Detecting high rates of ultracold neutrons and thermal neutron production

by

Lori Ann Rebenitsch

Thesis submitted to the Faculty of Graduate Studies of
the University of Manitoba
in partial fulfilment of the requirements of the degree of

Doctorate of Philosophy

Department of Physics and Astronomy
University of Manitoba
Winnipeg

Abstract

The first phase of the TRIUMF ultracold advanced neutron source (TUCAN) is operational at TRIUMF in Vancouver, Canada, with the second phase scheduled to be completed in 2020. The first proposed experiment with the source is a neutron electric dipole moment (nEDM) measurement. Preparing the experiment requires building the nEDM experimental cell, containing high voltage, magnetic fields, B_0 and B_1 coils, magnetic shielding to run the Ramsey cycle; a prototype detection system; and commissioning the TUCAN source. This thesis focuses on measurements that characterize the prototype UCN counter, as well as the thermal neutron flux measurement around TUCAN, as part of the source commissioning.

The UCN counter is a ^{6}Li-doped glass detector, designed for high rates of UCN. The detector efficiency is comparable to the GEM-based Cascade-U detector at the UCN source at the Paul Scherrer Institute. Comparing the ^{6}Li detector to simulation gave a neutron efficiency of 99.5 ± 0.5 % with a background contamination of 0.3 ± 0.1 %. The total efficiency of this detector was measured to be $89.7^{+1.3}_{-1.9}$ %.

The thermal neutron measurement used Au and Cd-covered Au foils to measure the thermal and colder neutron flux around TUCAN at different temperatures. This measurement was conducted at TRIUMF during the initial commissioning of neutron production. There were some large discrepancies between the measured data and simulation and also between measurements with the same settings. A number of discrepancies were found to be due to differences between the experimental set up and the model. Modeling graphite, in particular, is limited due to the wide variability of the structure of graphite and is known to vary up to 40% from the measurement depending on struc-

tural factors. The largest discrepancy was due to difficulties in steering the proton beam onto the tungsten target. However, none of the simulated effects were large enough to cover the measured results, suggesting there was a systematic effect that was not well-understood. While thermal and colder neutron flux was measured, the amount varied too much from irradiation run to irradiation run to determine the flux with consistency.

Contents

List of Tables

List of Figures

Part I

Introduction and motivations

Chapter 1

Theoretical introduction

1.1 Matter-antimatter asymmetry

One of the fundamental questions in cosmology is, “Why is there a matter-antimatter asymmetry of the universe?” The baryon asymmetry is useful in illustrating the matter-antimatter asymmetry because most matter is made out of baryons. At the Big Bang, the total number of baryons and antibaryons were assumed to be equal. These baryons and antibaryons annihilated to produce photons. As the universe expanded and cooled the matter-antimatter density became low enough to stop the annihilation process. Assume the number of baryons is n_b, the number of antibaryons is $n_{\bar{b}}$, and the number of photons is n_γ. Then, the dimensionless baryon-antibaryon asymmetry fraction, η, is

$$\eta = \frac{n_b - n_{\bar{b}}}{n_\gamma}. \tag{1.1}$$

At the beginning of the Big Bang, $\eta = 0$ by symmetry arguments, and adding in known Standard Model (SM) Charge-Parity (CP) violation, the asymmetry fraction becomes $\eta \approx 10^{-18}$ [1, 2]. This asymmetry is measured to be $\eta = 6.1^{+0.3}_{-0.2} \times 10^{-10}$ from the cosmic microwave background, which is eight orders of magnitude higher than standard model predictions [3]. While proposing an initial asymmetry would resolve the question of the existing matter-antimatter asymmetry, this does not agree well with other symmetries already present in nature.

In grand unified theories (GUTs), there are three proposed conditions for baryogenesis known as the Sakharov conditions [4]:

- Baryon number violation,
- C and CP-violation, and
- Interactions out of thermal equilibrium.

While the SM has sources of C and CP-violation, the amount is far short of what would be required for the observed baryon/anti-baryon asymmetry. New sources can be probed by finding nonzero electric dipole moments (EDM) of atoms, fundamental particles, and possibly in neutrino mixing. Here we focus on the neutron electric dipole moment (nEDM).

1.1.1 Evidence for baryon asymmetry

In this section, the evidence for baryon asymmetry is explored in more detail. In astronomical measurements, most of the observable mass is comprised of protons, neutrons, and electrons, where protons and neutrons (both being baryons) provide the most mass. In addition, antibaryons, predominately antineutrons and antiprotons also exist, and annihilate with the baryons to produce photons. The number of baryons to photons was found by fitting models to the measured cosmic microwave background (CMBR) about 4.4 %. In the same fit to the CMBR, the baryon/antibaryon asymmetry is computed to be $\eta = 6.1^{+0.3}_{-0.2} \times 10^{-10}$.

While it is tempting to propose pockets of antimatter or other sources of antimatter to explain the discrepancy, such pockets have not been observed [3]. This led to theories postulating previously unobserved interactions as extensions to the SM.

1.1.2 The Sakharov conditions

A. Sakharov determined three conditions for the development of the baryon/anti-baryon asymmetry. Each of the three conditions is briefly described below [3]:

Baryon number violation Baryon number violating interactions have to have occurred sometime after the Big Bang.

C and CP-violation A condition of these interactions is that the interactions are not fully reversed. Not every interaction occurs at the same rate, resulting in a higher rate of particles over antiparticles.

Interactions out of thermal equilibrium Most of the history of the universe occurs in thermal equilibrium, particularly 2-3 minutes after the big bang. This means that, at that time, there were equal masses of particles and antiparticles. Even if asymmetrical interactions occurred, the conditions of thermal equilibrium require that these masses remain equal. A net asymmetry of matter, then, can only occur if the interactions occur out of thermal equilibrium.

1.2 The neutron electric dipole moment in the Standard Model and beyond

An electric dipole moment is defined as a moment where two opposite point charges $\pm q$ are separated by a distance $\vec{r}$, or $\vec{d} = q\vec{r}$, where $\vec{d}$ is the electric dipole moment, usually set in units of e.cm. The neutron electric dipole moment (nEDM) is calculated in the SM at the level of $|d_n| \approx 10^{-32}$ e.cm in the electroweak sector [5], and measurements place a limit on the moment of $|d_n| < 3.0 \times 10^{-26}$ e.cm [6].

1.2.1 Symmetries

EDMs demonstrate parity (P) and time (T) violation and as a consequence, charge-parity (CP) violation, as illustrated in Figure 1.1. In order to explain how EDMs demonstrate this, we first review the CPT-symmetries.

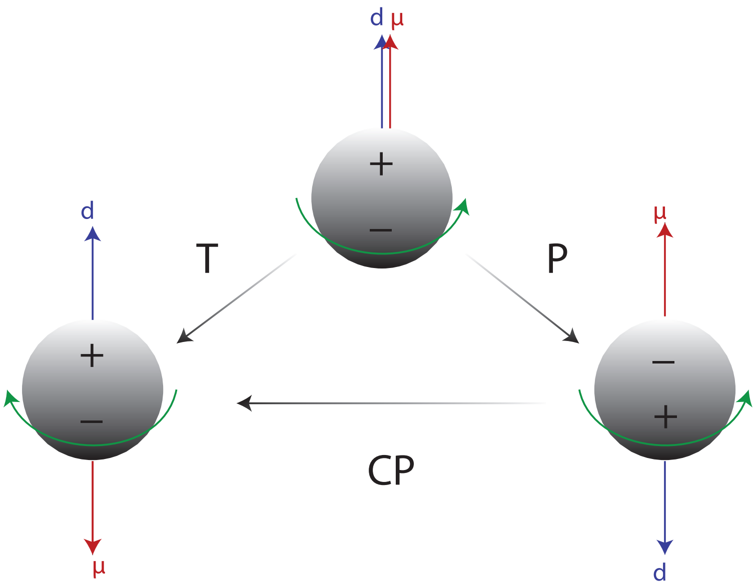

Figure 1.1: Drawing of the neutron magnetic dipole moment and electric dipole moment under T-reversal, P-reversal, and CP-reversal.

Charge (C) symmetry refers to the charge conjugation of a particle. This refers to the symmetry of flipping the charge, from, for example, positive to negative, and also the color charge, lepton/baryon number and so on into the corresponding anti-particle.

Parity (P) symmetry refers to the spatial symmetry of particles, or the inversion of all space coordinates in the Cartesian coordinate system. This can be compared to finding the mirror image of a particle.

Time (T) symmetry refers to processes that are reversible. The common example used to demonstrate time reversal symmetry is the ability to play a movie of moving balls on a table forward or backward and both are physically possible.

Taken all together, the three symmetries make up the universal CPT-symmetry which is assumed to be conserved. Violation of one symmetry results in violation of the other two symmetries to maintain the total symmetry. For example, a particle which has CP-violation also must have T-violation. Figure 1.1 shows the relationship between CP-violation and T-violation.

1.2.2 CP violation and EDM

CP-violation can occur in either the strong or the electroweak sector. In the strong sector, CP-violation occurs in the gluon interaction with the quantum vacuum as discussed in the next section [5]. In the electroweak sector, neutron electric dipole moments (nEDM) could occur with a two quark model with a spectator quark, which would give a nEDM of $|d_n| \approx 10^{-32}$ e.cm [7]. Many extensions to the SM require a higher amount of CP-violation in the electroweak sector.

While C and P are maximally violated in the electroweak sector, the combined CP-symmetry has so far been observed to be conserved. To see how CP-violation works with an EDM, consider a classical dipole. Under parity inversion ($P(\vec{r}) = -\vec{r}$), an EDM is odd:

$$P(\vec{d}) = -\vec{d}. \tag{1.2}$$

However, a neutron can be defined in quantum mechanics as a vectoral observable. Assuming a neutron with spin 1/2 and a permanent EDM reduces the EDM to be aligned with the spin, $\vec{S}$, as the spin is the only intrinsic vectoral quantity, according to the Wigner-Eckart theorem. So, for a neutron,

$$\vec{d_n} = |d_n|\vec{S}/S. \tag{1.3}$$

Since spin for a neutron is even under parity inversion, then $\vec{d_n}$ is even. In order for both conditions to be true, either $|d_n| = 0$ or parity is also violated making an overall CP-violation. For T-symmetry, or conversely, CP-symmetry, spin, $\vec{S}$ for a fermion is odd under transformation and position, $\vec{r}$, is even under transformation. Again, in order for both conditions to be true, either $d_n = 0$ or CP-symmetry is violated.

1.3 Standard Model predictions

Two sources of CP-violation exist in the SM: one in the weak interaction of mixing the weak mass eigenstates and of the flavor eigenstates of neutrinos [8] and another in the CP-odd vacuum polarization term in the QCD Lagrangian [9].

1.3.1 Cabibbo-Kobayashi-Maskawa matrix

The interaction of quark masses and mixing are related in the SM by the Yukawa interactions with Higgs condensate:

$$\mathcal{L} = -Y^d_{ij}\bar{Q^I_{Li}}\phi d^I_{Rj} - Y^u_{ij}\bar{Q^I_{Li}}\epsilon\phi^* u^I_{Rj} + h.c. \tag{1.4}$$

The $Y^{u,d}$ are 3×3 complex matrices representing the interactions between the quarks and the Higgs boson, ϕ is the Higgs field, i and j are indices, ϵ is the 2×2 antisymmetric tensor, Q^I_L are left-handed quark doublets, and d^I_R and u^I_R are right-handed up/down quarks singlets in the weak-eigenstate basis [10]. Mass terms for the quarks arise from the Higgs field when $\langle\phi\rangle = (0, v/\sqrt{2})$, where v is the vacuum expectation value. Physical states are derived by diagonalizing $Y^{u,d}$ by four unitary matrices, $V^{u,d}_{L,R}$ via

$$M^f_{diag} = V^f_L Y^f V^{f\dagger}_R (v/\sqrt{2}), f = u, d. \tag{1.5}$$

The charged-current $W^{\pm}$ interactions couple to the u_{Li} and d_{Lk} quarks in the weak interaction,

$$V_L = \frac{-g}{\sqrt{2}}(\bar{u_L}, \bar{c_L}, \bar{t_L})\gamma^\mu W^+_\mu V_{CKM} \begin{pmatrix} d_L \\ s_L \\ b_L \end{pmatrix} + h.c. \tag{1.6}$$

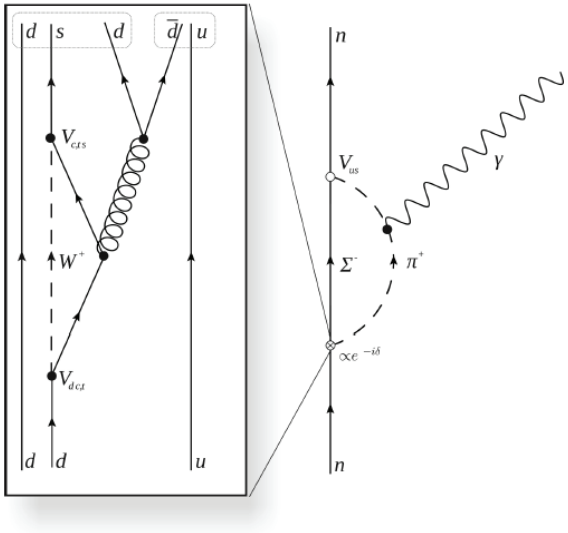

Figure 1.2: Diagram of a strong interaction with a four quark vertex. This is an example of a strong penguin interaction and is the largest source of CP violation in the SM. Figure from [9].

Solving for V_{CKM} gives the Cabibbo-Kobayashi-Maskawa (CKM) matrix:

$$V_{CKM} = \begin{pmatrix} c_{12}c_{13} & s_{12}c_{13} & s_{12}e^{-i\delta} \\ -s_{12}c_{23} - c_{12}s_{23}s_{13}e^{-i\delta} & c_{12}c_{23} - s_{12}s_{23}s_{13}e^{-i\delta} & s_{23} \\ s_{12}s_{23} - c_{13}c_{23}c_{13}e^{-i\delta} & -c_{12}s_{23}s_{13}e^{-i\delta} & c_{23}c_{13} \end{pmatrix}, \tag{1.7}$$

where $c_{ij} = \cos\theta_{ij}$, $s_{ij} = \sin\theta_{ij}$, and $\delta \approx 1.20$ rad is the CP-violating phase, called the Kobayashi-Maskawa phase, which is responsible for the observed CP-violation in the K and B meson decays. The largest contribution to CP-violation in the SM is from the strong penguin diagram (at the three-loop level), as shown in Figure 1.2 [11]. This gives a contribution to the neutron EDM of $d_n^{CKM} \approx 10^{-32}$ e.cm [5]. The CKM phase is the only known source of CP-violation in the SM, which means that the SM has strong predictions for CP asymmetries, whether the asymmetries vanish, or are not correlated [8]. CP violation by the strong interaction is covered in the next section.

To test the unitarity of the CKM matrix, the six V_{ij} components can be combined to represent triangles in the complex plane. For example,

$$V_{ud}V_{ub}^{*} + V_{cd}V_{cb}^{*} + V_{td}V_{tb}^{*} = 0 \tag{1.8}$$

represents one such triangle. The most recent fit for the CKM matrix from the Particle Data Group (2017 update) is

$$V_{CKM} = \begin{pmatrix} 0.97434^{+0.00011}_{-0.00012} & 0.22506 \pm 0.00050 & 0.00357 \pm 0.00015 \\ 0.22492 \pm 0.00050 & 0.97351 \pm 0.00013 & 0.0411 \pm 0.0013 \\ 0.00875^{+0.00032}_{-0.00033} & 0.0403 \pm 0.0013 & 0.99915 \pm 0.00005 \end{pmatrix} [8]. \tag{1.9}$$

A review of the measurements used for this most recent fit is mentioned in [8].

1.3.2 QCD-Lagrangian

The vacuum polarization term in the QCD-Lagrangian, $\mathcal{L}_{QCD}^{CPV}$, is

$$\mathcal{L}_{QCD}^{CPV} = \frac{g_s^2}{32\pi^2}\bar{\theta}G_{\mu\nu}^{a}\tilde{G}^{\mu\nu,a}, \tag{1.10}$$

where g_s is the strong coupling constant, $\bar{\theta}$ is the phase, and $G_{\mu\nu}^{a}$ is the gluon field tensor. $G_{\mu\nu}^{a}\tilde{G}^{\mu\nu,a}$ corresponds to $\mathbf{E} \cdot \mathbf{B}$ which is both T and P odd under reversal. A dimensional analysis gives $|d_n^{QCD}| \approx \bar{\theta} \times 10^{-16}$ e.cm. However, the current nEDM measurement restrict $\bar{\theta} \leq 10^{-10}$ when theoretically $\bar{\theta}$ can be anywhere between 0 and 2π. This is known as the "strong CP problem" and a number of theories have been postulated to account for the small $\bar{\theta}$, such as axions [12, 13].

1.4 Extensions to the Standard Model

Since the SM in its current form does not explain all of the existing baryon asymmetry in the universe, a number of extensions to the SM model have been postulated, especially supersymmetry.

These extensions generally add new particles and additional CP-violation phases which would increase the one loop contribution to the nEDM, generating a larger nEDM than $d_n > 10^{-30}$ e.cm. These extensions and how EDMs constrain these theories are briefly described below.

Left-right symmetric models add additional right-handed W and Z bosons to the SM. In the SM, weak interactions contributing to the EDM cancel to first order, which leaves the second order contributions, where the weak force acts twice, to contribute as the square of the weak force in the EDM. Left-right models do not have the first order weak interactions cancel, which give a higher EDM due to the weak interaction.

Supersymmetry, or SUSY, adds additional symmetries between boson and fermions. A generic SUSY model gives a neutron EDM with an order of

$$d_n \sim \left(\frac{300\text{ GeV}}{\Lambda_{SUSY}}\right)^2 \sin\phi_{CP} \times 10^{-24}\text{ e.cm}, \tag{1.11}$$

where ϕ_{CP} is a new CP-violating phase, and Λ_{SUSY} is the SUSY mass scale. The current experimental limits require either that the ϕ_{CP} is small and fine-tuned, 1-loop contributions are suppressed, or the SUSY scale is well above the weak scale [9, 3, 14]. Since EDMs have been measured to higher and higher precision, this restricts the energy range of where the SUSY mass scale may occur to higher energies. Figure 1.3 shows the required constraints of SUSY models well above the weak scale, where d_n is less constrained.

1.5 Sensitivity of nEDM to physics beyond the SM and Motivation of Work

Combining the CP-violation contributions in the SM together gives a nEDM limit of $|d_n| < 10^{-30}$ e.cm [9]. An nEDM larger than this would imply new physics. Theories that extend the SM require increased amounts of CP-violation, leading to an nEDM between 10^{-28} and 10^{-26} e.cm [14]. The SM expectation of the nEDM and a selection of extensions to the SM are compared to

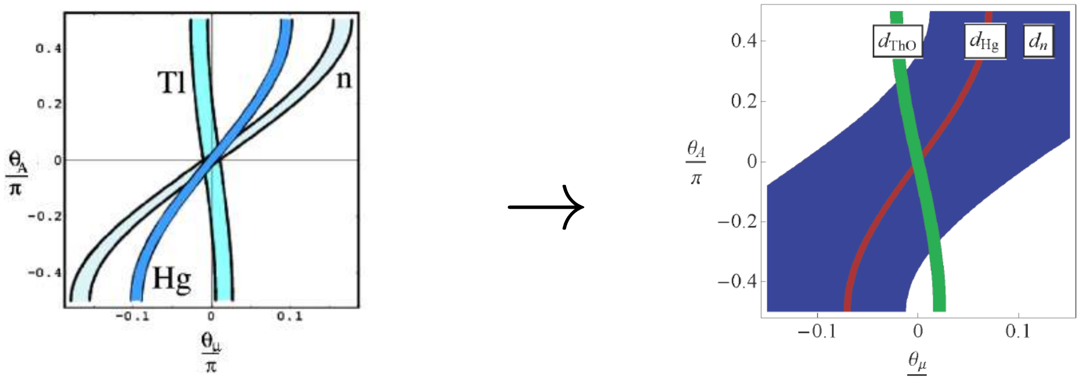

(a) $M_{SUSY} = 500\text{GeV}$

(b) $M_{SUSY} = 2\text{TeV}$

Figure 1.3: Drawing of a generic SUSY-model with neutron, Hg, and ThO constraints. Since the EDM of the electron and Hg have excluded SUSY models at lower energies, SUSY models with higher and more relaxed EDM requirements remain. Original figure on the left from [5] and updated figure on the right from [9].

the experimental limits of several experiments in Figure 1.4.

Measuring the nEDM to higher precision is an effective method to constrain the different extensions to the SM. Determining the nEDM to such high precision, however, requires high statistics. Ultracold neutrons (UCN) provide a means to reach this level of statistical sensitivity due to existing and developing technologies that allow the measurement of the spin state of high densities of UCN using Ramsey's technique. The method of using UCN to measure nEDM to high precision, using the Ramsey technique, is described in detail in Chapter 2. A survey of recent and developing experiments using UCN to measure nEDM to high precision is outlined in Chapter 3. The work in this thesis was done in collaboration with the nEDM experiment at TRIUMF, in Vancouver, BC. An outline of the nEDM experiment is shown in Chapter 4. This thesis describes two measurements in preparation for an nEDM experiment at TRIUMF. The first measurement is a characterization of the UCN detector that is used to count the neutrons after going through a Ramsey cycle and is described in Part II. The second measurement is of the density of the thermal and colder neutron flux that occurs at the neutron production stage and is described in Part III. These measurements are important in order for the nEDM experiment at TRIUMF to reach an even higher d_n precision.

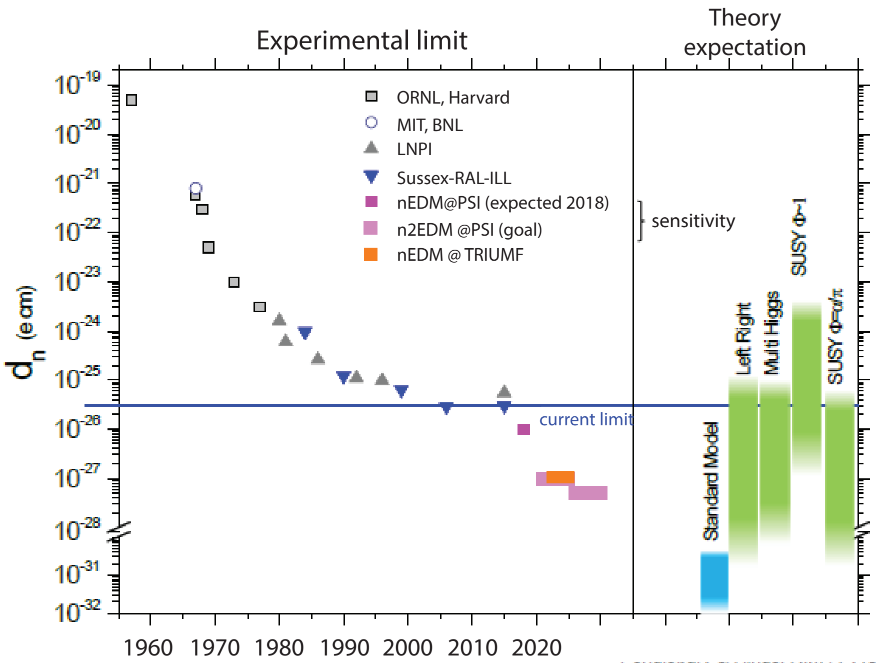

Figure 1.4: Graph depicting the nEDM measurements from the 1950s to predicted sensitivities to the left and the range of theoretical nEDM estimates to the right. Figure adapted from [15].

Chapter 2

Experimenting with ultracold neutrons

This chapter describes the nEDM measurement techniques. Here the focus is on the use of ultracold neutrons (UCN), where the nEDM has been measured to the 3×10^{-26} e.cm level. First, we review properties of UCN that make them useful for measurements of their fundamental properties, then, the Ramsey method which is used reach the desired level of precision, is presented.

2.1 Properties of ultracold neutrons

Neutrons consist of one up quark and two down quarks and have a known magnetic moment, $\vec{\mu}_n$. At energies below 300 neV, or less than 3 mK, neutrons display unique properties, such as being strongly subject to gravity rather than slightly, or $mgh \approx h \cdot 1.025$ neV/cm, and reflecting off materials with a high Fermi potential:

$$V_F = \frac{2\pi\hbar^2}{m_n}\mathcal{N}b, \tag{2.1}$$

where m_n is the neutron mass, $\mathcal{N}$ is the nucleon density, and b is the neutron scattering length. Examples of materials with a Fermi potential high enough to contain UCN, $V_F \in (200, 350)$ neV, include ^{58}Ni (335 neV), NiMo (85 to 15 percent ratio, 220 neV) [16] and BeO/Be (261/252 neV) [17]. UCN can also be polarized, and have energy $\vec{\mu_n} \cdot \mathbf{B}$ of 60 neV/T. In a magnetic field of 5 T, all

UCN with spin up encounter a 300 neV barrier while UCN with spin down pass through the field.

In order to measure the nEDM with UCN, the UCN need to be polarized and contained as long as possible. The storage time for UCN is affected by various losses [9]:

$$\frac{1}{\tau_s(E)} = \frac{1}{\tau_\beta} + \frac{1}{\tau_\eta(E)} + \frac{1}{\tau_{gap}(E)} + \frac{1}{\tau_{gas}(E)}, \tag{2.2}$$

where τ_β is the loss due to neutron β decay, $\tau_\eta(E)$ is the loss due to absorption on the walls, τ_{gap} is the loss due to gap in the containing surface, and τ_{gas} is the loss due to upscattering neutrons with gas molecules. Since nEDM measurements have UCN stored in vacuum conditions, this last loss is typically negligible. Self-interactions are also ignored since the densities of UCN are typically low.

Accounting for these losses, the number of UCN, $N(t)$, remaining after a storage time t is

$$N(t) = \frac{\int \mathrm{d}E N_0(E)\mathrm{exp}(-t/\tau_s(E))}{\int \mathrm{d}E N_0(E)}, \tag{2.3}$$

where $N_0(E)$ is the initial UCN spectrum. This can be further approximated into fast and slow moving components of the spectrum, which suffices for many measurement purposes, as

$$N(t) = N_f \mathrm{exp}(-t/\tau_f) + N_s \mathrm{exp}(-t/\tau_s), \tag{2.4}$$

where N_f and τ_f are the initial number of UCN and loss time-constant of the UCN with high energies compared to the wall and N_s and τ_s are the initial number of UCN and loss time constant of the UCN with low energies compared to the wall. More information regarding UCN optics can be found in [17, 18].

2.2 Measuring nEDM using UCN

In order to measure the nEDM at high precision, both **E** and **B** fields are used to separate the nEDM from the magnetic moment. This section describes the Ramsey method of measuring the nEDM [9, 19].

2.2.1 Theoretical method of measuring nEDM at high precision

In the nonrelativistic limit, the Hamiltonian for a UCN is

$$H = -\vec{d_n} \cdot \mathbf{E} - \vec{\mu_n} \cdot \mathbf{B}, \tag{2.5}$$

where **E** is the electric field and **B** is the magnetic field. Looking at this alone, it appears possible to find an upper bound for the nEDM by minimizing the magnetic field and strengthening the electric field and measuring the precession frequency of the neutron's spin in that field. However, in order to reach to the desired precision, such a configuration would require a magnetic field of less than 0.83 fT. For reference, Earth's field is at least 25 μT, and the best magnetically shielded rooms, such as those at the Technical University of Munich, Germany, [20] and the Physikalisch-Technische Bundesanstalt in Berlin, Germany, [21] which have an approximate shielding factor of more than 10^6, cannot reduce the magnetic field to less than 1 fT.

Another way of measuring the nEDM is by finding the Larmor precession frequency for parallel and antiparallel **E** and **B** fields:

$$\hbar\omega_{\uparrow\uparrow} = 2\left|\vec{\mu_n} \cdot \mathbf{B}^{\uparrow\uparrow} + \vec{d_n} \cdot \mathbf{E}^{\uparrow\uparrow}\right|, \tag{2.6}$$

and

$$\hbar\omega_{\uparrow\downarrow} = 2\left|\vec{\mu_n} \cdot \mathbf{B}^{\uparrow\downarrow} - \vec{d_n} \cdot \mathbf{E}^{\uparrow\downarrow}\right|, \tag{2.7}$$

where $\uparrow\uparrow$ refers to parallel and $\uparrow\downarrow$ refers to antiparallel fields, ω_{ij} is the precession frequency of the neutron in a particular field configuration, and $\hbar$ is the reduced Planck constant. Combining the

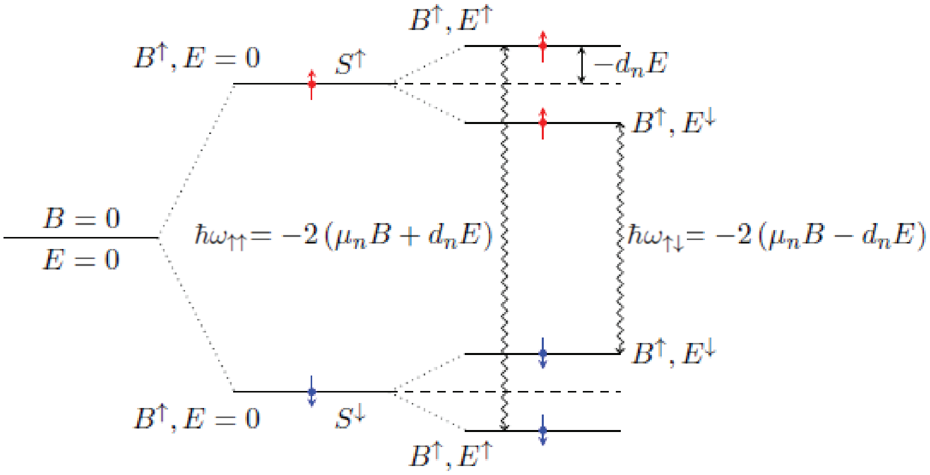

Figure 2.1: Neutron energy level diagram for different **E** and **B** fields used to measure the $|d_n|$. ↑ and ↓ refer to the direction of the field. Originally derived from [19]. Used with permission.

above two equations gives a neutron EDM of

$$|d_n| = \frac{\hbar(\omega^{\uparrow\uparrow} - \omega^{\uparrow\downarrow}) - 2|\mu_n|(B^{\uparrow\uparrow} - B^{\uparrow\downarrow})}{2(E^{\uparrow\uparrow} - E^{\uparrow\downarrow})}. \tag{2.8}$$

In the case where the **B** field is unchanged in the parallel and antiparallel configuration, the formula reduces to

$$|d_n| = \frac{\hbar(\omega^{\uparrow\uparrow} - \omega^{\uparrow\downarrow})}{4E}. \tag{2.9}$$

Figure 2.1 gives a graphic depiction of how the $|d_n|$ is derived from the parallel and antiparallel fields.

This method requires finding the precession frequency in two different **E** and **B** field configurations. There are two ways of doing this. One way is by using two adjacent volumes with opposite electric fields. This requires the same magnetic field through both volumes. The other way is by measuring with one configuration and then switching the polarity of the electric field and measuring again. This requires keeping the magnetic field stable throughout the measurements.

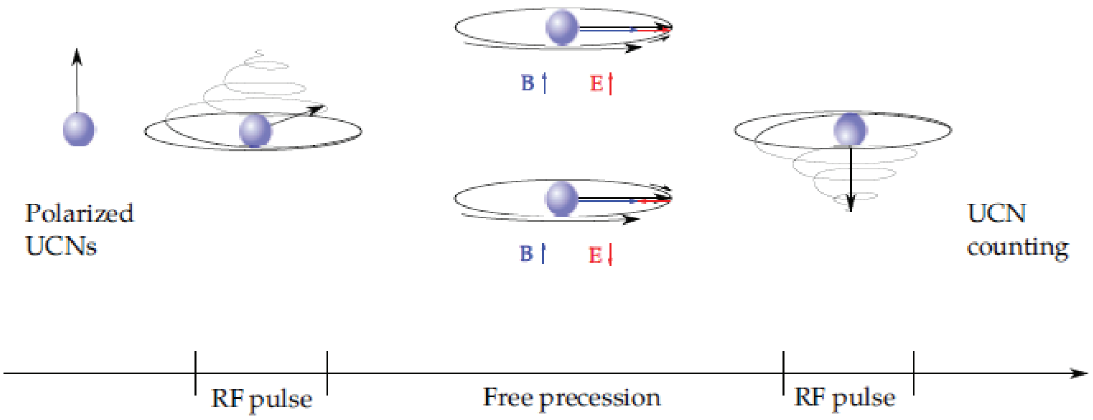

Figure 2.2: Ramsey's technique of separate oscillating fields. Polarized neutrons are exposed to an RF pulse, allowed to precess, and then exposed to another RF pulse before being counted. As the gyromagnetic ratio is negative, neutrons with spin down are high-field seeking, which gives the "spin-down" neutron with an upward arrow for high-field seeking. Figure from [19]. Used with permission.

2.2.2 Ramsey's technique

In order to experimentally measure the Larmor precession frequency, the method developed by Ramsey is described below [22]. A graphic depicting the technique is shown in Figure 2.2.

First, polarized UCN are collected in a precession chamber with parallel or antiparallel **E** and **B** fields. The UCN are polarized along the initial $\mathbf{B}_0$. Then an oscillating (RF) magnetic field pulse, $B_{rf} = B_1 \cos(\omega_{rf}\tau)$, perpendicular to $\mathbf{B}_0$, is applied for a time, τ. This RF pulse is at the new Ramsey frequency, $\omega_{rf} = \gamma_n \mathbf{B}_0$, and is chosen to be the length of the pulse so that the spins rotate into a plane parallel to B_{rf}. This causes the neutron spin to flip to the plane orthogonal to $\mathbf{B}_0$. The neutrons are then given a time, T, to freely precess. This results in the neutron spin accumulating an additional phase, $\phi = \gamma_n BT$. Then, the RF pulse is applied for another τ. After this, the neutrons of each spin state are counted using a detector.

The goal of this technique is to find if $\phi = \omega_{rf}T$. If this is so, then $B = \omega_{rf}/\gamma_n$. When optimized, the RF pulse is applied with enough power and for the right length of time, τ, to flip the spin by $\pi/2$. The probability of a neutron with initial spin $|\downarrow\rangle$ to have the same final spin state

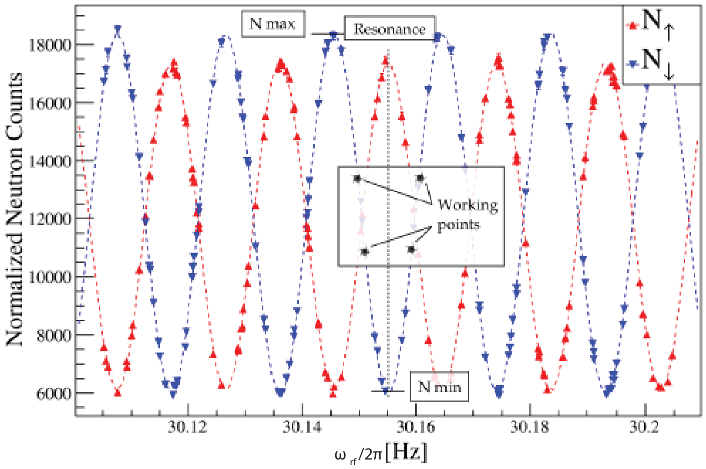

Figure 2.3: Sample Ramsey pattern obtained from PSI [19]. Used with permission. The central fringe points are specified in the graph as the working points.

$\langle\downarrow|$ after the time-evolution operator, $U(T, \omega_{rf})$, acting on the spin is [23]

$$P(T,\omega_{rf}) = |\langle\downarrow|U(T,\omega_{rf})|\downarrow\rangle|^2 \tag{2.10}$$

$$= 1 - \frac{4\omega_1^2}{\Omega^2}\sin^2\left(\frac{\Omega t_{\pi/2}}{2}\right)\left[\frac{\Delta}{\Omega}\sin\left(\frac{\Omega t_{\pi/2}}{2}\right)\sin\left(\frac{T\Delta}{2}\right) - \cos\left(\frac{\Omega t_{\pi/2}}{2}\right)\cos\left(\frac{T\Delta}{2}\right)\right]^2, \tag{2.11}$$

where $\omega_1 = -\gamma_n B_1$, $\Delta = \omega_{rf} - \omega_0$, and $\Omega = \sqrt{\Delta^2 + \omega_1^2}$. When $\gamma_n B t_{\pi/2} = \pi/2$, the central fringe range where $\Delta \ll \omega_1$ can be simplified to

$$P(T,\omega_{rf}) = 1 - 4\left(\sin^4\frac{\pi}{4}\right)\left[\frac{\Delta}{\Omega}\sin\frac{T\Delta}{2} - \cos\frac{T\Delta}{2}\right]^2 \tag{2.12}$$

$$P(T,\omega_{rf}) \approx 1 - \cos^2\frac{T\Delta}{2} \tag{2.13}$$

$$P(T,\omega_{rf}) \approx \frac{1}{2}(1 - \cos(T\Delta)). \tag{2.14}$$

The Ramsey interference pattern is recorded by scanning ω_{rf} while keeping all other conditions constant as shown in Figure 2.3. Counting the number of neutrons with spin up or down in this central fringe ($\omega_{rf} = \gamma_n B$), particularly where the slope is steepest, is used for finding the Larmor frequency. In counting the neutrons, this becomes

$$N^{\uparrow/\downarrow} = \frac{N}{2}\left\{1 \mp \alpha^{\uparrow/\downarrow}(T)\cos\left[(\omega_{rf} - \gamma B_0)\cdot(T + \frac{4t_{\pi/2}}{\pi})\right]\right\}, \tag{2.15}$$

where $N^{\uparrow/\downarrow}$ are the number of counted neutrons with spin up or down, $\alpha(T)$ is the fringe visibility and the $\frac{4t_{\pi/2}}{\pi}$ term accounts for the B_1 and B_0 inhomogeneities. This is fitted to the data. The visibility fringe is defined in terms of $N^{\uparrow/\downarrow}$ as

$$\alpha^{\uparrow/\downarrow}(T) = \frac{N^{\uparrow/\downarrow}_{max} - N^{\uparrow/\downarrow}_{min}}{N^{\uparrow/\downarrow}_{max} + N^{\uparrow/\downarrow}_{min}}. \tag{2.16}$$

From this fit, the Larmor precession frequency can be found for both configurations of **E** and **B** fields. Typically, the four measurement points around the Larmor frequency are used as a sequence of measurements with the spins ↑↑, ↓↑ of the of the **E** and **B** fields. Every so often, the **B** might be flipped, in order to perform a check.

2.2.3 Statistical sensitivity

The statistical sensitivity can be computed by first deriving ω_0 from Equation 2.15, and finding the uncertainty of the Lamour frequency [19, 9]:

$$\sigma(\omega_0) \approx \frac{1}{\alpha T\sqrt{N_{tot}}}, \tag{2.17}$$

where N_{tot} is the total number of neutrons detected integrated over all measurement cycles.

Equation 2.17 can then be used with Equation 2.9 to find the statistical sensitivity of two nEDM measurements:

$$\sigma(d_n) \approx \sqrt{2}\frac{\hbar}{4E}\frac{1}{\alpha T\sqrt{N_{tot}/2}} = \frac{\hbar}{2\alpha TE\sqrt{N_{tot}}} \tag{2.18}$$

where the $1/\sqrt{2}$ factor is to account for the required two measurements, in order to take the difference between the flipped E measurements. This gives a statistical sensitivity which depends on maximizing N_{tot}, and the storage time T. Adding in the UCN storage losses (approximating N_{tot} to $N_{tot}(\omega) = N_0\text{exp}(-T/\bar{\tau})$ and the transverse spin coherence time T^* of the precessing spins gives

$$\sigma(d_n) = \frac{\hbar}{2\alpha_0 \text{exp}\left(-T/T^*\right) TE\sqrt{N_{tot}(\omega)}}. \tag{2.19}$$

The minimum is at

$$T = \frac{2T^*\bar{\tau}}{T^* + 2\bar{\tau}}, \tag{2.20}$$

which gives a minimum sensitivity of

$$\sigma_{min}(d_n) = \frac{\hbar}{4\alpha_0 T^* E\sqrt{N_0}} \frac{\text{exp}\left(\frac{2\bar{\tau}}{T^*+2\bar{\tau}}\right)}{\sqrt{\text{exp}\left(-\frac{2T^*}{T^*+2\bar{\tau}}\right)}} \frac{T^* + 2\bar{\tau}}{T^*\bar{\tau}}. \tag{2.21}$$

From this equation we see several factors that can be maximized in order to find the nEDM at high precision, such as the E-field, higher numbers of UCN, and the precession time. However, these factors can influence each other and can influence the systematic uncertainty. For example, increasing precession time increases UCN losses.

2.3 Detection of UCN

There are a number of challenges in the detection of UCN. First, neutrons are of neutral charge, so UCN require special detection methods. Second, there are often thermal and high energy neutrons produced along with the UCN, and so detection techniques and neutron shielding are required to count only the UCN. Third, nEDM experiments require measuring UCN according to spin and counting each spin in order to fit Equation 2.15.

To address the first challenge, counting neutrons cannot be done using typical ionization processes. Instead, detection methods rely on capturing neutrons on nuclei, which depends on the neutron capture cross-section. The capture process then produces charged particles from the breakup of the nucleus. These charged particles are then detected by typical ionization processes.

In the second challenge, only UCN are to be detected. While high energy neutrons produce recoil interactions with proton-rich materials [9], this is not the case with UCN. UCN can be reflected with materials of high Fermi potential and can be blocked from entering the detector if the incident UCN do not have enough energy to penetrate the detector barrier. Experiments also produce background signals from thermal neutrons, gamma rays and βs that can be picked up by the UCN detectors. Most detection techniques use detectors with low or separable background and use shielding to stop thermal neutrons and gammas from entering or leaving the UCN guide. More information about UCN detectors can be found in Chapter 5.

In the third challenge, UCN are to be counted according to spin. This is done by placing a highly magnetized iron layer on an aluminum foil in the pipe leading to the counter. The magnetic field in the highly magnetized iron is close to 2 T, so that high field seeking (spin down) neutrons encounter a potential of 90 neV and pass through, while low field seeking (spin up) neutrons encounter a potential of 330 neV and reflect ($V_F = V_{Fe} \pm 2$ T $\cdot 60$ neV/T, where $V_{Fe} = 210$ neV). The addition of an adiabatic spin flipper [24, 25] offers the ability to detect both spins. Without the spin flipper, only neutrons with one spin are counted. When the spin flipper is on, the neutron spin is flipped before encountering the foil, so neutrons with the opposite spin are counted and the other neutrons are reflected. Counting both spins can be done sequentially or simultaneously. Sequential counting uses one detector with the spin flipper being turned on and off for different periods of time, to sequentially count neutrons of different spins. Simultaneous counting uses two detectors and UCN guides. A spin flipper is placed in one guide so that neutrons of one spin are counted in the detector at the end of that guide and the neutrons of the other spin are counted in the second detector at the end of the other guide. More information regarding neutron counting according to spin can be found in [19].

Chapter 3

Survey of nEDM experiments

The main statistical limitation on nEDM experiments is the achievable UCN density within the nEDM apparatus. Previously, experiments extracted low energy neutrons from reactors. These low-energy neutrons were then sent to moderators cooled to liquid D_2 temperatures. The UCN flux could be further increased by either vertical extraction or mechanical deceleration [26].

Superthermal sources were next to be considered [27]. In these sources, the neutron flux is exposed to a material where the neutrons downscatter to the UCN level. The material used for downscatter is usually superfluid ^{4}He (He-II), due to its unique properties (phonons and rotons) off which cold neutrons downscatter and are not absorbed [28, 29]. Superthermal sources have been demonstrated to be successful [30, 31]. Solid D_2 can also downscatter cold neutrons to the UCN level and is being used at the PSI and TRIGA Mainz UCN sources. While previously, the production and storage of UCN occurred in the same vessel, separate vessels for UCN production and storage were also developed [32]. Different types of superthermal sources are in use or are being developed, such as pulse sources, using reactors or spallation techniques [33, 34, 35, 30].

There are a number of nEDM experiments that have been done or are being done across the world, which have been completed, are running, or are planning their measurements. This chapter focuses on three recent experiments, two at ILL in Sections 3.1 and 3.2 and one at PSI in Section 3.3. Also, in this chapter, there is a brief overview of other experiments and sources to be

Table 3.1: Summary of nEDM experiments.

Experiment name	UCN Source	nEDM Apparatus	Magnetometry	Date completed/ to begin	nEDM precision measured/aim (e.cm)
ILL	He-II to vacuum	double chamber	199Hg, Cs-OPM	2015	3.0×10^{-26}
ILL-PNPI	He-II to vacuum	double chamber	Cs-OPM	2015	5.5×10^{-26}
PSI	SD$_2$	single chamber	199Hg, Cs-OPM	2017	Analysis in progress
SuperSUN	CN beam	double chamber	MSR	2019	4.2×10^{-28}
SNS	He-II in situ	double chamber	3He, SQUIDs	2023	3×10^{-28}
LANL	SD$_2$	single chamber prototype	-	-	$10^{-27} - 10^{-28}$
n2EDM at PSI	SD$_2$	double chamber	3He, 199Hg, Cs-OPM, MSR	2020	$10^{-27} - 10^{-28}$
PNPI-ILL-PTI	He-II to vacuum	double chamber	Cs-OPM	2020	3×10^{-28}
FRM-II	SD$_2$	double chamber	MSR	-	$\sim 10^{-28}$
TRIUMF	SD$_2$	double chamber	199Hg, 129Xe	2020	$10^{-27} - 10^{-28}$

constructed. A summary table of the experiments is shown in Table 3.1.

3.1 Institute Laue-Langevin

The measurement at the Institute Laue-Langevin (ILL), in Grenoble, France, has the current best nEDM limit [6, 36]. Neutrons with an average speed of 50 m/s were extracted from the liquid D_2O cold source in the high-flux reactor. The thermal neutrons were then guided upstream. The 'Steyerl' turbine mechanically Doppler-shifts the neutrons to UCN level [37]. The PF2 UCN source has 4 UCN beamlines, and 1 VCN beam [38]. A detailed description of the facility can be found in [39]. A drawing of the beamline is shown in Figure 3.1.

The UCN were then polarized, by only passing one spin state through a silicon foil with magnetized Fe to produce a field of approximately 0.1 T, prior to entering the spectrometer. The spectrometer consisted of a single precession chamber with Al electrodes, quartz cylinder, and a ^{199}Hg magnetometer. The smooth quartz cylinder was used for the first half of the data-taking period, and then replaced with a matte-finished quartz cylinder for the latter half. After the Ramsey sequence, the UCN were counted with a ^{3}He neutron detector [37]. Since both the neutron and Hg frequencies were measured, the frequencies are combined in the ratio [6]

$$R_a = \left| \frac{\nu_n \gamma_{Hg}}{\nu_{Hg} \gamma_n} \right|, \tag{3.1}$$

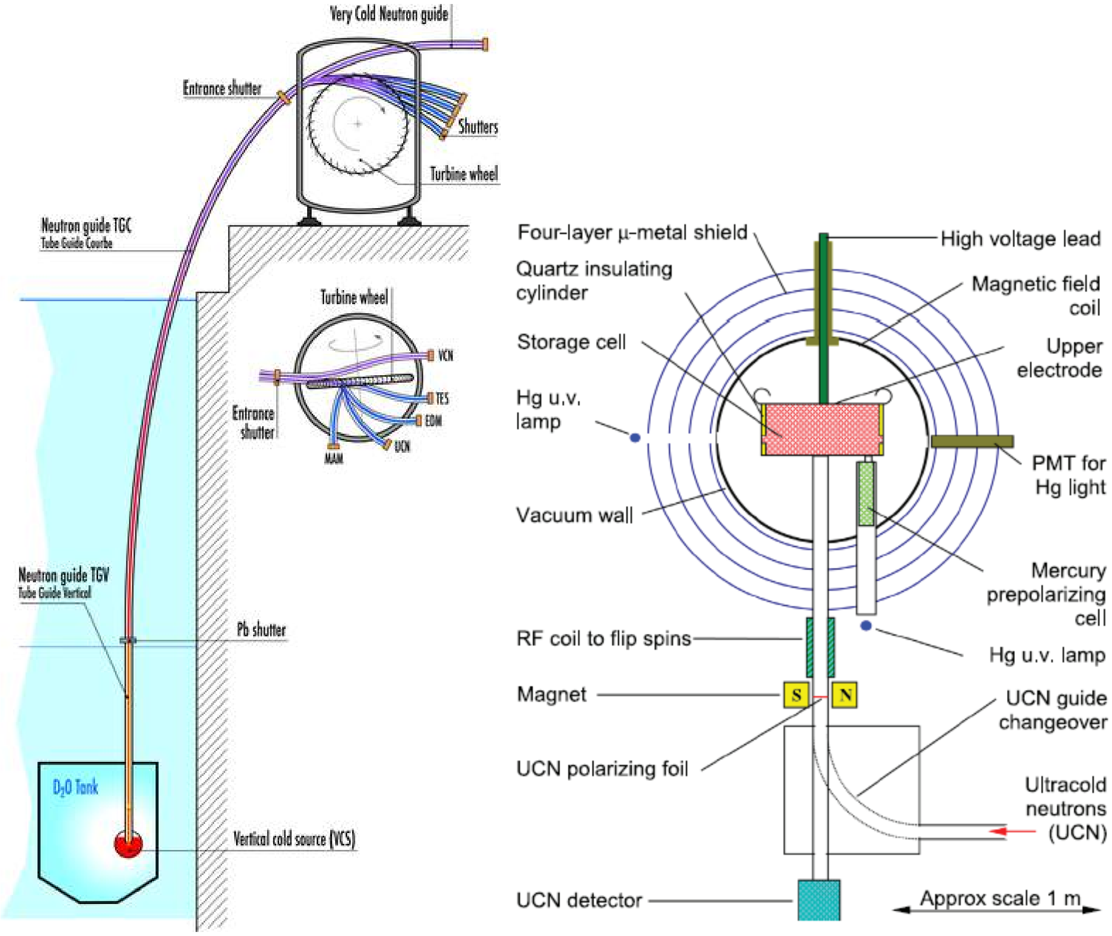

Figure 3.1: The PF2 and Steyerl neutron turbine at ILL is shown on the left, and the nEDM Spectrometer at ILL is shown on the right. Drawings from [38, 37].

where the ν's are the frequencies and the γ's are the gyromagnetic ratios of the neutron and the Hg nucleus.

A number of cuts were applied to the data. For example, an adjacent experiment was using a superconducting magnet. Turning the magnet on or off made a slight variation in R_a. A detailed analysis to identify false EDMs was conducted after the initial analysis. The Hg false EDM contribution to the measured d_n is

$$d_{n,Hg,f} = \pm\frac{\hbar}{8}|\gamma_n\gamma_{Hg}|\frac{r_B^2 B_{0_z}}{\Delta h c^2} \cdot R', \tag{3.2}$$

where r_B is the measurement cell radius, Δh is the height difference between the centers of mass of the different systems and

$$R' = R_a - 1 = \pm\Delta h\frac{\partial B_z/\partial z}{B_0}. \tag{3.3}$$

This gives a measured EDM of

$$d_{meas} = d' + d_{n,Hg,f}. \tag{3.4}$$

A false EDM caused a change in R_a or in $d_{n,Hg,f}$ without keeping the ratio between them constant and varies with the magnetic field.

Combining all the cuts, effects of false EDMs, the rotation of the Earth, potential leakage currents, sparks, and gravitational depolarization into a global fit gave $d_n < 3.0 \times 10^{-26}$ e.cm.

3.2 ILL-PNPI

Another nEDM measurement at ILL was in collaboration with the Petersburg Nuclear Physics Institute (PNPI) using the ILL reactor (PF2) with the installed PNPI spectrometer [40]. Analysis was finished in 2015. PF2 is explained in the previous section; this section focuses on the PNPI spectrometer.

The PNPI spectrometer has two UCN storage chambers with an integrated system of magnetic

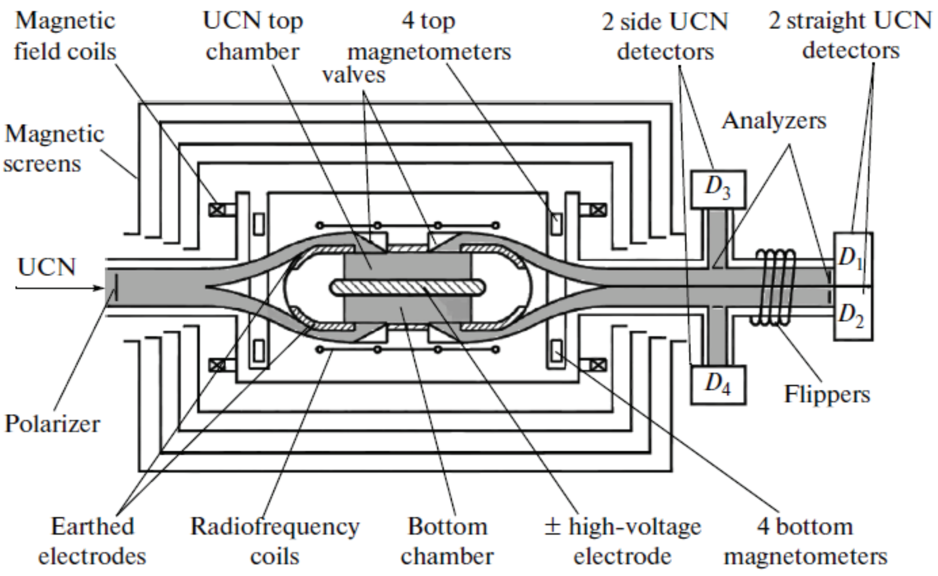

Figure 3.2: Drawing of the PNPI double chamber spectrometer. Figure from [40].

fields and each with electric fields of equal magnitude but opposite in direction. This dual chamber design serves to reduce false EDM. The spectrometer also has a dual polarization analysis system. Each chamber empties the resultant UCN into two detectors for a total of four detectors. In this way, each spin state of each chamber is measured and the nEDM is calculated as

$$d_n = \frac{1}{4}[(d_1 + d_2) + (d_3 + d_4)], \tag{3.5}$$

where d_i represents the EDM measured for each detector. This method also allowed checking for systematic errors such as voltage on the resonance $\Delta\nu$ and detector counting ΔN, where

$$\begin{aligned} \Delta\nu &= \frac{1}{4}[(d_1 - d_2) + (d_3 - d_4)], and \\ \Delta N &= \frac{1}{4}[(d_1 - d_2) - (d_3 - d_4)]. \end{aligned} \tag{3.6}$$

This gives a compensation factor for the uniform magnetic disturbances [40].

During runtime, there were a number of factors that reduced available measurement time and restricted precision. When large magnetic fluctuations occurred in the experimental hall, the equipment had to be stopped and retuned to bring the magnetic resonances of the top and bottom UCN chambers into coincidence. This resulted in a significant loss of measurement time. The measurement ceased when the reactor was shut down for long term maintenance and upgrade. While the spectrometer was designed to compensate for uniform changes in the magnetic field, it was not designed to compensate for nonuniform change such as those caused by leakage of currents in the chambers. This effect was checked at various frequencies with no dependence found between the leakage current and the compensation factors.

The PNPI-ILL experiment measured d_n with an accuracy of 4.7×10^{-26} e.cm. However, the spectrometer was used at an earlier measurement at the WWR-M reactor, which gave a measurement accuracy of 3.0×10^{-26} e.cm. This gives an nEDM of $d_n < 5.5 \times 10^{-26}$ e.cm at 90% confidence [40]. These measurements had different systematic effects to account for since each measurement was taken with different UCN sources.

3.3 Paul Scherrer Institute

The nEDM experiment at the Paul Scherrer Institute (PSI) in Villigen, Switzerland, used a spallation method of producing neutrons and a solid D_2 moderator [35, 19]. Data collection was completed at PSI in Oct. 2017 and analysis is ongoing for the nEDM measurement [41, 42]. A drawing of the UCN production source is shown in Figure 3.3. This section describes PSI's process of producing UCN [43], and its nEDM experiment.

A 590 MeV proton beam with current up to 2.4 mA (and to a maximum of 20 μA/hr) is incident on the spallation target made of 760 lead-filled Zircaloy tubes. The target is surrounded by ultraclean, heavy water at approximately 300 K. The resultant spallation neutrons are cooled in the surrounding D_2O. Solid D_2 cooled to 5 K is placed at a distance of about 50 cm above the proton beam plane [44] to further downscatter the neutrons to UCN level, via phonon interaction, before entering the storage vessel. UCN left the storage vessel with an additional ≈ 100 neV gain in energy due to the D_2 crystal potential [45]. The 1 m height of the vessel countered this gain in energy and then the UCN entered the 2 m^3 storage vessel coated in diamond-like carbon. UCN

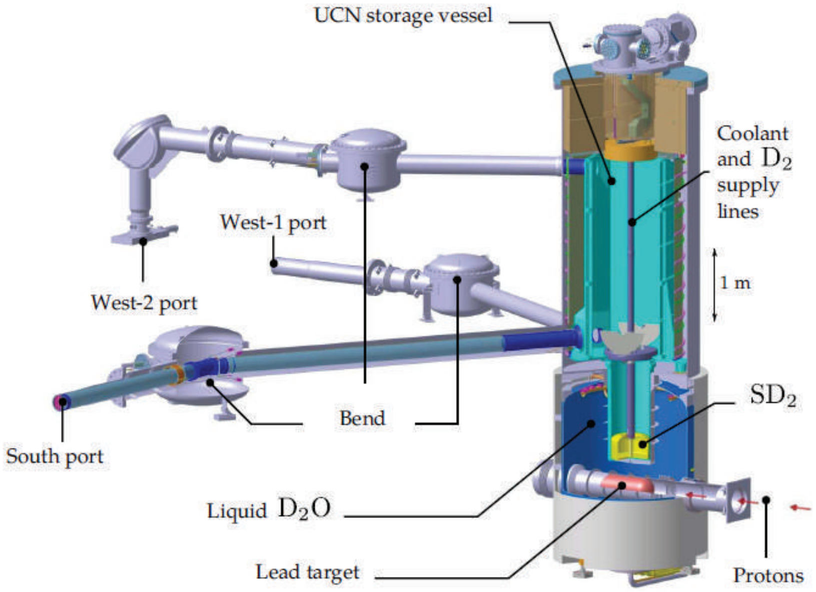

Figure 3.3: UCN source at PSI. Drawing from [19]

were extracted from the storage vessel by three ports that led to the experimental areas.

In transport from the UCN source to the nEDM spectrometer, the UCN passed through a superconducting magnet to polarize the neutrons. After this, the UCN were stored in the nEDM spectrometer. The apparatus consisted of a single precession chamber made of two electrodes and one insulating ring under vacuum [46]. One of the limitations, aside from statistics, was the stability of the magnetic field. This was accounted for by constructing a co-magnetometer within the nEDM apparatus [47]. A “cohabitating” magnetometer, or co-magnetometer, is a system where an additional material, in this case, ^{199}Hg, cohabitates the same space as the UCN and precesses in the same fields as the UCN. UCN collect in the chamber in a gradient of kinetic energies due to the effect of gravity on the UCN, while ^{199}Hg is nearly homogenous in the same space. The ratio of the neutron precession frequency over the mercury precession frequency is an observable that does not depend on magnetic field fluctuations. The ratio of precession rates of both distributions was used to correct for small changes to the magnetic field. Cesium magnetometers are also used to monitor the magnetic field gradient outside the experimental cell. The Ramsey sequence was operated on the UCN in the spectrometer, and the UCN were drained to be counted by a ^{6}Li glass

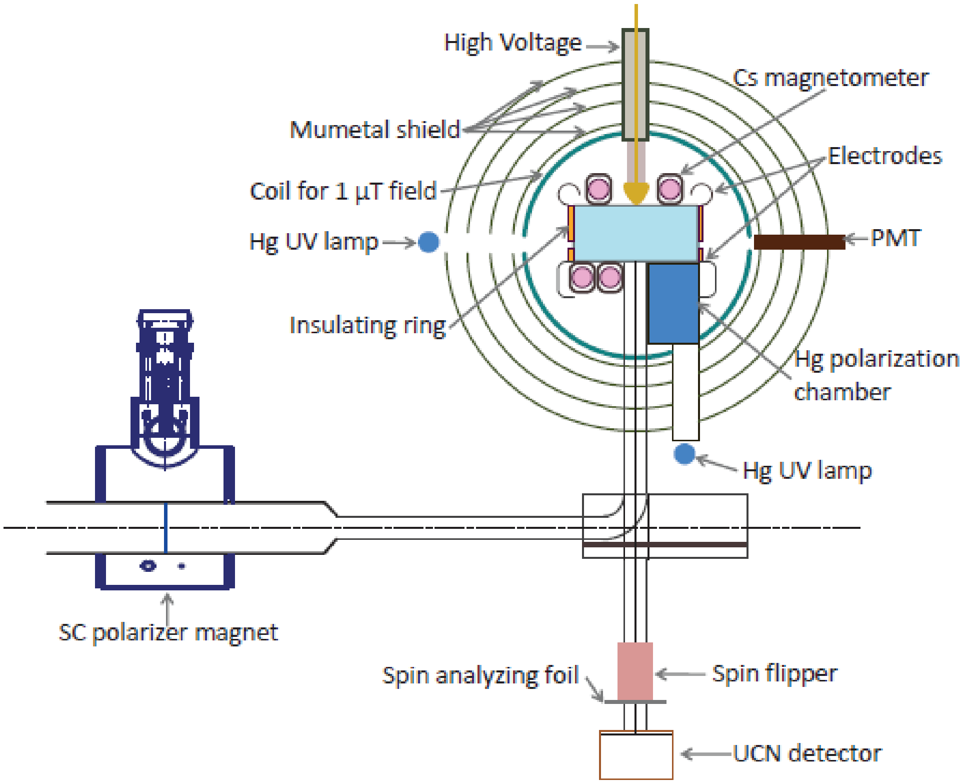

Figure 3.4: nEDM spectrometer at PSI. Drawing from [46].

scintillating counter [46].

Upgrades for the next generation experiment, n2EDM, are discussed in Section 3.4.4.

3.4 Future planned experiments

There are also a number of other experiments at various research and development stages. The experiments discussed here in this section are listed as follows; SuperSUN at ILL, the Spallation Neutron Source at Oak Ridge National Laboratory (ORNL), the UCN Source at Los Alamos National Laboratory (LANL), USA, n2EDM at PSI, PNPI-ILL-PTI collaboration, FRM-II in Germany, and TRIGA UCN source upgrade also in Germany. Most of the focus in development is on upgrades to the UCN source for the specified nEDM experiment.

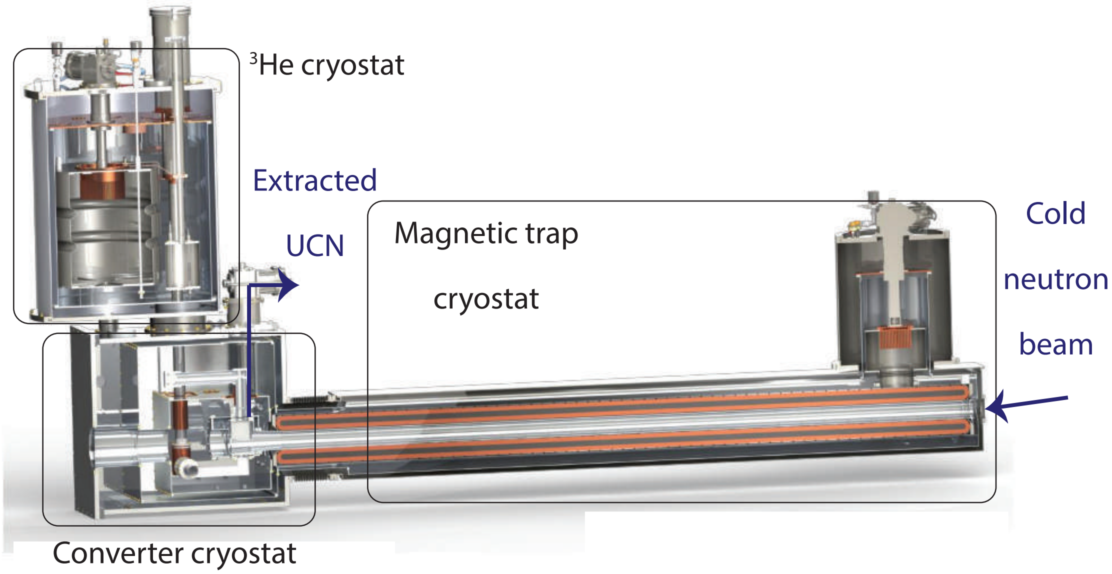

Figure 3.5: Drawing of the SuperSUN UCN Source. The cold neutron beam from PF1B enters the magnetic trap cryostat from the right. The cold neutrons are cooled in the ^{4}He volume here and are directed by the superconducting multipole into the converter cyrostat. The converter cryostat, filled with He-II, downscatters the cold neutrons to UCN level where the UCNs are extracted vertically through the guide via crystal diffraction [52]. The ^{3}He cryostat is for holding an ^{4}He reservoir and cooling. Figure from [51].

3.4.1 SuperSUN and PanEDM at ILL

The ILL has a number of UCN sources. One such source, SuperSUN is the next stage after SUN-1 and SUN-2 [48]. The source extracts neutrons from the PF1B cold neutron beam. The SUN-2 source uses ^{4}He cooled below 1 K. This allows cold neutrons with 0.89 nm wavelength to downscatter to UCN level via single-phonon scattering [49]. Upgrades are ongoing to increase the UCN density to reach up to 1600 UCN/cm^3 from the previous SUN-II density of 22 ± 1 UCN/cm^3 [50, 51]. A drawing of SuperSUN is shown in Figure 3.5.

The nEDM experiment consists of a double precession chamber. As the apparatus is intended to be placed in a magnetically shielded room, co-magnetometers may be unnecessary due to the small magnetic fields, but will be built with a co-magnetometer as a measurement option [51]. Several magnetometers are to be used: ^{199}Hg, Cs, ^{3}He, ^{129}Xe, and SQUID.

3.4.2 Spallation Neutron Source nEDM

The Spallation Neutron Source (SNS) at ORNL is a spallation neutron source with a proton beam impinging on liquid Hg. The resulting spallation neutrons are then cooled into a cold neutron beam by passing through liquid H_2 at 20 K [53]. The cold neutron beam enters a He-II volume to downscatter to UCN level. ORNL finished constructing a new building for the nEDM experiment and has increased the UCN production to the nEDM area by about 40 % due to the shallower bend in the beamline [54]. The experiment is now focused on developing a novel UCN source and an nEDM apparatus.

The nEDM apparatus measures the precession frequency in two ways: free precession and dressed spin techniques or by comparing the precession rates of UCN and ^{3}He. This requires combining the nEDM spectrometer and the UCN detector together. The collaboration has a number of ongoing studies to design and build the apparatus. One prototype study is a systematic and operation studies (SOS) apparatus at PULSTAR in development [55]. Detection system studies include developing the scintillation light readout system and SQUIDs for the ^{3}He precession readout. Other systems being developed include a polarized ^{3}He system, which is used both as co-magnetometer and a detector, and cryogenic magnet system [54]. A drawing of the design is shown in Figure 3.6. Data taking is expected to begin sometime around 2023.

3.4.3 Los Alamos National Laboratory

Los Alamos National Laboratory (LANL) recently upgraded its UCN Source. The basic design of the source remains the same. Spallation neutrons are produced by an 800 MeV proton beam impinging on a tungsten target. The neutrons are moderated by beryllium and graphite moderators and then by cooled polyethylene beads. The resultant cold neutrons downscatter to UCN energies in an SD_2 crystal cooled to 5 K. Since the UCN gain a 100 neV boost when leaving the crystal, the UCN are directed upwards 1 m in a vertical guide before being guided 6 m horizontally to outside of the source's biological shielding. A butterfly valve is placed between the SD_2 crystal and the guides to prevent the UCN from re-entering the SD_2. Upgrades include increasing the

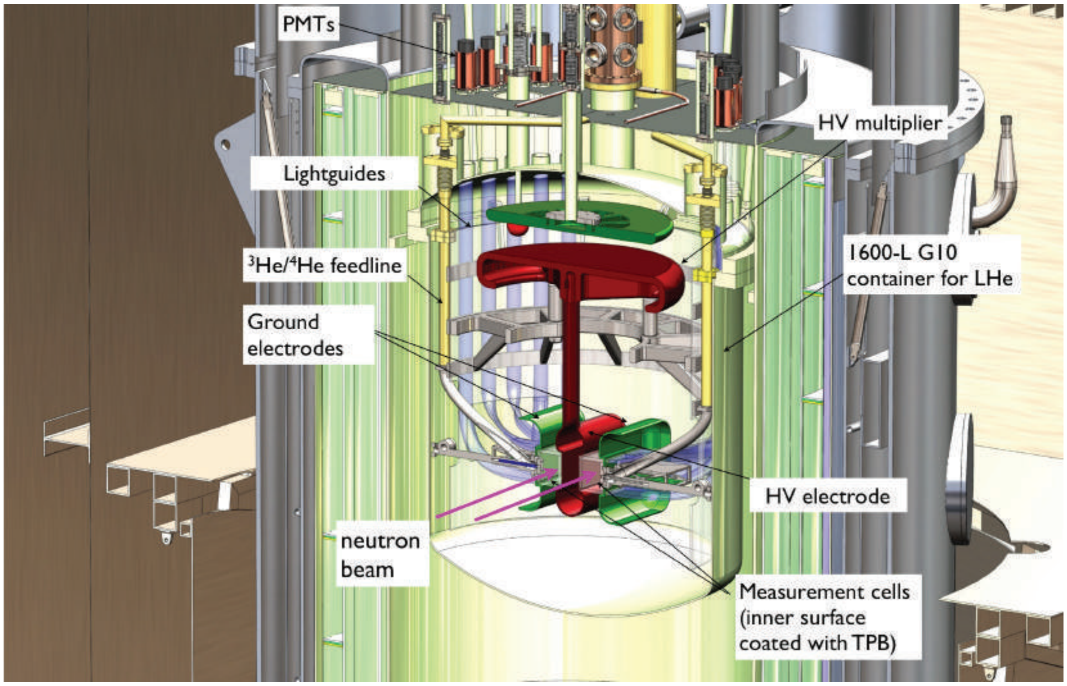

Figure 3.6: Drawing of the nEDM apparatus design for the Spallation Neutron Source at ORNL as of 2016. Figure from [56].

proton current to the tungsten target, building a new cryogenic insert, coating the horizontal guides with nickel phosphorus, and adding another guide to the location designated for the new nEDM experiment. The cryogenic insert includes the vertical guide, the SD_2 crystal, and the cold moderator volume. A new insert is being designed to maximize the UCN density. The measured UCN density after the upgrades was found to be four times higher (184(32) UCN/cm^3) than the previous measured density upon leaving the biological shield (38(7)) [57]. A cutaway view of the source and the insert is shown in Figure 3.7.

The collaboration currently has a working nEDM apparatus [58].

3.4.4 n2EDM at PSI

PSI has begun construction of an improved spectrometer for its n2EDM project that consists of a double chamber based on the design from Gatchina. This spectrometer will take the place of the existing experiment that finished running in 2017. [41].

The main features are the double precession chamber, a laser-based Hg co-magnetometer, ^{3}He

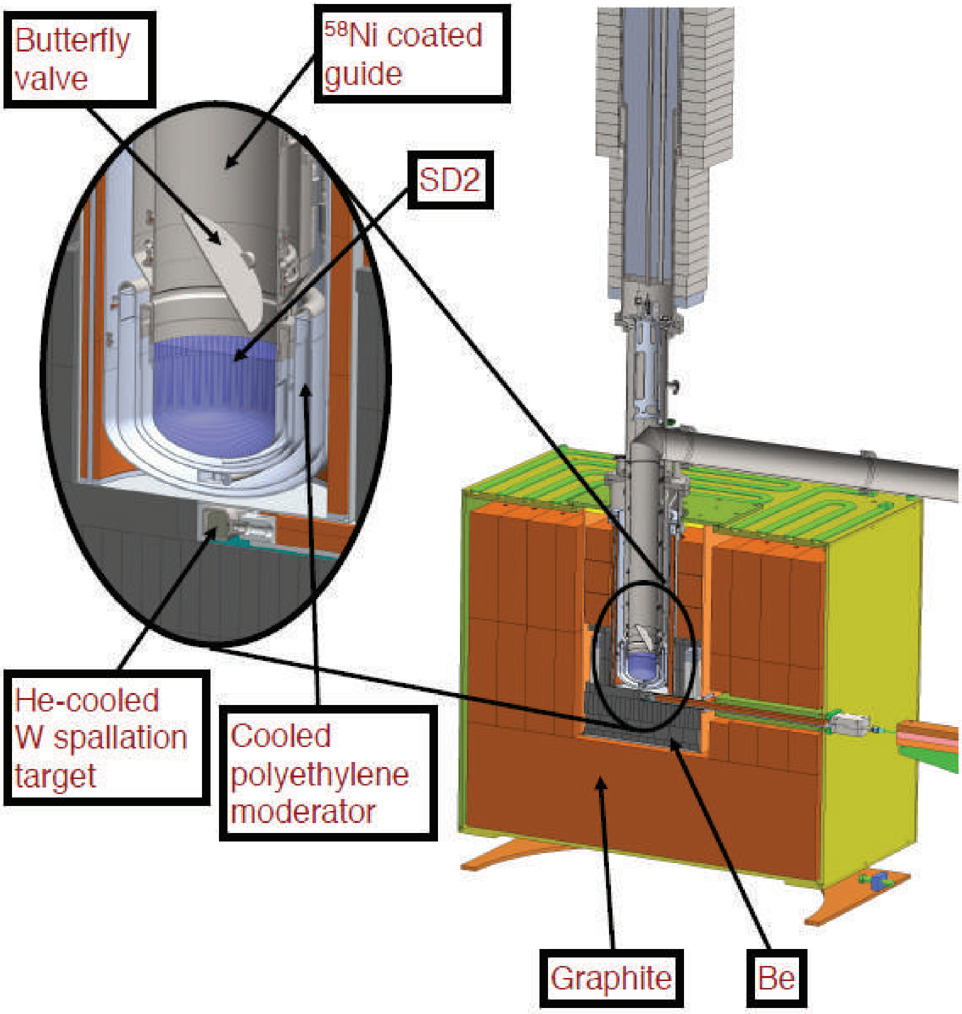

Figure 3.7: Cutaway drawing of the UCN source at LANL [57].

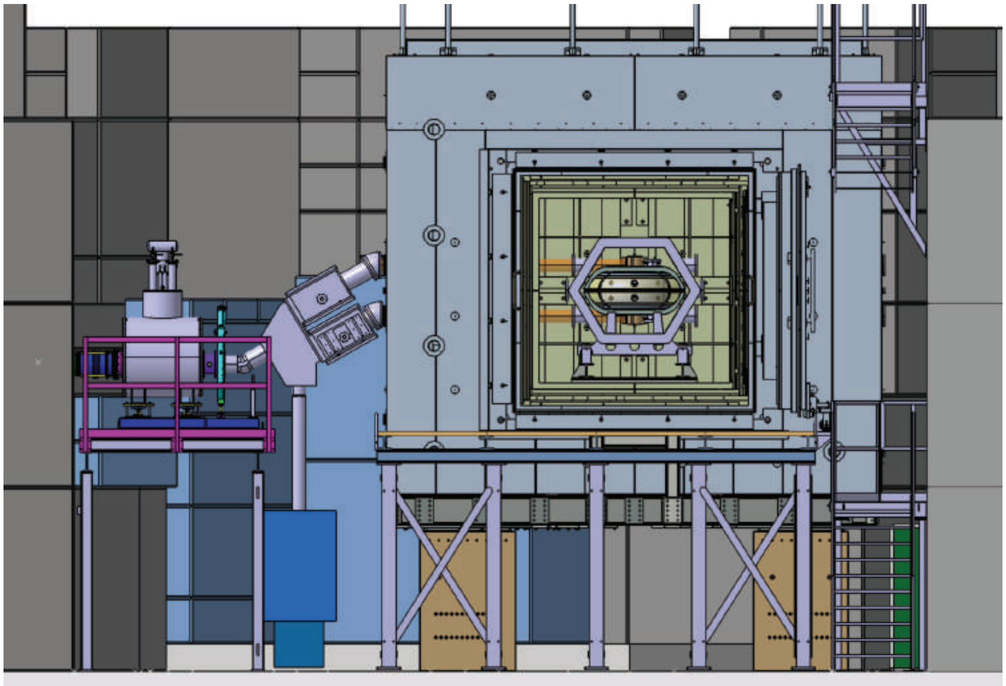

Figure 3.8: Drawing of the proposed n2EDM spectrometer at PSI. This includes the double precession chamber in the middle and the magnetically shielded room [15].

and Cs magnetometers, a magnetically shielded room, large field coils and a high efficiency spin-sensitive detection system [15]. A drawing of the proposed components is shown in Figure 3.8. Possible upgrades to the UCN source are currently under study [41].

3.4.5 PNPI-ILL-PTI at PNPI

PNPI in Gatchina, Russia, is undergoing upgrades to develop the UCN source for a number of neutron measurements, including nEDM [59]. PNPI has its spectrometer located at PF2 in ILL currently, though it may move back to PNPI [9, 40]. PNPI has the currently operating WWR-M reactor and the PIK reactor, which is under construction, for neutron sources. Figure 3.9 shows the planned positions for the various neutron experiments relative to the WWR-M. The WWR-M reactor is more likely to be used for the neutron flux into the UCN source, because the available neutron flux into the UCN source was calculated to be higher for the WWR-M reactor's thermal column than extracting the flux from the PIK reactor [60]. The WWR-M reactor also has a thermal column where a He-II base UCN source can be placed. This would give the spectrometer an

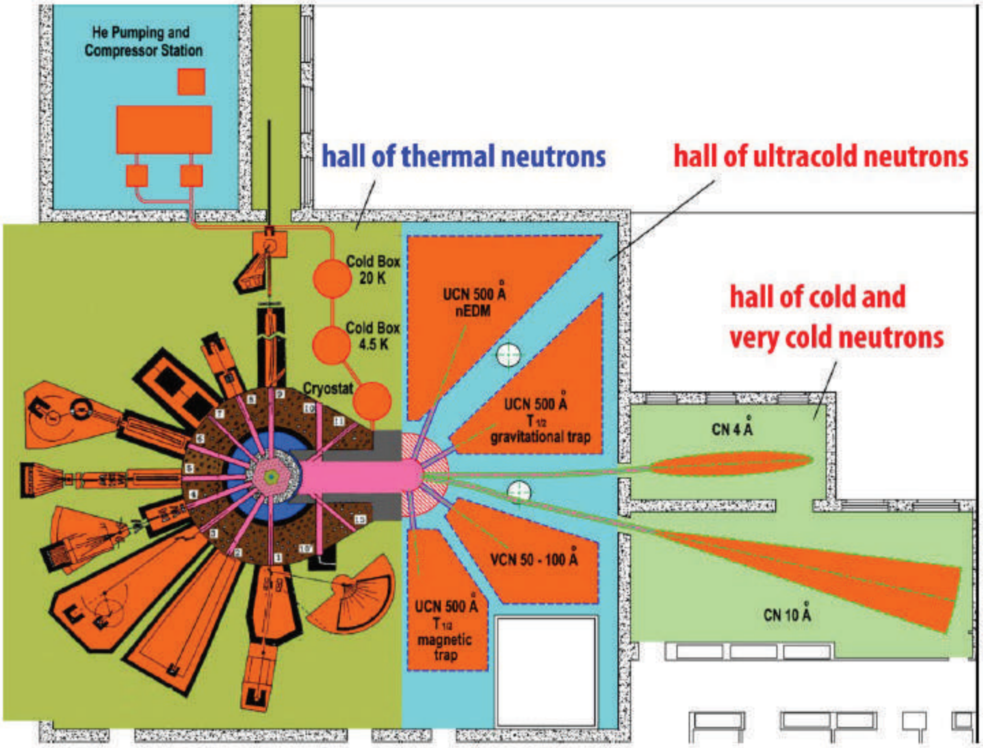

Figure 3.9: Map of WWR-M reactor and experiments. The UCN source would provide a high UCN flux, not only for the nEDM measurement but for a Gravitrap neutron lifetime experiment and a magnetic neutron trap experiment. Drawing from [60].

estimated UCN density of 1.3×10^4 UCN/cm^3.

3.4.6 FRM-II

A UCN source has been under construction at the University of Munich using the FRM-II reactor [61]. The neutron flux comes into the source from a uranium reactor that produces more than 10^{14} n/cm^2/s. The neutron flux for the source are extracted through the SR6 beam tube. The source uses solid H_2 as a pre-moderator [62] to cool the thermal neutron flux to about 40 K. The flux is further cooled to UCN level using solid D_2. A drawing of the source is shown in Figure 3.10.

The EDM spectrometer has multiple levels of magnetic field controls [20, 63]. The facility housing the spectrometer has a magnetically-shielded room with an inner and outer space that can be used separately or slid into each other. Magnetometry includes Cs, ^{199}Hg, and superconducting quantum interference device (SQUID) magnetometers. Spin-exchange optical pumping (SEOP)

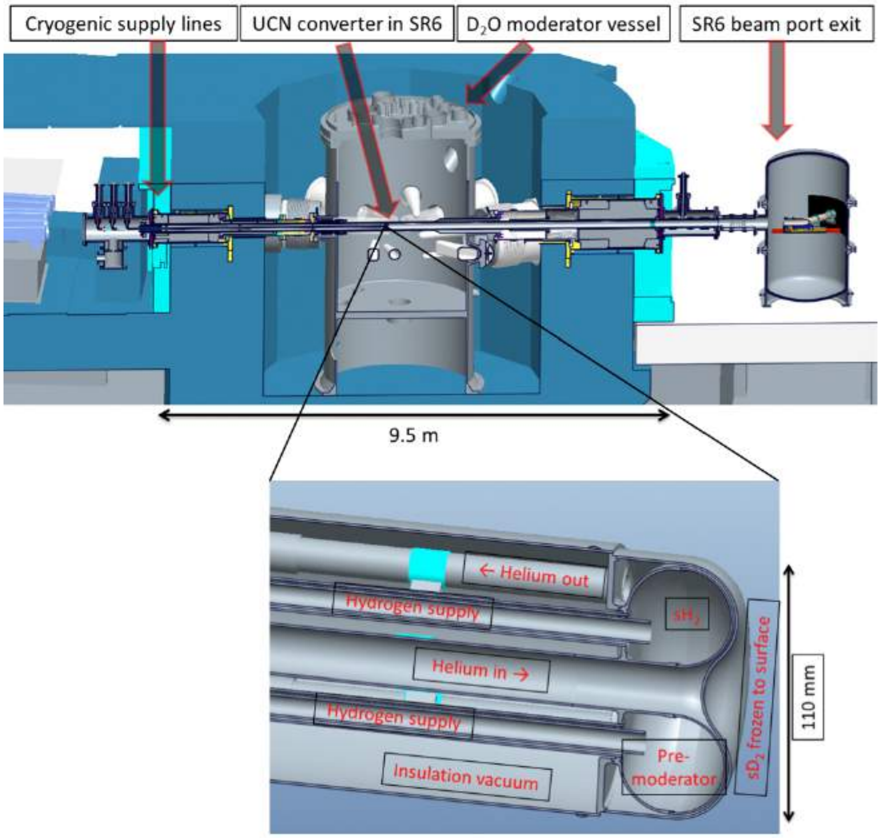

Figure 3.10: Top image is a side view of the beam ports and UCN source at FRM-II. Bottom view is a detailed image of the UCN converter vessel which houses the moderator, He cooling system, sH_2 premoderator and SD_2 moderator. Images from [61].

polarization of ^{3}He and ^{129}Xe is used for comagnetometers [64].

3.4.7 TRIGA UCN source upgrade

The low power reactor TRIGA at Mainz University is being upgraded to become a UCN user facility [26], and will be used for a neutron lifetime measurement. Such a reactor is unique in that it's possible to pulse the reactor every five minutes. The reactor is brought to criticality at a low steady-state power of 50 W before compressed air shoots out a pulse rod from the reactor core. The power rises sharply, but only for a few milliseconds. The solid SD_2 converter is exposed to a neutron fluence of 4.5×10^{13} n/cm^2 and has achieved UCN density of 8.5 UCN/cm^3. Upgrades are aimed toward achieving a UCN density of 50 UCN/cm^3. These upgrades include replacing the He liquefier, the horizontal guide with electropolished stainless steel, and the converter nose with NiMo coating [65]. A drawing of the facility is in Figure 3.11.

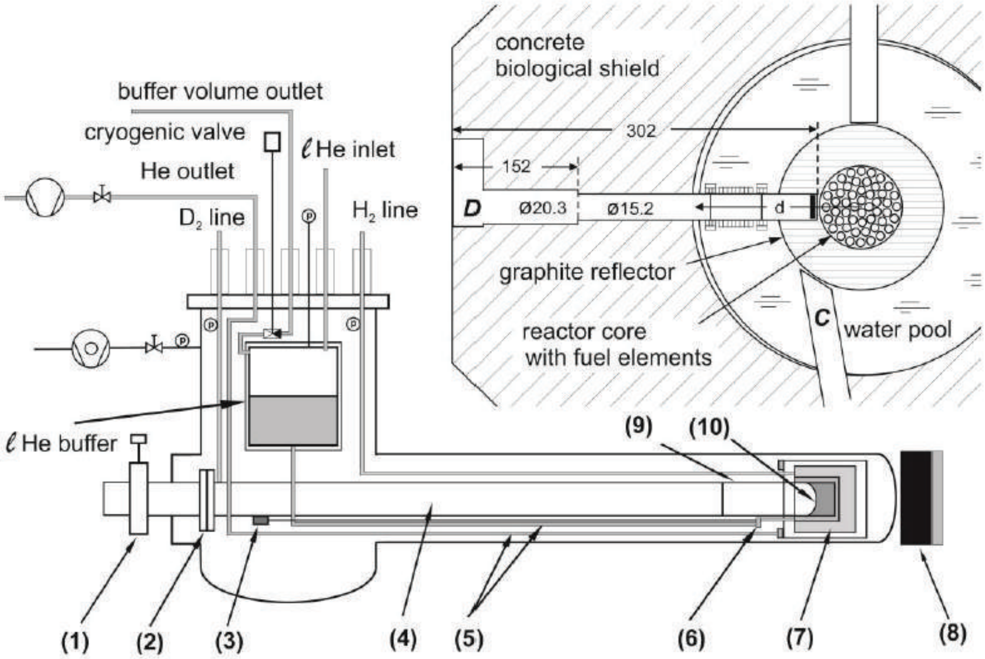

Figure 3.11: Drawing of the UCN Source at Mainz University. Inset is the section of the reactor containing beamport D which is used for the pulse to the source. (1) is the safety shutter, (2) is the alMg_3 foil, (3) is the driver for the Joule-Thomson valve, (4) is the neutron guide, (5) is the liquid He supply, (6) is the Joule-Thomson valve, (7) is the premoderator which is filled with either $\mathrm{H}_2\mathrm{D}_2$ or CH_4, (8) is the graphite/bismuth stopper, (9) is the thermal bridge, (10) is the nose of volume encased with sD_2. Drawing from [26].

Chapter 4

nEDM at TRIUMF

In order to measure the nEDM to high precision, a high density of UCN is required (because $\sigma \propto \frac{1}{\sqrt{N}}$). While free neutrons are readily produced in research reactors via nuclear fission, gathering the number of neutrons required for a longer period of observation is difficult. Spallation neutron sources generate free neutrons using a high-intensity proton beam impinging on a neutron-rich target, such as tungsten. Spallation neutrons at TRIUMF are produced with a 480 MeV proton beam with a current 10-40 μA impinging on a tungsten target. The spallation neutrons at TRIUMF are progressively cooled to UCN temperatures using layers of moderators, which include lead, graphite, warm and cold heavy water, and superfluid He-II. The UCN are then extracted through an aluminum window. This produces a high density of UCN, which are then available for measurement.

Both phases of the nEDM experiment at TRIUMF use this method. The second phase is under development which focuses on improvements in UCN density by changing the heavy-water ice with solid D_2 (surrounding the He-II cryostat), and the design of an improved nEDM apparatus. First, a brief description of TRIUMF (which houses the experiment) is given, then a review of the phase 1 version of the experiment from RCNP is discussed. This includes details regarding the UCN source, TUCAN, and the EDM system. Lastly, improvements on both the source and the EDM system are described in detail, including the calculated improvements in statistics.

4.1 TRIUMF

TRIUMF is located in Vancouver, BC, Canada, and is operated as a joint venture by a number of universities across Canada. The laboratory operates a 520 MeV proton cyclotron that services a number of different experiments, and does radiation therapy. The nEDM experiment is being planned for the TRIUMF UCN Source, which recently measured its first UCN in Nov. 2017 [66]. This chapter provides an overview of the UCN source, called TUCAN for TRIUMF Ultracold Advanced Neutron source, and the nEDM experiment and its stages.

4.2 TUCAN

The UCN source facility has been under construction since 2013, beginning with the decommissioning of the M13 beamline [67]. From then, the new proton beamline constructed between the kicker magnet and the spallation target and test cryostat was completed in 2016. The first protons on target were observed Nov. 1st, 2016, and at the end of 2016, tests were conducted with the proton beam on target, and measurement of the resultant thermal and cold neutron flux.

The cryostat for the UCN source arrived on Oct. 2016, from Osaka, Japan. This is a vertical cryostat which has been used and developed in Japan for the last 15 years [30], rather than the second generation, horizontal cryostat. The Japanese collaborators are working on developing a third generation, horizontal cryostat [67].

TUCAN is a neutron spallation source, with a tungsten target, and He-II UCN production. The UCN group has been working in collaboration with RCNP, the University of Winnipeg, and KEK to build this source. In the fall of 2016, the cold part of the horizontal source was commissioned, as shown in Figure 4.5. The unavailability of the horizontal source, due to incomplete, required safety modifications, meant the vertical source was used for the first UCN production the following year, shown in Figure 4.4. A new, third generation, horizontal source is under development for the next phase of UCN production.

Producing UCN requires several steps. First, the 480 MeV and 40 μA proton beam from the

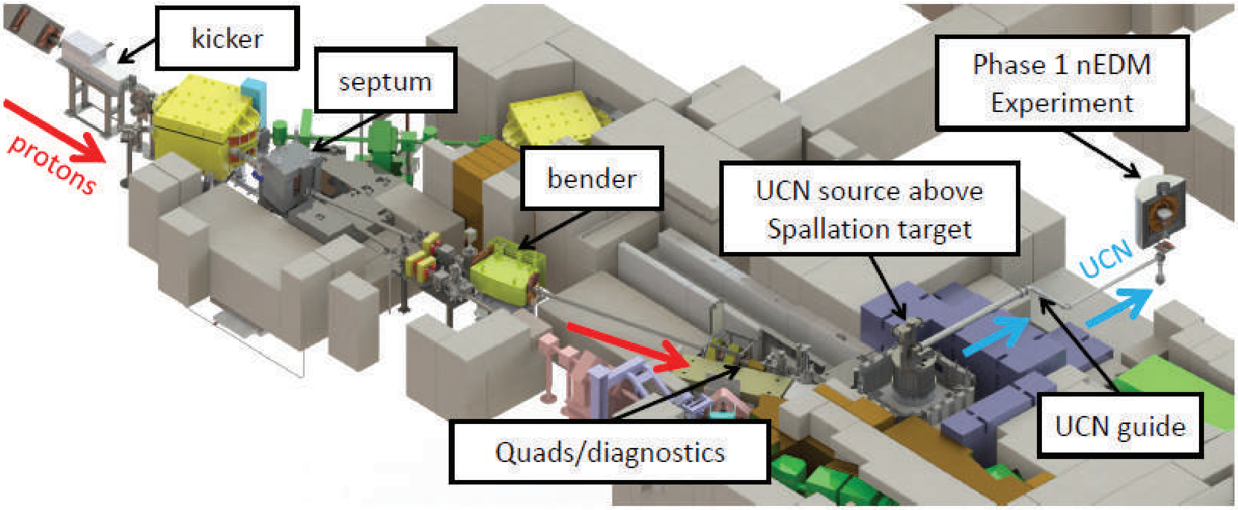

Figure 4.1: View of the Meson Hall housing the UCN source and the nEDM experiment. The proton beam comes from the cyclotron and hits the tungsten target below the cryostat. The resultant neutron flux is then cooled in stages to the UCN level and sent to the nEDM apparatus [67].

cyclotron impinges on the tungsten target as shown in Figure 4.1. This creates spallation neutrons, which are moderated by room temperature lead, graphite, and D_2O, and then 20 K D_2O before reaching the superfluid He volume (He-II) at 0.8 K. The cold D_2O cools a portion of the neutron flux down to cold neutron temperatures. Once the neutrons enter the He-II, the cold neutrons of about 1 meV energy have the greatest probability of downscattering to the UCN range via phonon and roton transitions [29, 67]. A drawing of the source is shown in Figure 4.2. This is the only source that combines spallation neutrons and He-II production volume to produce UCN [67].

4.3 nEDM experiment

For the EDM portion of the experiment, currently in the testing phase, the prototype nEDM apparatus from RCNP was installed for phase 1 [69, 67]. This apparatus was developed in Japan for neutron-spin resonance research and is being used at TRIUMF for testing other new equipment, such as the prototype UCN detector and high-voltage system. The chamber is surrounded by one spherical coil and then four layers of cylindrical shielding. After the UCNs are produced, the UCN that bounce to the top of the cryostat and are guided through a superconducting magnet, which

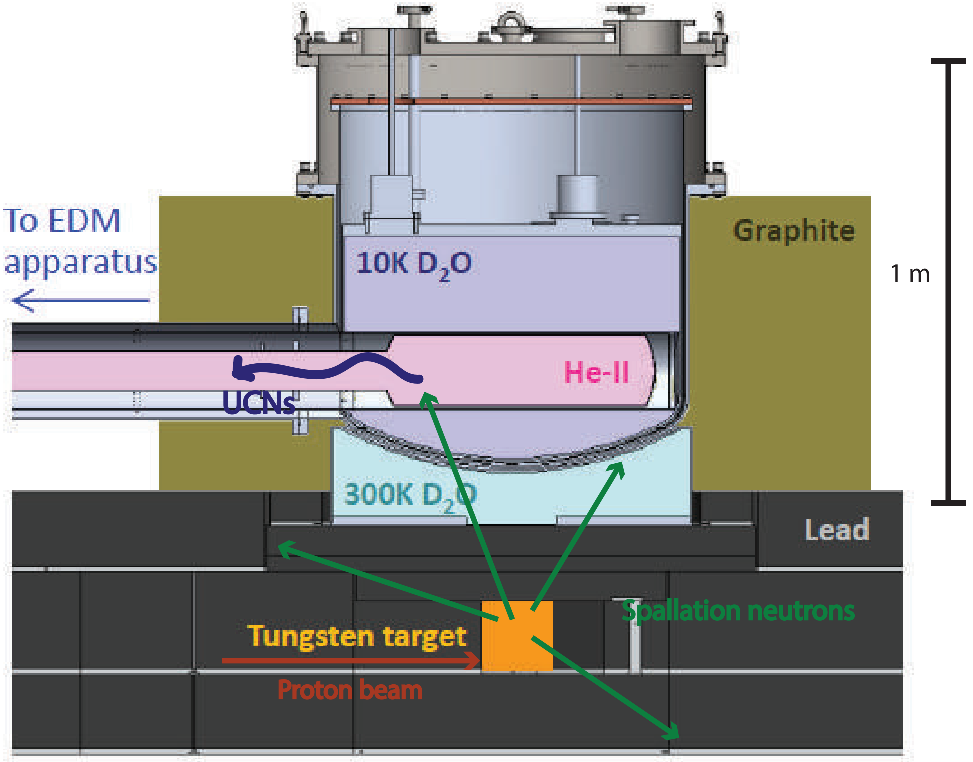

Figure 4.2: Drawing of the first UCN source tested at TRIUMF. The proton beam hits the tungsten target, releasing spallation neutrons. Some of the neutrons are progressively cooled through warm D_2O, cold D_2O, and He-II to UCN energies. Figure from [68].

separates out one, specified polarized state of UCN. The polarized neutrons then fill the storage cell. The bottom of the storage cell is then closed and the Ramsey sequence is performed on the UCN in the storage cell. After completing the sequence, the rotation valve is rotated to drain the UCN to the detector. The UCN in the storage cell of one spin are passed through the analyzer foil into the UCN detector and then the spin flipper is turned on to allow the UCN of the other spin to pass through the analyzer foil; this is called sequential counting. A drawing of the vertical cryostat and the EDM apparatus is shown in Figure 4.4.

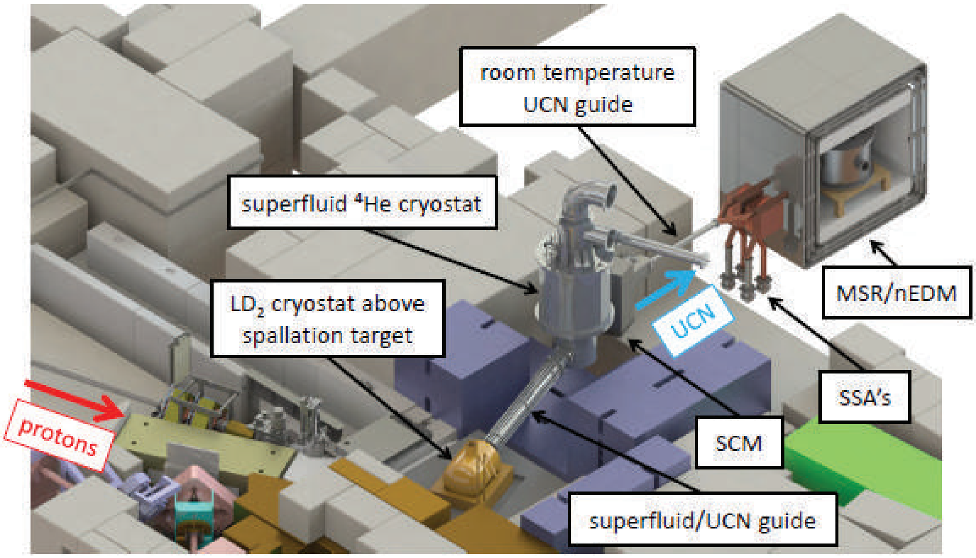

Figure 4.3: Layout of the proposed upgraded experiment from the cryostat to the nEDM apparatus [67].

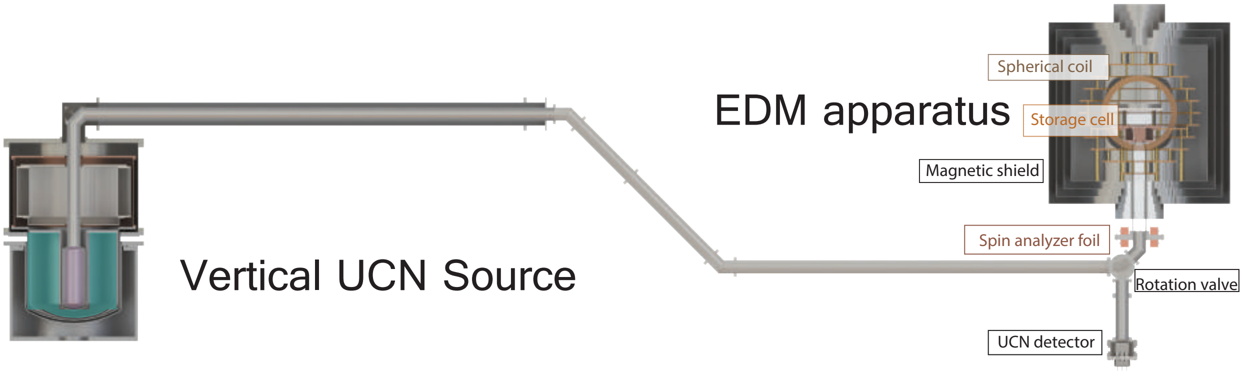

Figure 4.4: Drawing of the current nEDM system using the vertical UCN source and nEDM apparatus in use. Drawing from [70].

4.4 Initial explorations in preparation for an nEDM experiment at TRIUMF

Tests of UCN production with the vertical source were conducted in fall of 2017. In these tests $> 3\times10^5$ UCN per cycle at 10 μA were observed. Testing of the various components in preparation for phase 2 of the experiment occurred throughout the development and installation of phase 1 and continues with the current version of the experiment running. UCN scattering measurements off Ni-plate, NiMo, Diamond-Like Carbon (DLC), deuterated polystyrene (dPS), and deuterated polyethylene (dPE) coatings were completed at J-PARC in 2016 for developing UCN guides. An Xe/Hg comagnetometer is under development. The prototype UCN detector was tested at the UCN facility at PSI.

The horizontal UCN source, without He-II and with three graphite columns surrounding approximately half of the cryostat, was used for moderator testing in cold neutron production tests during the winter of 2016. These tests also included measuring the cold neutron flux, inside the empty He-II volume.

The vertical cryostat has some limitations. For example, the cryostat was not designed for the 40 μA heat load but the lower heatload of 1 μA at RCNP. It also has some steel parts, which become radioactive over time, and extraction of UCN requires the UCN to travel 1.2 m upward, thus reducing the UCN energy window to less than 90 neV. The second generation cryostat corrects these limitations, but does not have the required safety modifications completed.

4.5 TRIUMF plan for TUCAN nEDM measurement

A new horizontal UCN source is being built which uses liquid D_2 in place of the existing D_2O moderator, and the moderated neutrons will then be further cooled in the new horizontal He-II cryostat. The nEDM apparatus has a number of upgrades, including multiple experiment cells, improved shielding, and four UCN detectors. A drawing of the potential upgrades is shown in Figure 4.5.

4.5.1 Horizontal UCN source

The third generation superfluid helium cryostat is similar to the horizontal cryostat but with a number of improvements to increase UCN production and extraction. One of the upgrades is the improved heat exchanger design and improved cooling efficiency and internal neutron guides. This bottle is proposed to be made of Be in place of the current Al bottle, as Al presents the largest γ and β heat load to the He-II [67]. With the design modifications, the cold windows may be removed

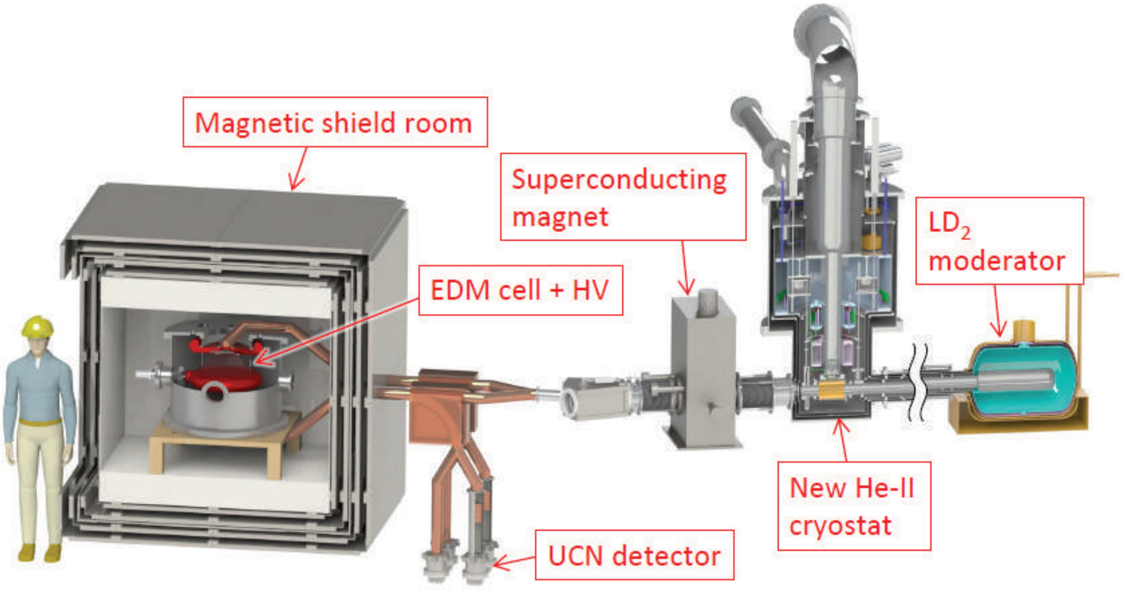

Figure 4.5: Drawing of the planned upgrades to TUCAN and the nEDM apparatus. Drawing from [68].

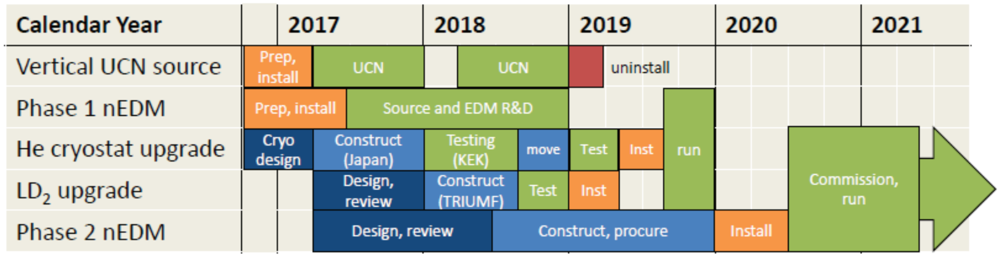

Calendar Year	2017	2018	2019	2020	2021
Vertical UCN source	Prep, install UCN	UCN	uninstall		
Phase 1 nEDM	Prep, install Source and EDM R&D		run		
He cryostat upgrade	Cryo design Construct (Japan)	Testing (KEK) move	Test Inst		
LD_2 upgrade	Design, review	Construct (TRIUMF) Test	Inst		
Phase 2 nEDM	Design, review	Construct, procure		Install Commission, run	

Figure 4.6: Timeline of proposed upgrades. Phase 1 of the nEDM measurement is scheduled to run until 2019. The next phase is expected to be operational in 2020 [67].

between the He-II volume and the vacuum extraction volume. The cold windows were present for the second generation cryostat, but not the first generation cryostat, due to its vertical bottle design.

Another component change is the use of liquid deuterium (LD_2) in the cold moderator in place of the previous solid D_2O. This is to increase the 1 meV neutron flux into the He-II by 5 to 9 times and further reduce the heat load to the He-II. Using the cold neutron flux in this design and the calculations in [71], the resultant UCN flux is projected to be $\approx 2 \times 10^7$ UCN/s [67].

4.5.2 nEDM apparatus upgrades

A number of improvements are also planned for the EDM portion of the experiment particularly for magnetic stability and addressing systematic effects. One major improvement regarding the magnetic stability is the addition of a four-layer magnetically shielded room. This room includes self-shielded coils as the basis for the high precision coil system and replaces the cylindrical shields providing more space for the experiment. The self-shielded coils will produce $B_0 = 1 - 2\mu$T in the expected cell. Inside the inner experimental shield, AC coils provide the fields for the free spin precession portion of the Ramsey sequence. UCN are transported into and out of the chambers using guides with special material coatings (NiMo) that have a high $V_F \sim 250$ neV. Saddle-shaped coils along the UCN guides are used to ensure the adiabatic requirement $\frac{1}{\gamma|B|}\frac{\partial B}{\partial t} \ll \frac{\mu B}{\hbar}$ in the region of the spin flipper.

The spectrometer itself has a dual chamber, vertically stacked; each chamber has a diameter of 36 cm, and a height of 15 cm. These chambers are housed in a non-magnetic vacuum chamber, and each chamber is separated by a wall of dielectric insulator. This set-up gives a first-order correction for the magnetic field. ^{199}Hg and ^{129}Xe are used as the comagnetometers; Cs is used as an external magnetometer. Adding the ^{199}Xe gives an additional measurement of the magnetic field from the^{129}Xe magnetic moment. The Xe/Hg system utilizes the precession frequencies of both species together and give a false EDM term according to $\partial B_z/\partial s$, where s is the spin [72, 73].

After the Ramsey sequence is performed on the UCN, the spins are to be separated using simultaneous spin analyzer systems (four in total, such as seen in the PNPI spectrometer). The UCN are then counted, using four ^{6}Li glass counters for simultaneous counting. This is to maximize the counting efficiency and the visibility of the Ramsey fringe.

Transport efficiency is expected to be 4 % or about 680 UCN/cm^3 for a total of 2.1×10^7 UCN [67]. Factoring in the neutron lifetime, spin-coherence in the EDM cells, and the eight-fills cycle required to determine the points of the resonant frequency, a statistical sensitivity of $\sigma(d_n) = 5.6 \times 10^{-26}$ e.cm per cycle is predicted. Fourteen hours of stable running, per day, would reach a sensitivity of $\sigma(d_n) = 10^{-27}$ e.cm after about 100 days of running.

4.6 Thesis foci

This thesis focuses on two aspects of the nEDM experiment. One focus is on the UCN detector. The UCN density is expected to be high, therefore the detector used must be capable of handling high instantaneous rates. The other focus is on the thermal neutron flux measured for the horizontal cryostat without the He-II generated with the D_2O moderator. This is measured with Au with and without Cd to determine the thermalization effect of surrounding the moderator with graphite. These measurements were done at the same time as a multiple metal foil measurement to determine the cold neutron flux inside the moderator.

Part II

^{6}Li glass detector

Chapter 5

Prototype UCN detector

UCN are typically detected via neutron capture. Certain nuclei (e.g. 5330 bn for ^{3}He, 940 bn for ^{6}Li, and 3840 bn for ^{10}B for thermal neutrons [74]) have higher neutron capture cross-sections at low neutron energies that increase in cross-section as the speed of the neutron decreases, or $\sigma_{abs} \propto 1/v$. The resultant, charged particles are then collected to give a measurable signal.

Historically, ^{3}He gas detectors were used for detecting UCN [74]. As the density of generated UCN increased, however, new types of detectors were developed. The four main challenges when developing UCN counters for these new sources [74, 75] are:

- obtaining high neutron detection efficiency,
- maintaining efficiency stability,
- rejection of backgrounds, and
- radiation hardness.

The following sections describe the different types of available UCN counter technology.

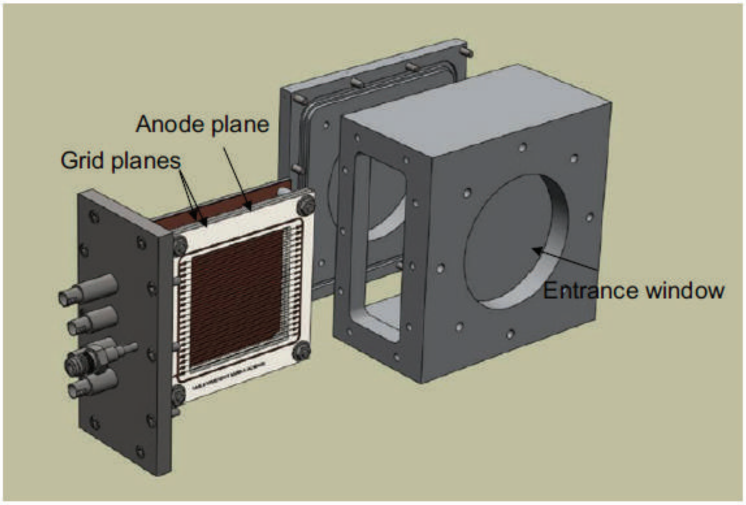

Figure 5.1: ^{3}He detector developed at Los Alamos. The drawing here shows the detector partially disassembled [76].

5.1 ^{3}He gas detectors

^{3}He has a high thermal neutron capture cross-section of 5330 bn [74]. The capture reaction is

$$n + {}^3\mathrm{He} \to p + {}^3\mathrm{H} + 764\ \mathrm{keV}. \tag{5.1}$$

The resultant particles then ionize the gas mixture (usually Ar/CH_4 or Ar/CO_2) to produce the signal.

^{3}He gas detectors have most commonly been used with previous UCN sources and continue to be used today. The main advantages to using this detector is that the technology is well developed and, since ^{3}He is a low Z material, it has low sensitivity to background. However, ^{3}He gas detectors generate a signal 2 μs long or longer. Even with segmentation, ^{3}He detectors have too much pile-up at high intensity sources.

5.2 Gas electron multiplier (GEM) detectors

Gas electron multipliers (GEM) technology is also used for UCN detection [77]. A GEM foil is comprised of a grid of two metal layers separated by a thin insulator with etched channels. Each

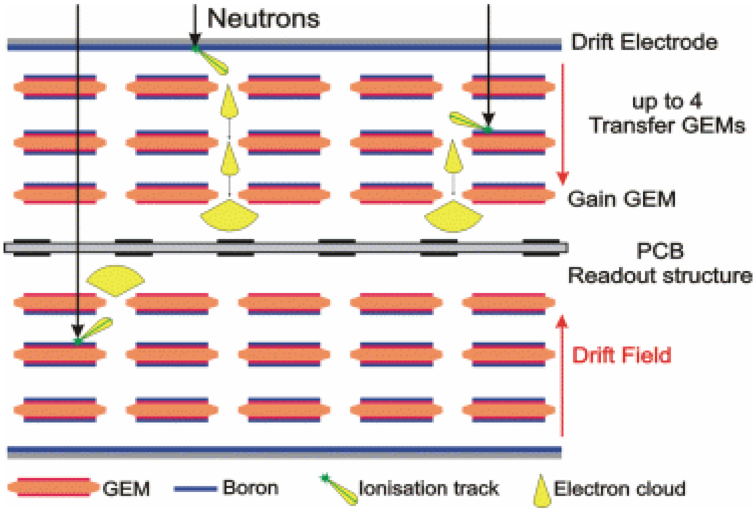

Figure 5.2: Drawing depicting a number of layers of GEM foils and the ionization method of a GEM detector. This particular detector has the layers cascading behind the Boron layer and are called Cascade detectors from Cascade Detector Technologies [78]. A CASCADE-U model was tested with the ^{6}Li prototype detector in the PSI tests.

layer is kept at different potentials within the volume of a gas. The foils pre-amplify electrons going through the channels, giving a larger signal.

For example, the Cascade detectors [78] use a layer of ^{10}B coated onto the Al window, which has a thermal neutron capture cross-section of 3840 bn [74], multiple layers of GEM foils, and a gas mixture of Ar/CF$_4$. However, the capture reaction has two branches:

$$n + {}^{10}\mathrm{B} \rightarrow \alpha(1.78\,\mathrm{MeV}) + {}^{7}\mathrm{Li}(1.01\,\mathrm{MeV})[6.4\%], \tag{5.2}$$

$$n + {}^{10}\mathrm{B} \rightarrow \alpha(1.47\,\mathrm{MeV}) + {}^{7}\mathrm{Li}(0.84\,MeV) + \gamma(0.48\,\mathrm{MeV})[93.6\%]. \tag{5.3}$$

The resultant charged particles enter the gas volume and produce e^{-}-ion pairs. The electrons are amplified by gas amplification as they are accelerated through the GEM foil channels, to give the signal. Since this detector also uses low Z materials, the sensitivity to background is low, as is its sensitivity to magnetic fields. This detector is available commercially, including readout electronics.

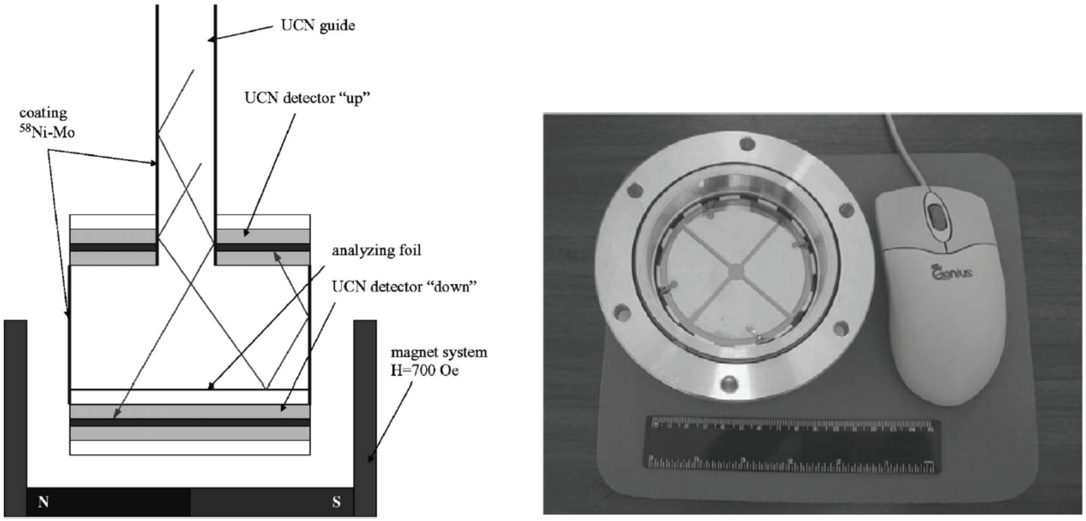

Figure 5.3: This is the silicon solid state detector developed by PNPI. To the left is a drawing of the components of the detector and to the right a photo of the completed detector [80].

5.3 Silicon solid state detectors

Silicon solid state detectors utilize a layer of ^{6}LiF and a silicon semiconductor. The ^{6}Li has a thermal neutron capture cross-section of 940 bn and a much higher cross-section of the order of 10^5 bn for UCN [79, 74]:

$$n + {}^6\mathrm{Li} \rightarrow \alpha(2.05\,\mathrm{MeV}) + {}^3\mathrm{H}(2.73\,\mathrm{MeV}). \tag{5.4}$$

Defects can occur after long neutron exposure and reduce energy resolution [74].

5.4 Scintillator detectors

Scintillator detectors use scintillating glass doped with ^{6}Li. The absorption of neutrons and decay is the same as in Equation 5.4, and with the same energy in the resultant particles. The resultant particles, however, interact with the surrounding scintillating material, which contains Ce^{3+}. Activating the Ce^{3+} sites with the resultant particles emits blue light with a maximum wavelength of 395 nm [74, 75, 81]. The light can then be collected via lightguides and directed into photomultiplier tubes.

The main advantage is the ability to detect at high rates, as the decay time of the signal is 50-70 ns [74, 75, 81] although there is a slower decaying light component up to 1 μs. The glass is also shown to not decay in signal over a high neutron dose [81]. The glass does pick up background, but the signal shape can be discriminated from the background. Also, by using very thin scintillators, the background is reduced, both by γs and thermal neutrons. Detailed studies of the ^{6}Li detector area discussed further in Chapter 6.

Chapter 6

^{6}Li glass and UCN

The type of detector chosen for the nEDM prototype counter uses ^{6}Li scintillating glass. ^{6}Li has a high neutron absorption cross-section of order 10^5 bn for UCN. The capture reaction is shown in Equation 5.4.

The different components of the prototype detector are described below. The basic design was inspired by a similar detector in use at PSI [75, 81]. Particular focus on manufacturing and testing the ^{6}Li glass surface is detailed in the following section, the testing of the optically-bonded glass is in Section 6.2, and the remaining components and assembly of the prototype detector are in Section 6.3.

6.1 ^{6}Li optically bonded glass

The detector is two optically-bonded pieces of glass. The top 60 μm layer of scintillating glass contains only ^{7}Li (^{6}Li depleted) and is called GS30 by the manufacturer. The bottom 100 μm contains only ^{6}Li and is called GS20 by the manufacturer. The concentrations of ^{6}Li in the top GS30 and bottom GS20 layers are listed in Table 6.1. In the bottom layer, the neutrons have an interaction length of approximately 1.6 μm. This is done so that the neutrons penetrate the glass before being absorbed by the ^{6}Li, and thus, the resultant particles propagate completely within the glass to give the maximum signal. Figure 6.1 shows a number of potential interactions in the glass,

Table 6.1: Table showing the ^{6}Li content of the two scintillating glasses used [82, 83].

Scintillator	GS20 ^{6}Li enriched	GS30 ^{6}Li depleted
^{6}Li fraction (%)	95	0.01
^{6}Li density (cm^{3})	2.2×10^{22}	2.4×10^{18}

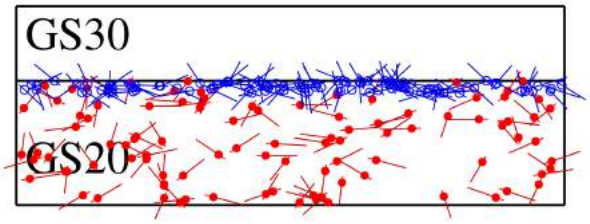

Figure 6.1: Graphic demonstrating UCN absorption behavior in optically bonded glass. The GS30 layer is ^{6}Li depleted while the GS20 layer is ^{6}Li doped. Since the top layer is ^{6}Li depleted, the UCN drop to the lower layer and absorb either right on the boundary with highest probability (blue) or further into the lower layer (red). The lines show example directions of where the resultant triton and alpha particles decay, showing the majority of particles staying within the scintillating glass and generating the maximum signal.

where the concentration of interactions is at the boundary between the GS30 and GS20 in blue, and other possible interactions in the GS20 glass only are in red.

The glass is kept thin so that it is more transparent to thermal neutrons, which have a much longer interaction length. The mean distance of the α and the triton are 5.3 μm and 34.7 μm, respectively. As a result, the glass must still be a minimum of 40 μm, in order to capture the full scintillation light.

The two layers of glass are optically bonded to remove any signal loss from neutrons capturing in glue, or light loss from the α or ^{3}H crossing additional glue boundaries. Optical contacting of the glass was done by Thales-Seso in France. Backgrounds do appear in the signal output (largely due to gamma interactions with the light-guides). The backgrounds (due to the two-layer design show interactions in the light-guides) are much faster than the scintillator signal as seen from the oscilloscope shown in Figure 6.2. The glass has also been shown to be resistant to radiation damage, to the order of 10^{12} n/cm^{2} [81].

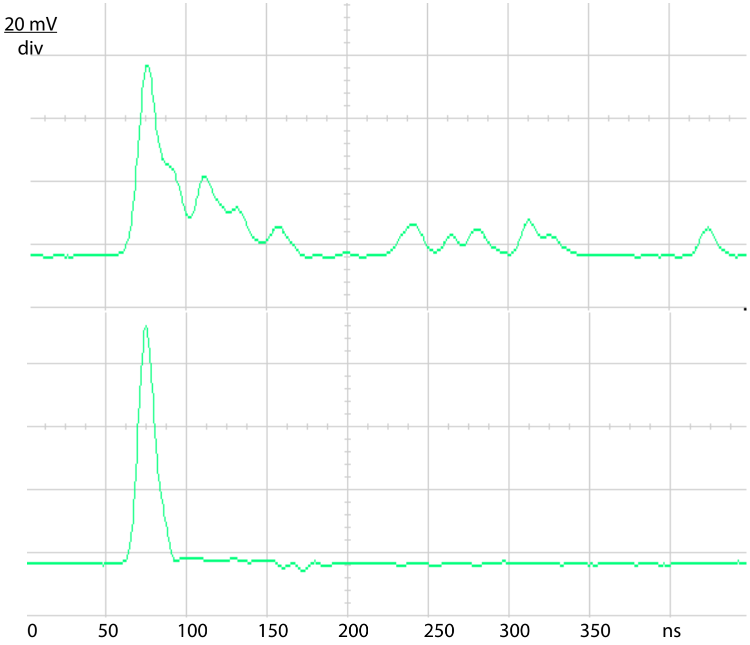

Figure 6.2: Two example signals from the detector. The top figure shows a neutron signal in the scintillating glass and the bottom figure shows a background signal in the light-guide. The neutron signal is measurably larger and has a long tail compared to the background.

6.2 Testing ^{6}Li content on each side of glass

In order to deduce which side of the glass stacks contained ^{6}Li, a test was conducted [84]. First, a box was lined in borated wax blocks. Inside the wax box was placed a Si-detector apparatus and two thermal neutron sources with each source's holders, one 37 MBq AmBe contained in lead and one 185 kBq ^{252}Cf contained in plastic, to generate the thermal neutron flux inside the box. Two sources were used to produce a higher rate of thermal neutrons than was otherwise available in the lab. The borated wax was served to further thermalize the neutrons. The Si-detector apparatus was an Ortec A-016-025-500 partially depleted silicon surface barrier detector. The Si-detector was placed inside a dark metal bell. One side of the glass was placed as close as possible to the Si surface barrier detector inside the bell (≈ 1 mm. The Si-detector was biased with a voltage of $+140$ V, to produce a 0.5μm thick depletion region to detect the energy deposit of either an α or ^{3}H particle. The top was then covered with more borated wax. A drawing of the experimental set-up is shown in Figure 6.3.

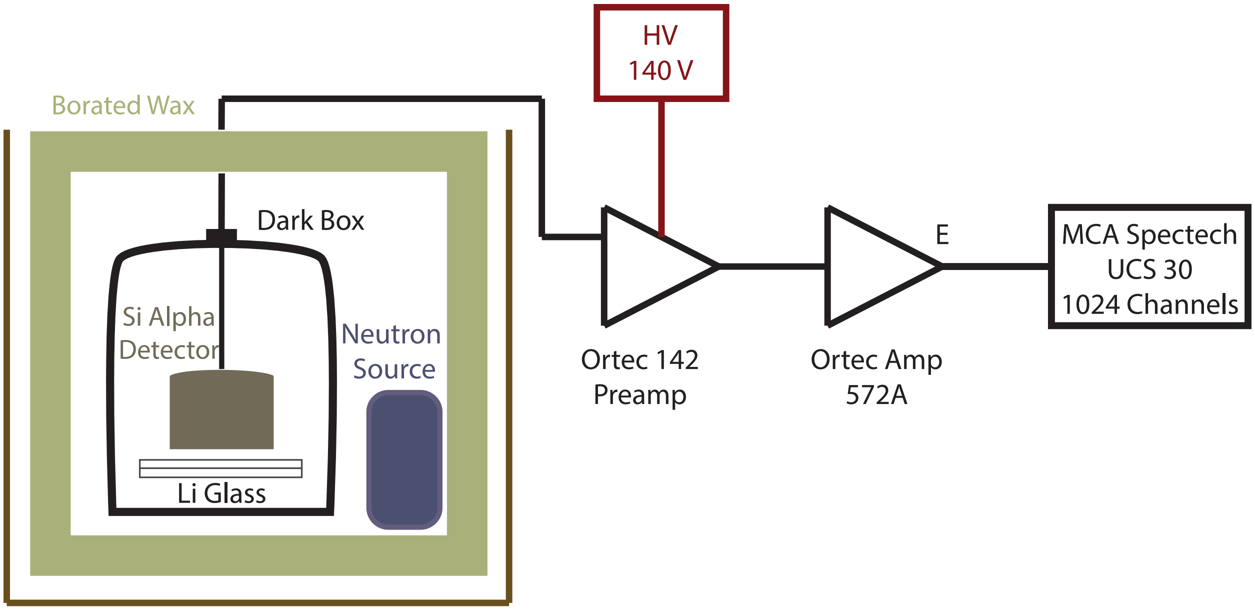

Figure 6.3: Experimental set-up for determining ^{6}Li concentration according to measured side of glass. The glass was placed close to a Si α detector with a thermal neutron source nearby. If a neutron was absorbed in the surface of the glass near the detector, there would be a probability that the resultant α particle propagates into the detector, giving a signal.

The signal from the Si-detector was first sent through an Ortec 142A pre-amplifier, which was then amplified by an Ortec 572A spectroscopy amplifier, before being sent to a 1024 channel SpecTech Multi-Channel Analyzer (UCS-30 spectrometer) to produce the energy deposit spectra. To calibrate the energy deposit spectra, four known α sources were placed near the Si-detector in place of the glass: A ^{241}Am surface α source, a ^{210}Po thin window α source, a thin window ^{137}Cs electron conversion source, and a thin window ^{207}Bi electron conversion source. Two of the sources had more than one energy possible, resulting in more than one peak in the spectra. The area normalized output from the analyzer for all the calibration sources and the resulting energy calibration is shown in Figure 6.4.

When a thermal neutron captures on the surface of the ^{6}Li glass side set close to the Si-detector, either the resultant α or ^{3}H particle may escape the glass surface and would be instead captured on the Si-detector surface, generating the signal. Both the α or ^{3}H particle have more than enough energy to reach the Si-detector and deposit any remaining energy into the signal. This only occurs when the GS20 (^{6}Li-doped glass) side is near the Si-detector.

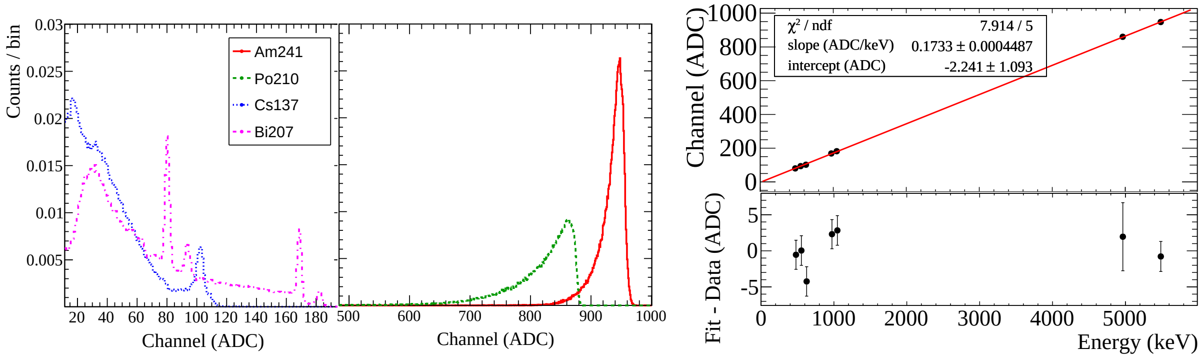

Figure 6.4: The signal from the Si detector was calibrated with four known sources. These data peaks were used to convert the channel ADC values into keV [84].

Three types of tests were conducted: with the GS30 near the Si-detector, with the GS20 near the Si-detector, and with no glass near the Si-detector.

The first two types of tests were conducted for all the glass pieces for the data collection period of 24 hrs for each individual test. The background test was conducted once with a data collection period of 24 hrs. For each piece of glass, the data for the ^{6}Li-doped and depleted sides was normalized and then compared to the background data. The data with the ^{6}Li-doped glass near the Si-detector showed a clear excess of signal, while the ^{6}Li-depleted data was comparable to the background data for each piece of glass. Figure 6.5 shows the summed data comparison, showing the excess signal produced from the ^{6}Li-doped side. The energy range of the excess signal is between 1300 and 2900 keV, which goes above the expected energy of the α particle. The ^{3}H has more energy than the α particle, and thus, provides more energy to the spectrum.

In order to determine the ^{6}Li neutron capture signal, a fit was developed that modelled the sum of the α and ^{3}H signals as two Gaussians with exponential tails over an exponential background of the form $e^{A/E+B}$, with A and B determined from fitting the ^{6}Li-depleted data for the specified piece of glass. The sum of the data was fit first, with parameters being allowed to vary. Then the data from each piece of glass was fitted with only the background, α and ^{3}H, allowed to vary. The different signal and background fits were due to variations in data collection time. To account for uncertainties in the model, the uncertainties in the counts found by integrating the function over the range of 1.3 to 2.9 MeV was increased be a factor of $\sqrt{\chi^2/DOF}$, determined from the fit. The

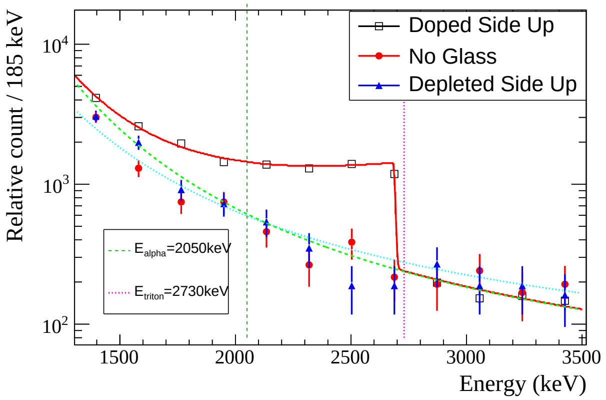

Figure 6.5: This graph shows a comparison of the signal counts according to energy for no glass, glass with the ^{6}Li depleted side close to the Si detector, and glass with the ^{6}Li doped side close to the detector. There is a measurable excess of signal within the energy range of the α particle from neutron capture [84].

results of the fit are shown in Figure 6.2.

Sample	χ^2 / DOF	p-value	Signal (S)	Background (B)	S/B
All	$20.50/6$	0.002	5527 ± 235	5299 ± 135	1.043 ± 0.044
0	$17.26/9$	0.045	1206 ± 75	867 ± 41	1.39 ± 0.09
1	$16.73/9$	0.053	402 ± 41	257 ± 22	1.57 ± 0.16
2	$11.21/9$	0.262	526 ± 37	293 ± 19	1.80 ± 0.13
3	$15.01/9$	0.091	315 ± 41	355 ± 24	0.89 ± 0.12
4	$9.90/9$	0.359	878 ± 50	707 ± 28	1.24 ± 0.07
5	$4.78/9$	0.853	1039 ± 40	970 ± 23	1.07 ± 0.04
6	$8.40/9$	0.494	422 ± 31	316 ± 17	1.34 ± 0.10
7	$2.82/9$	0.971	413 ± 18	310 ± 10	1.33 ± 0.06
8	$9.59/9$	0.385	444 ± 38	449 ± 22	0.99 ± 0.08
9	$6.97/9$	0.640	347 ± 28	315 ± 16	1.10 ± 0.09

Table 6.2: Fit results showing the integrated signal and background data for each of the 10 samples tested, and the sum of all samples. Table from [84].

In this way, all pieces of glass were verified to contain the ^{6}Li on the specified side and if the labels for the sides were lost, the sides could be tested again.

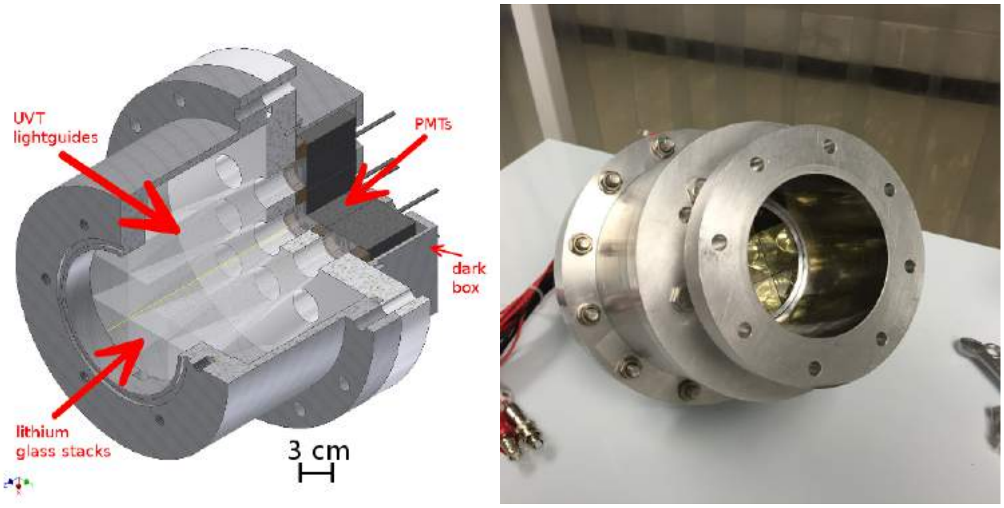

Figure 6.6: Final design of the UCN detector shown with cutout to the left and a photo of the assembled detector to the right. The plot on the right also has an adapter flange attached to it for use in the tests at PSI.

6.3 Signal and housing components

This section details the prototype detector's signal transmitting components and housing. The environment where the detector is to be placed has γ background and thermal neutron flux as well as other sources of noise. For this reason, the detector is designed to be placed under vacuum and light-tight with the UCN guides and the resultant signal is sent out of the detection area.

Figure 6.6 shows a cutout drawing and a photo of the final prototype.

6.3.1 Signal components

The glass face of the detector is segmented into 9 channels, in order to handle up to 1 MHz of neutrons. When a neutron is captured, the scintillation light is collected in ultra-violet transmitting acrylic light-guides to be sent outside of the vacuum portion of the detector housing to the Hamamatsu R7600U PMTs. Each PMT has a voltage of approximately 900 V. The signal is then sent to the electronics. Photos of the components are shown in Figure 6.7.

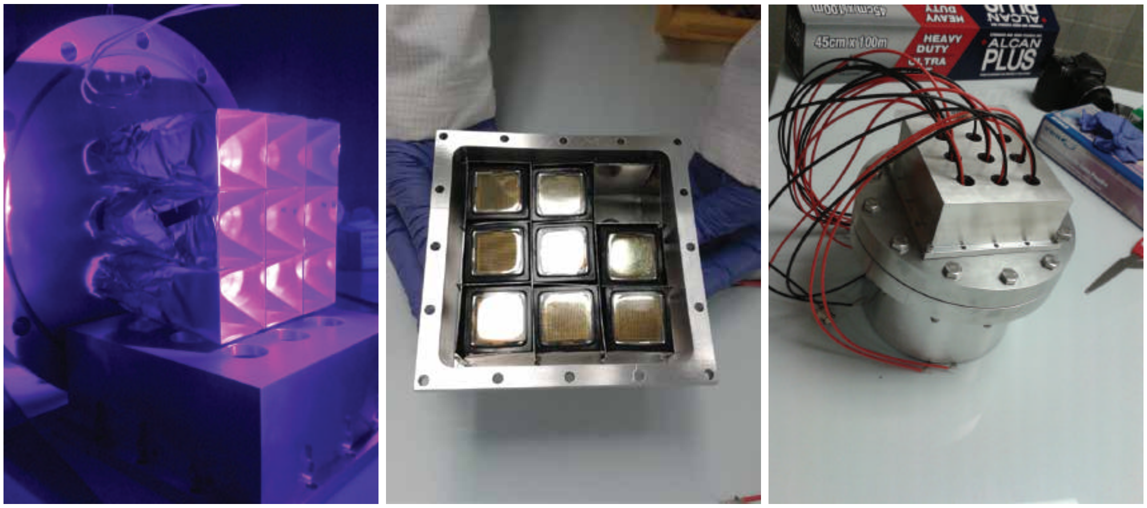

Figure 6.7: Above are photos of the signal components of the detector. On the left is a photo of all nine channels with the ^{6}Li glass glued to the light-guides under a blacklight. In the middle is a photo of eight out of nine PMTs in the dark box housing. On the right is the back of the assembled detector, showing the BNC cables coming from the PMTs in the dark box to read into the electronics.

6.3.2 Housing components

The detector volume was enclosed in an Al housing with a flange opening to the glass face. The rim of the flange was coated with 1 μm of natural abundance Ni to reduce UCN loss on the flange. This flange was connected to the UCN guide. The inside volume contains the glass and the light-guides placed under vacuum and in light-tight conditions. The light-guides led out of this volume into the PMT housing dark box, which is in air; each channel is magnetically shielded using μ metal. This housing also requires a light-tight environment for the PMTs.

Chapter 7

Electronics

7.1 Components of the DAQ system

The data acquisition system (DAQ) processes data in three steps while collecting data in real time. First, the detector, which is comprised of 9 signal channels, sends the raw data to the CAEN v1720 digitizer. After the digitizer processes the signals, the event data is then sent to the computer. The computer then saves the data as MIDAS events for later analysis. The next section goes into detail about how the raw data is processed by the digitizer and saved.

7.2 Software analysis method

7.2.1 Pulse shape discrimination

CAEN offers a licensed digital pulse processing (DPP) firmware for the 1720 digitizer. This DPP does some basic analysis of the incoming pulse within the digitizer. The digitizer may then accept or reject the signal and send the accepted signals to the computer. This reduces the computing load on the computer and speeds up the readout.

The DPP uses various signals to determine the position of the pulse in time and the pulse's shape, as shown in Figure 7.2. The relevant signals are as follows:

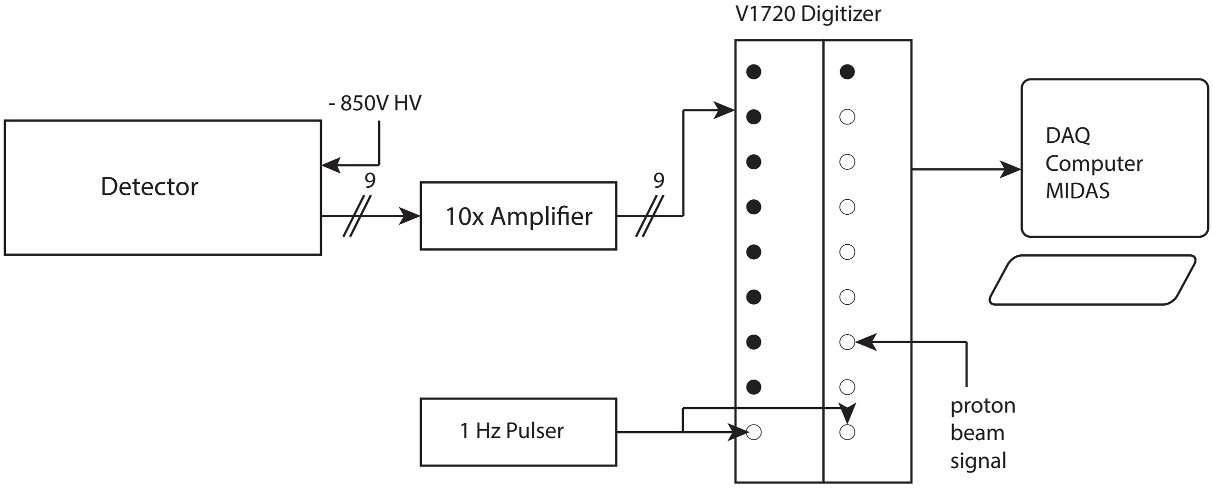

Figure 7.1: The three stages of data processing while taking data.

- Baseline: Also known as pedestal, baseline is the reference voltage level from which to decide if there should be a trigger.
- Threshold: The minimum difference between the signal and Baseline, with the signal below the Baseline, required to issue a trigger signal.
- Trigger: Time at which the signal crosses threshold for the beginning of an event
- Long/Short Gates: Gate values, in units of time, used to integrate charge over the signal. The long gate determines the total energy of the event and the short gate is a measure of the prompt charge deposited.

These values are then sent to the computer for further analysis.

Measuring the amount of charge in the tail of an event can be determined by comparing the long and short charge values:

$$PSD = \frac{Q_L - Q_S}{Q_L}, \tag{7.1}$$

where Q_L and Q_S are the charge values collected in the long and short gates in ADC, respectively. PSD stands for pulse shape discrimination. The closer the PSD is to 1, the more charge there is

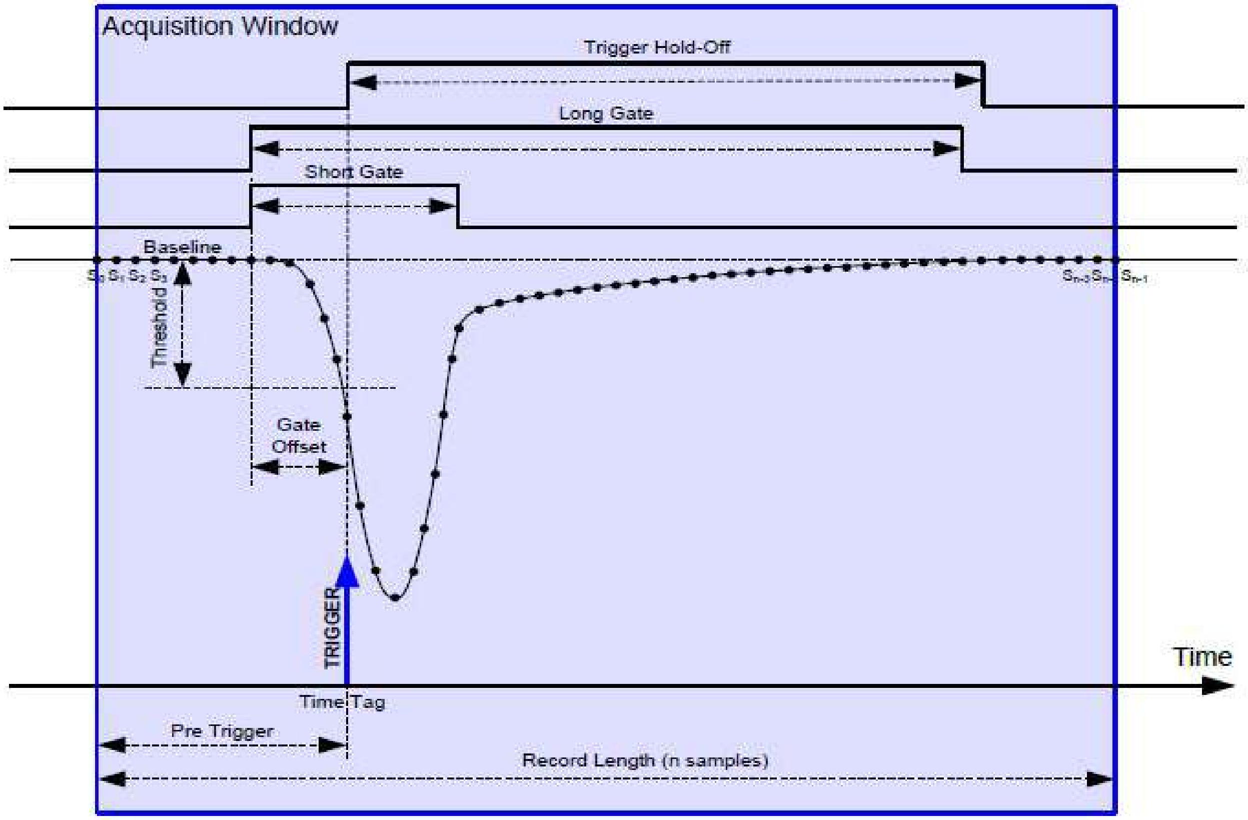

Figure 7.2: Graphic showing the positions of the gates signals relative to the pulse in position of time. The long and short gates open to collect charge for respective set times. Used with permission of CAEN [85].

in the tail of the event. Comparing the Q_L and PSD values was shown to be the most beneficial for separating signal from background events.

The firmware has an option for a variable baseline value. This baseline is calculated by averaging a number of previous samples. When the trigger signal occurs, the baseline value freezes and the frozen baseline value is used to compute the charge of the signal. The benefit of this is that the baseline value does not need to be set manually from background runs prior to data taking. However, this is successful only if the baseline is frozen sufficiently before the beginning of the pulse.

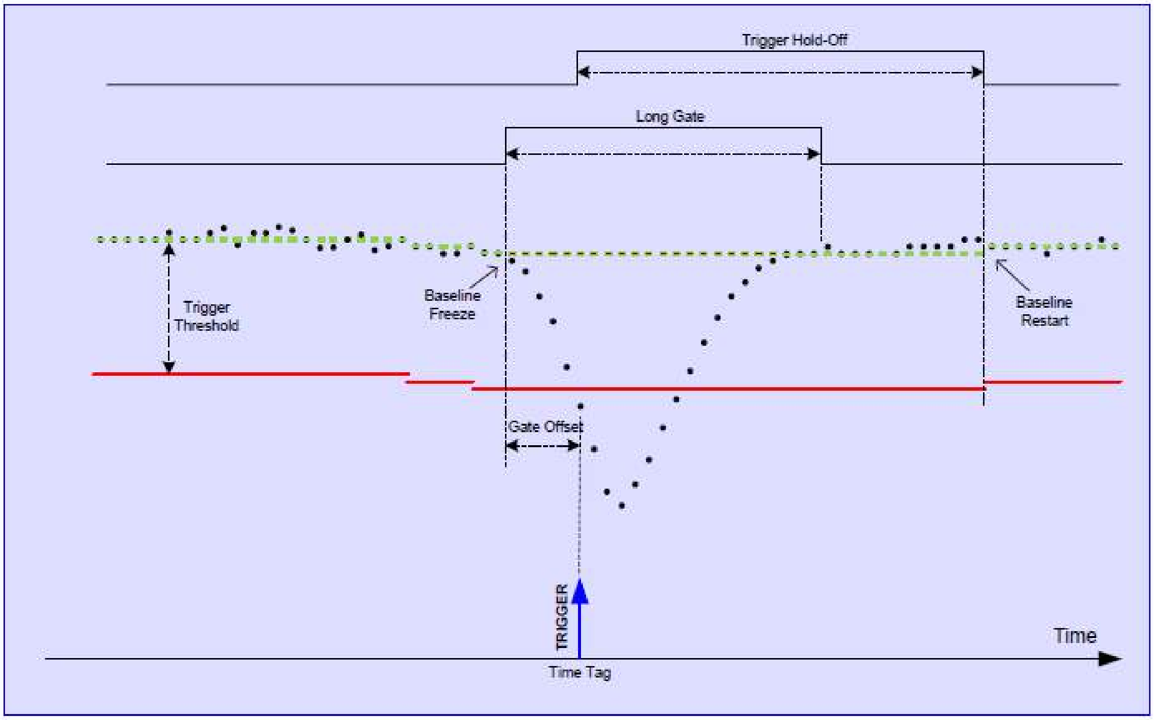

Figure 7.3: Graphic showing behavior of the baseline value when set to averaging. Used with permission of CAEN [85].

7.2.2 MIDAS

MIDAS, or Maximum Integrated Data Acquisition System, is a software package originally developed at PSI and TRIUMF. MIDAS consists of a web interface to an online database of equipment settings and readblocks. The software comes with a number of frontend programs useful for accessing CAEN modules, including digitizers. A frontend program written for the DEAP experiment was modified to read in the DPP data from the firmware. That data was then saved to file in MIDAS data banks. Again, this was to maximize read-in rate.

Later, after data taking, the .mid files were then reprocessed into ROOT files for further analysis [86].

7.3 Digitizer settings for data taking

The digitizer settings for data taking were developed with either an α source, or a thermal neutron source and a single channel set-up in a dark box. The signal settings are as follows:

- Baseline: variable
- Threshold: 200 ADC (approximately 100 mV)
- Trigger: self-trigger for each channel
- Long Gate: 200 ns (50 time bins)
- Short Gate: 40 ns (8 time bins)

  The long gate (Q_L) was mostly set at 200 ns. However, some runs were taken with the Q_L gate set at 400 ns or 800 ns to check for pile-up event effects.

Chapter 8

Tests of the UCN detector at PSI

8.1 Measurement at PSI

In August of 2015, the prototype detector was brought to the Paul Scherrer Institute (PSI) in Switzerland for a characterizing measurement.

8.1.1 UCN source

PSI has a UCN source with two beamline ports available for visiting scientists. The UCN source had 300 s cycles. The start of the cycle was produced by a pilot pulse of protons hitting the target to gauge the beam position. Ten seconds later, the full proton beam hit the target for 2 s, producing the neutrons which are then cooled to UCN levels and sent down the beamline [43]. Near the end of the 300s cycle, any remaining UCN are drained from the beamline. This cycle will be referred to as a UCN cycle.

There were two UCN ports available: West-1 and West-2.

West-1 was a horizontal connection with UCN having a minimum energy of 54 neV and a higher rate. The aperture of the beamport was 180 mm while the detector's face was 75 mm. A photo of West-1 is shown in Figure 8.2. West-2 was a vertical connection that had a minimum UCN dropping height of 120 cm before reaching any detector. West-2 offered the option of increasing the

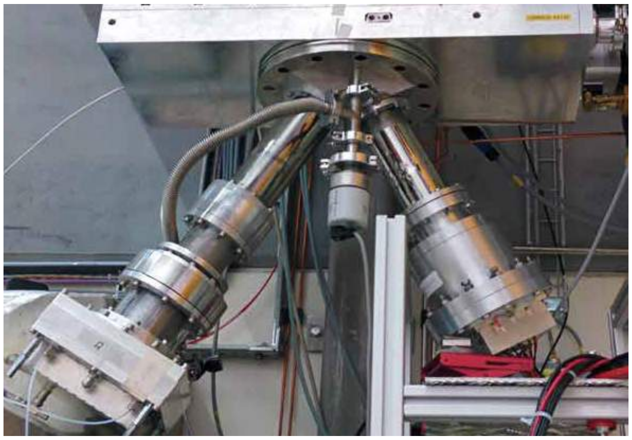

Figure 8.1: Photo of the UCN beam with the Y configuration on West-2. The UCN beam falls vertically down the pipe to the beam splitter, which splits the beam evenly between the two pipes. The PSI Cascade detector is to the left and the ^{6}Li UCN detector is to the right [87].

dropping height by adding longer guides between the UCN port and the detector, however, it had a lower rate than West-1. West-2 also had a y-connection attachment available for splitting the UCN between two detectors, as shown in the photo in Figure 8.1. Since the glass face of the detector had a Fermi potential of 103.4 neV, any UCN with lower energy cannot penetrate the detector face, such as in West-1. West-2, with its additional dropping height, had a higher minimum energy of about 120 neV. As a result, approximately 32% of UCN were not detectable on West-1, according to previous PSI measurements [87], while all the UCN were detectable on West-2. The rate of UCN detected on West-1 had roughly a factor of 10 higher rate than West-2, over the course of a UCN cycle, as shown in Figure 8.3.

8.1.2 Cascade detector

PSI also had a commercial Cascade detector available for comparison. This was a GEM-based detector with its own readout system. This type of detector is discussed in Section 5.2. A photo of the Cascade detector is shown on the left of the y-connection in Figure 8.1 along with the ^{6}Li detector on the right.

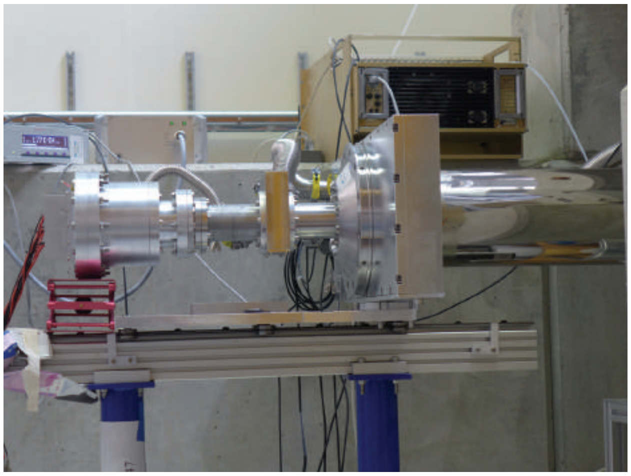

Figure 8.2: Photo of the UCN beam connected to the West-1 beamport. West-1 offered a higher rate of UCN per UCN cycle to test for rate dependence in a horizontal configuration [87].

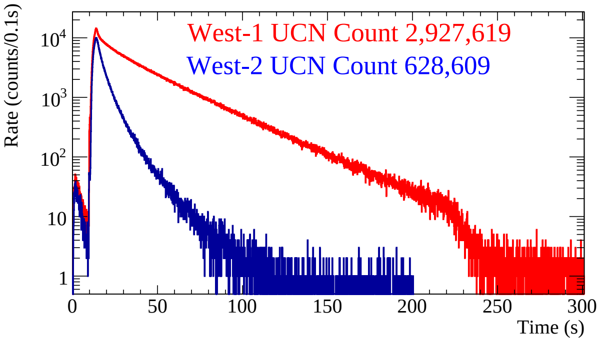

Figure 8.3: UCN count over the cycle of generating UCN beam for the West-1 and West-2 configurations. West-1 has a higher count. Near the end of the cycle, the remaining UCN in the pipes are drained from the beamline, which results in a noticeable drop in rate in the West-1 count [87].

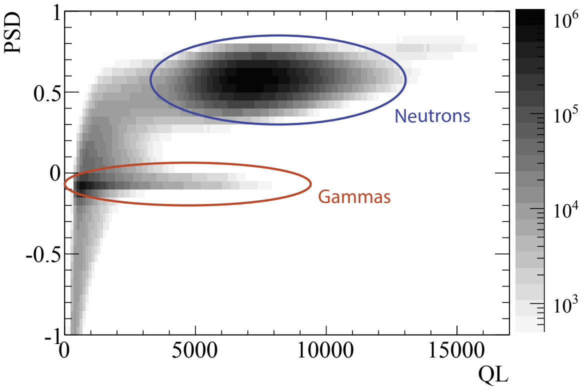

Figure 8.4: Event spectra from the PSI UCN beamline using the ^{6}Li detector and the digitizer firmware. The main concentration of events are UCN events, while the line near $PSD = 0$ are background events.

8.2 Raw data

It was previously found that comparing the Q_L and PSD values of the data output were the most useful for separating signal and background. A 2D histogram of PSD versus Q_L of some representative data is shown in Figure 8.4. The UCN events are at about 0.5 PSD and between 5000 and 12,000 for Q_L. The background has a PSD of about 0 with the other remaining events due to pile-up effects, dead-time events, and late light. A small amount of double events (2 or more UCN events captured in the Q_L window) can be noted at a Q_L of about 14,000 and a PSD of about 0.8.

Since there are nine channels, each channel's Q_L spectrum was compared with and without PSD cuts as shown in Figure 8.5. Since the UCN beam is not evenly distributed across all channels, this comparison can show any additional effects of a PSD cut relative to rate. A PSD cut of > 0.3 removes most of the background data regardless of signal rate.

In order to better determine background contamination, late-light, and deadtime effects, a simulation was developed to understand the detector response.

8.3 Relative efficiency to Cascade detector

Using the $Q_L > 3000$ and $PSD > 0.3$ cuts from Section 9.2 the rate of detecting neutrons can be compared to the Cascade detector. This comparison was done by using the y-configuration connected to the West-2 UCN port as shown in Figure 8.1. First, the total number of UCN found per UCN cycle was calculated for both the ^{6}Li detector and Cascade detector. Since the Cascade detector required two additional adapter flanges to bring the aperture from 110 mm to 70 mm for the y-configuration, the UCN beam had an additional approximately 20 cm more distance to the Cascade detector than the ^{6}Li detector and a smaller detector area exposed to UCN. The ^{6}Li detector required one adapter flange to go from 110 mm to 75 mm. The Cascade detector had a lower Fermi potential and the additional drop adds more energy to the incoming UCN for that detector. The difference in detector area was roughly accounted for by reducing the number of UCN detected by the ^{6}Li detector according to the fractional difference in detection area between

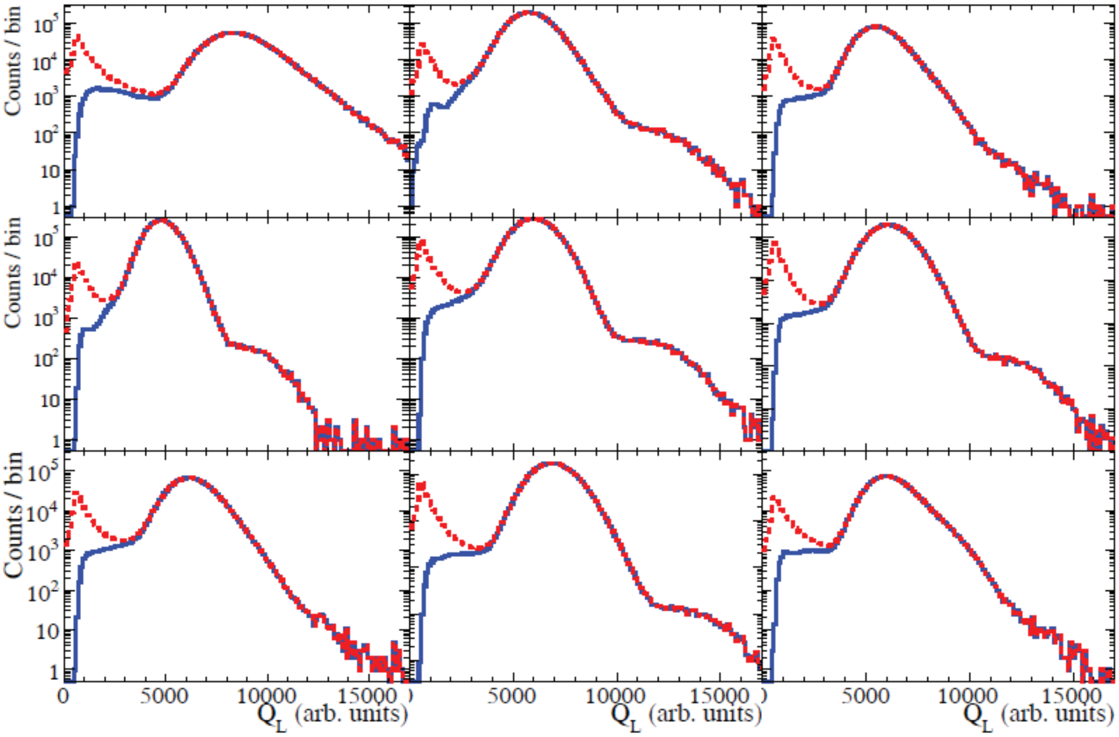

Figure 8.5: The effect of applying a PSD cut for each of the detector channels. Each channel behaves slightly differently due to the differing rates (e.g. the middle channel always has the highest rate). However, the PSD cut largely affects background only, regardless of channel. Red is the spectra with no PSD cut, and blue is the spectra with PSD>0.3 [87].

both detectors or (70 mm/75 mm)^2 $= 0.871$. Figure 8.6 shows the UCN cycle totals for both detectors and the detection area correction. This shows 10.28 ± 0.02(stat)% increase in detected UCN in the ^{6}Li detector [87]. During the course of the run, the number of UCN available in the beam varied and both detectors noticed this variation.

The same data was then used to calculate the averaged UCN per cycle for both detectors (with the detection area correction for the ^{6}Li detector), as shown in Figure 8.7. Here the ^{6}Li detector counted more UCN at the beginning of the cycle, but then less towards the end of the UCN cycle.

This difference could be due to the relationship of the initial UCN spectrum and the configurations of the two detectors, including their respective Fermi potential at the surface of the detector. Faster UCN reached the detector face first, which makes for a higher rate of penetration for the ^{6}Li detector, since that detector had a higher Fermi potential. Towards the end of the UCN cycle, however, the slower neutrons reached the detectors' surface and had a lower rate of penetration, especially for the ^{6}Li detector. A GEANT4 simulation was developed to determine how this additional drop and flange would affect the rate of UCN reaching each detector. This rate was found to be strongly dependent on the initial UCN spectrum [87].

8.4 Other efficiencies

The effective area of the detector face was determined from a photograph of the detector face shown in Figure 8.8. Since the length of the ^{6}Li glass was 29.0 ± 0.1 mm, this length was used for scaling of pixels. The number of pixels within the detector aperture was counted as the denominator, and the number of pixels of glass were counted as the numerator. Using this calculation, the effective area was estimated to be $97.4 \pm 0.1\%$ [87].

The efficiency of the transmission of UCN through the ^{6}Li-depleted layer glass was found by the LPC Caen group [88]. The closest measurement to our 60 μm ^{6}Li-depleted layer was the 55 μm measurement of $92.6^{+1.2}_{-1.8}\%$ transmission.

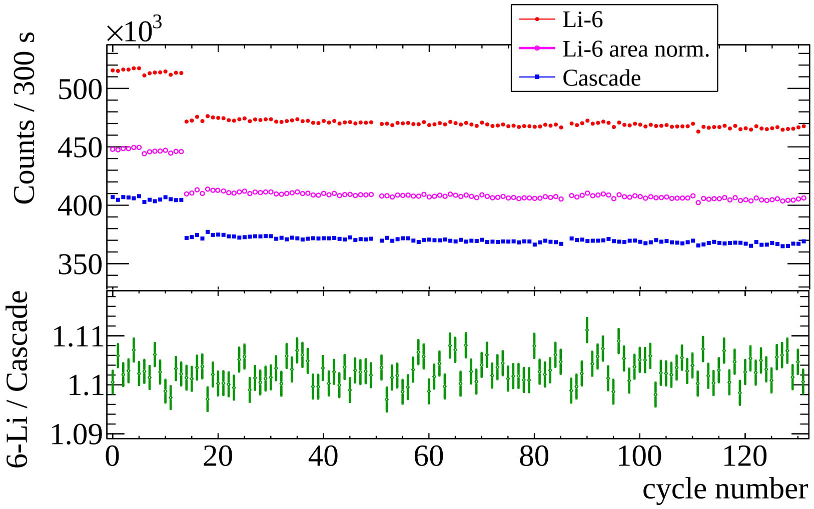

Figure 8.6: The top graph shows the total number of neutrons detected per UCN cycle for both the ^{6}Li detector and the Cascade detector. Since the cross-section of the detectors' face is not the same, a scaling factor of the ^{6}Li area to the Cascade area is also shown (pink). The bottom graph shows the ratio of the total neutron count from the adjusted ^{6}Li detector area and the Cascade data. The ^{6}Li detector detected about 10% more neutrons than the Cascade detector over the course of the total cycle. This assumes that the UCN beam is evenly split between the detectors.

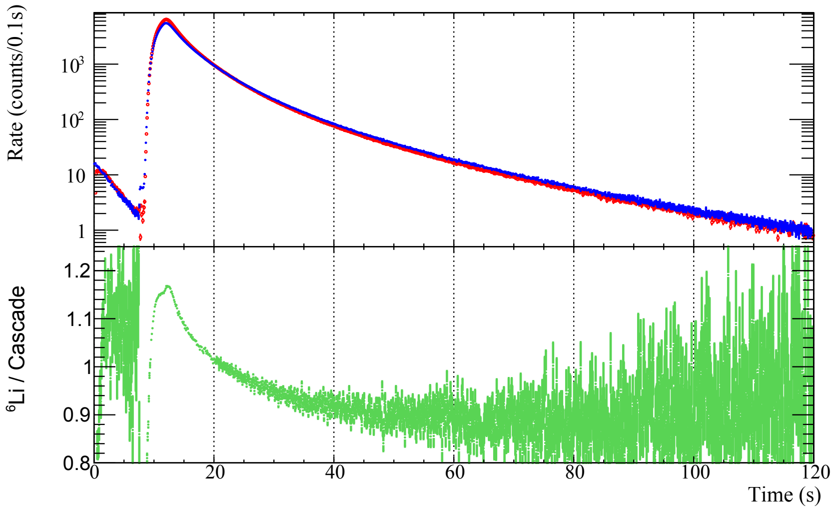

Figure 8.7: The top graph shows the average rate of detected neutrons over the course of 130 UCN cycles for both detectors. Red is the ^{6}Li detector and blue is the Cascade detector. The bottom graph is the ratio of the rates between the detectors. The ^{6}Li detector detects about 10% more neutrons at the beginning of the cycle and then about 10% fewer neutrons at the end of the cycle compared to the Cascade detector.

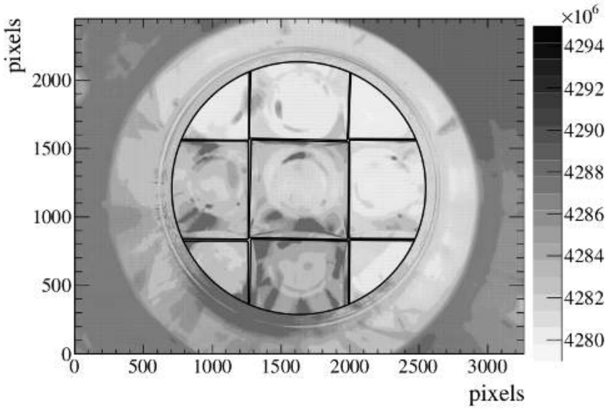

Figure 8.8: To find the effective area of the detector face, a photo was used to compute the area of the face covered by glass as opposed to the space between channels.

8.5 Calculated efficiency for ^{6}Li detector

Combining all of the efficiencies of the glass, effective area, and the background rejection, the total efficiency is estimated to be $89.7^{+1.3}_{-1.9}\%$. The uncertainty was dominated by the uncertainty of absorption in the ^{6}Li-depleted layer. The ^{6}Li detector was determined to be at least as efficient as the Cascade detector.

Chapter 9

Simulation and fit results of the ^{6}Li

9.1 Signal and digitizer simulation

The simulation used for determining different signals had two steps. First, a signal with added noise was simulated. Second, this simulated signal was fed into a simulated DPP-PSD data analysis.

The simulated signal uses a single photo-electron (pe) from the detector as having a Gaussian signal shape with a width of $\sigma_{pe} = 6.4$ ns, and an amplitude of $A = 20$ mV but with a minimum amplitude of 4 mV. A scintillation signal was then built by summing the arrival times of the pe's (mean of 83 pe's) in a Poisson distribution with a rise time of τ_R =6.4 ns and a fall time of $\tau_F = 41.7$ ns and an additional slow fall time of $\tau_S = 2000$ ns. The probability, $P(t)$, of a pe occurring in time, t, relative to the start time of the signal, T, is shown below:

$$P(t) = \begin{cases} A(1 - e^{-(t-T)/\tau_R}) & T < t < T + 5\tau_R \\ A((1 - f_L)e^{-(t-T-5\tau_R)/\tau_F} + f_L e^{-(t-T-5\tau_R)/\tau_S}) & t \geq T + 5\tau_R \end{cases}, \tag{9.1}$$

where f_L is the fraction of late light. The probability function and the resultant simulation neutron scintillation signal are shown in the left panel of Figure 9.1. The background signal was also simulated in this way, but with an exponential distribution with a mean of 7.5 pe's. These values

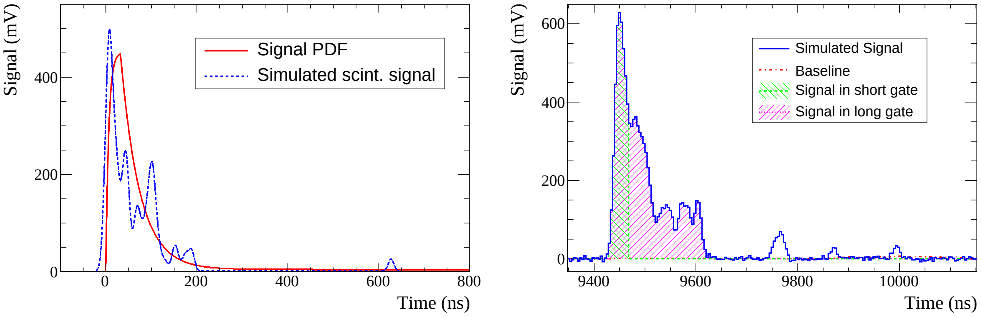

Figure 9.1: A simulation was developed in order to determine how to categorize different data events. (left) The signal was generated with sufficient tail (red) and noise (blue). (right) The simulated signal was then processed by simulating the gate charge collection method used by the firmware.

were all estimated by comparing and adjusting the simulated signal to match the output of the detector. The signals were then assembled at randomized rates of 10 kHz neutrons and γs each for 0.1 s length of total signal.

Next the simulated signal was fed into a simulated DPP-PSD digitizer. All the simulated gates were giving the same settings as the physical digitizer given in Section 7.3. Visually, the simulated digitizer analyzed a positive signal, while the physical digitizer had a negative signal. The signal was analyzed by the simulated digitizer and produces the gate values as seen in the physical data. The simulated digitizer was set to only trigger if the signal crossed the set threshold relative to the baseline value the same as the digitizer.

Different event signals were simulated and compared to data for analysis:

- Single neutron: One neutron signal was captured in the Q_L window.
- Multiple neutrons: Two or more neutron signals were captured in the same Q_L window.

Example pulses of these signal events are shown in Figure 9.2.

As far as background signals, one source was from the γ events in the light-guides. The scintillator material also has a slower decaying light component of up to 2 μs [87]. That was a very slow signal and was simulated as a late light contamination. The different background signals that were found are listed below:

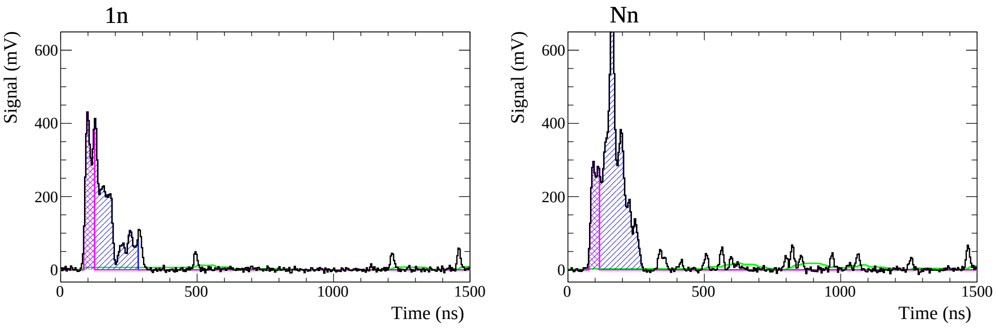

Figure 9.2: Sample simulated signal events. The left one represents a single signal and the right one represents multiple signals with the Q_L gate. The pink, left-slanting area is the integrated charge for the short gate, the blue, right-slanting area is the integrated charge for the long gate, and the green line with no area fill is the baseline value.

- Single background: One γ pulse captured in the Q_L window.
- Multiple background: Two or more γ pulses captured in the Q_L window.
- Late light: Coincident pe's from late scintillation light of a neutron capture.

Example pulses of these background events are shown in Figure 9.3.

The detector continued to collect data even when there was no UCN cycle. For some UCN cycles, the gate value between the UCN source and the experimental area was left closed. For these cycles, a data derived background was collected. When compared to the single γ simulation in Q_L in Figure 9.4, one can see good agreement at lower energies, showing that most of the background data was single γ events. The higher remaining background events were likely multiple events or light leaks.

After comparing the background and neutron capture signals, two other types of signals became apparent. For one, there was a possibility of background events mixing with neutron events, such as one neutron and one γ event both captured in Q_L. Another type of event was also found by comparing the time between two signals. It was found that the second event always occurred a minimum of 150 ns after the end of the first event, in order to be read. Figure 9.5 shows the minimum distance between events in time, which represents a readout dead-time. The Q_L is set to 200 ns and the closest the next event could be read was 150 ns after that. This could result in part

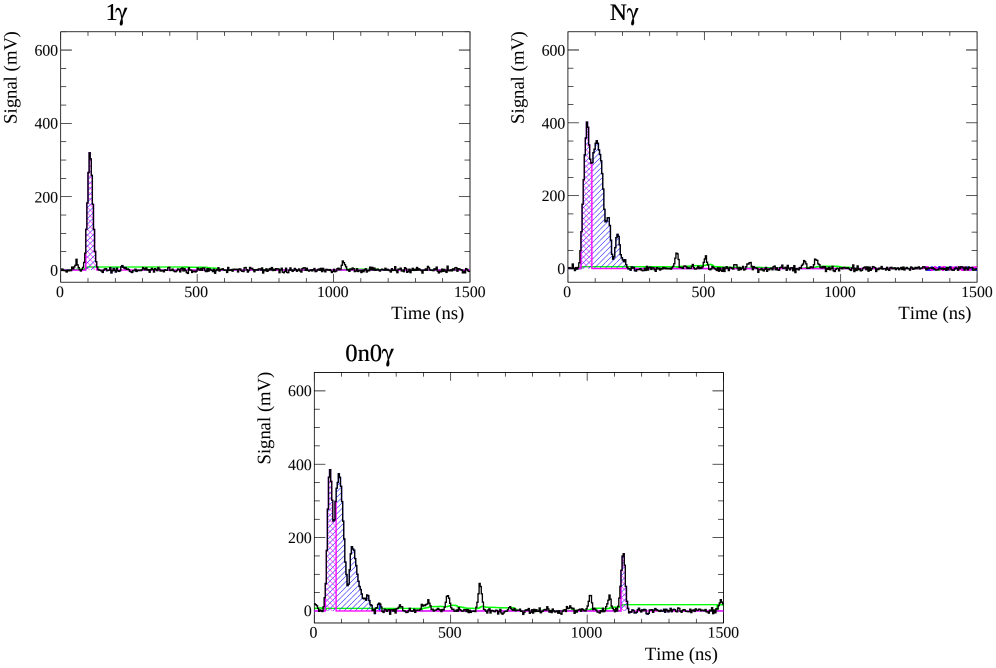

Figure 9.3: Various types of background events were simulated. Upper left graph is a single background event. Upper right graph is multiple gamma events within the Q_L gate. Lower is a late light event, a trigger that occurs with the signal late light. The pink, left-slanting area is the integrated charge for the short gate, the blue, right-slanting area is the integrated charge for the long gate, and green line with no area fill is the baseline value.

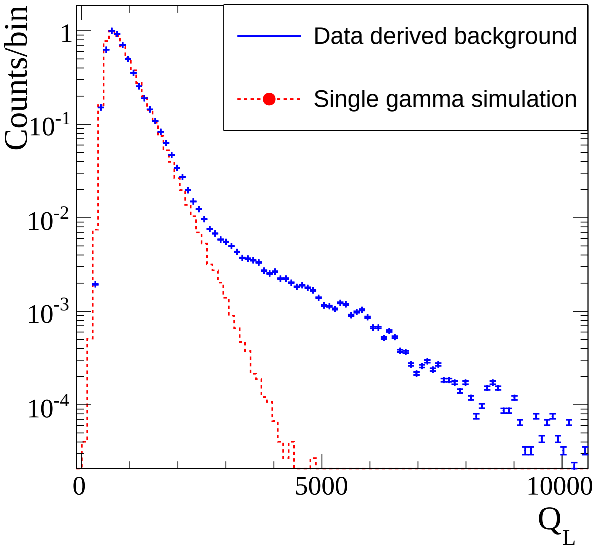

Figure 9.4: Comparison of the single background spectra (red) and the background data collected during runtime in Q_L. Most of the background events shown are single background events.

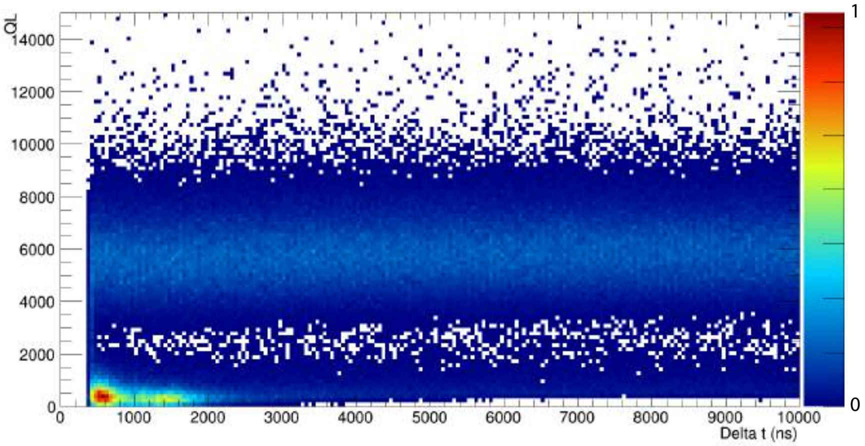

Figure 9.5: Evidence of retrigger events in δt after first event. Data events are histogrammed in Q_L to the distance in time between two successive signals, δt. There is a gap in δt of 350 ns after the first event and a concentration of small events (small in Q_L) immediately after. These are retrigger events. Later events are late light events.

of the second neutron signal being missed by Q_L and is referred to as a deadtime event. When the Q_L was widened to 400 ns or 800 ns, the deadtime effect became more pronounced. These other signals are as follows:

- One neutron and one γ: Q_L was triggered by one γ or neutron and captures part of a neutron event or a neutron event with additional charge from a γ event.
- Deadtime event: One neutron event was partially captured in Q_L due to electronic deadtime.

Examples of other signals are shown in Figure 9.7.

9.2 Fitting simulation to data

The digitizer output of all of these simulated signals were then sorted into histograms of Q_L vs PSD. The histograms of the signal events are in Figure 9.8, the histograms of the background events are in Figure 9.9, and the histograms of the remaining other types of events are in Figure 9.10.

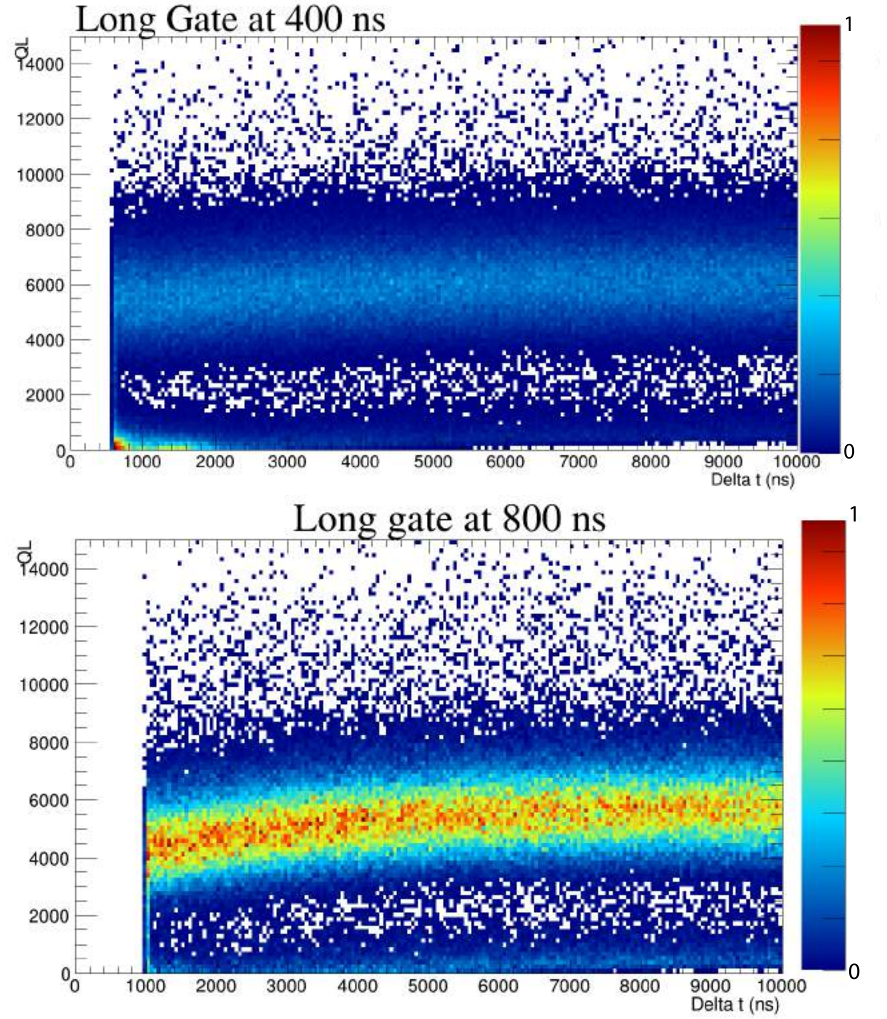

Figure 9.6: Stronger evidence of deadtime in the electronics. The Q_L gate was widened to 400 ns in the top figure and 800 ns in the lower figure. More energy loss is apparent in the second event. Left represents a single signal and right represents multiple signals with the Q_L gate.

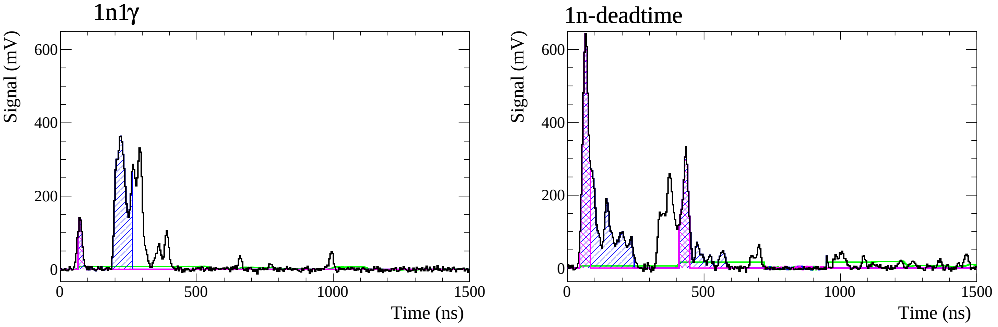

Figure 9.7: Sample simulated other events. Left is a mixed event with one signal and one background event within the Q_L gate. Right is a dead event. The first pulse is a signal event, but the trigger remains closed during the beginning of the second event. The pink, left-slanting area is the integrated charge for the short gate, the blue, right-slanting area is the integrated charge for the long gate, and the green line with no area fill is the baseline value.

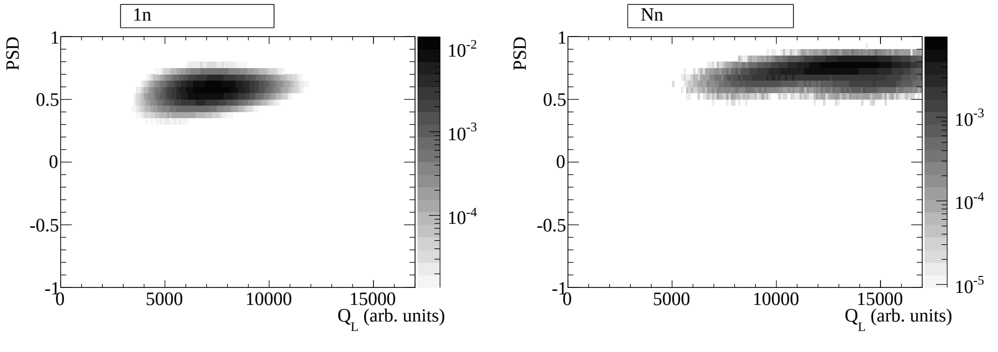

Figure 9.8: Simulated signal spectra in Q_L and PSD. Left is the spectra for single signal events and right is the spectra for multiple signal events.

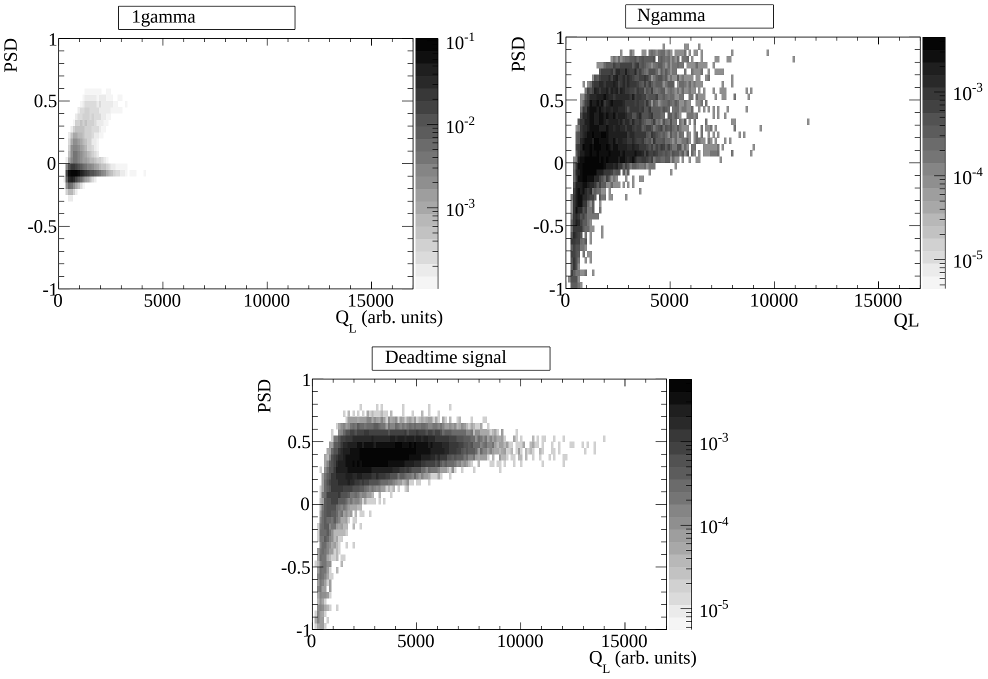

Figure 9.9: Simulated background spectra in Q_L and PSD. Upper left is the spectra for single background events. Upper right is the spectra for multiple background events. Bottom is the spectra for late light events.

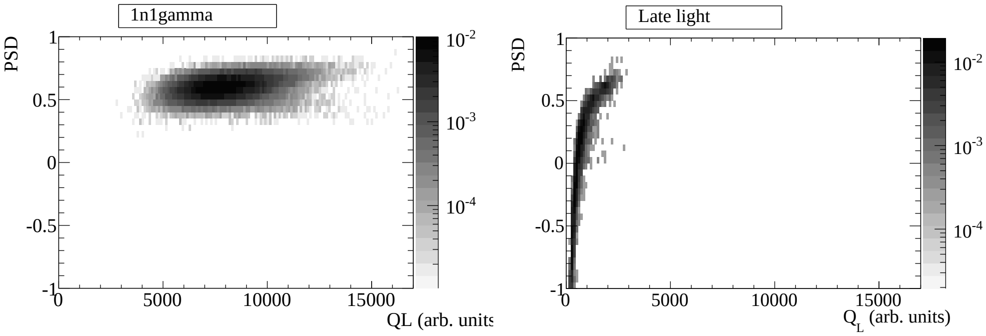

Figure 9.10: Simulated mixed event spectra in Q_L and PSD. Left is the event spectrum for one signal and one background event within the Q_L gate, and right is the spectrum for dead time events.

Each of these histograms derived from simulation was then converted to a probability distribution function (PDF) template, where the data is a function of PSD and Q_L in the form of $P_i(PSD, Q_L)$, where i =(1n, Nn, 1γ, Nγ, 1n1γ, 1n dead-time, 0n0γ). The PDF templates were fit to the data by using an extended maximum likelihood fit. This involved estimating each P_i by N_i minimized a negative log likelihood as calculated as a sum over all M of PSD^j and Q_L^j of the data as

$$-\ln(L) = \sum_i^7 N_i - \sum_j^M \ln \sum_i^7 P_i(PSD^j, Q_L^j). \tag{9.2}$$

Figure 9.11 shows the fit to data projected along the Q_L and PSD axes.

The neutron efficiency and background contamination were calculated for a range of cuts, predominately along Q_L. The neutron efficiency was calculated by finding the number of neutron events that passed the specified minimum cut, N_n^{cut}, over the total number of neutrons in the template:

$$\epsilon_n = \frac{N_n^{cut}}{N_n}, \tag{9.3}$$

where ϵ_n is the calculated efficiency. The background contamination was calculated by finding the number of background events passing the specified minimum cut, N_γ^{cut}, over the total number of neutrons in the template:

$$\eta_\gamma = \frac{N_\gamma^{cut}}{N_n}, \tag{9.4}$$

where η_γ is the calculated background contamination. Figure 9.12 shows the neutron efficiency and background contamination for a range of cuts.

Since the rate of UCN entering the detector varies according to time from the beginning of the UCN cycle, the data was also separated into three time periods to determine any changes in rate effects to the efficiency. The first period was 0 to 10 s after the proton beam arrived, which had an event rate of 100 to 50 kHz. The second period was 10 to 40s after the proton beam arrived, which had an event rate of 50 to 20 kHz. The last period was 40 to 270 s after the proton beam arrived,

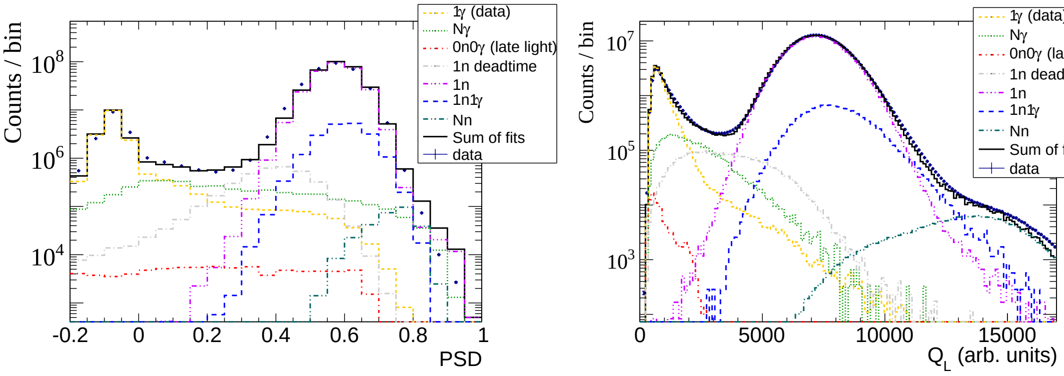

Figure 9.11: Results of fitting the simulation to data. The background data spectra plus the multiple background, late light, and various signal simulation spectra were fitted to data. The results are shown in projections along the PSD axis (left) and the Q_L axis (right).

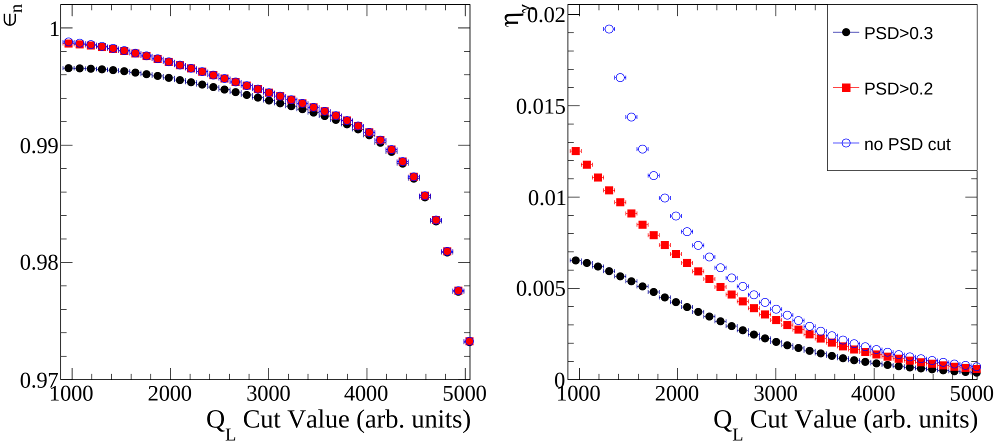

Figure 9.12: Using the simulation fits, the detector efficiency (left) and the background contamination (right) were calculated using increasing Q_L and PSD cuts.

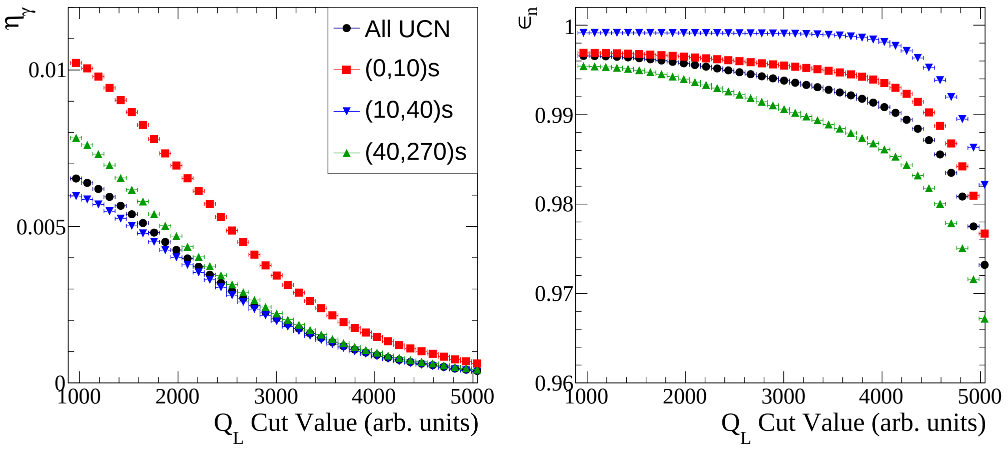

Figure 9.13: The same detector efficiency and background contamination plots as Figure 9.12, but with the UCN cycle separated into three different rates. The first 10 s of the UCN cycle has the highest rate and 40 to 270 s have the lowest rate. The left shows the efficiency and the right shows the background contamination.

which had an event rate of 20 to 0.1 kHz. Applying the efficiency and background contamination calculations to the different periods over different Q_L cuts (with $PSD < 0.3$) is shown in Figure 9.13.

The high rate period showed the most contamination due to the larger rate of pile-up events. While these double events were counted as single events here, double event can be separated from the single signal data and counted as two events instead of one. The low rate period showed the next highest contamination, due to the higher ratio of background to neutrons present in the data. Assuming a cut of $Q_L > 3000$ and $PSD > 0.3$ the neutron efficiency was estimated as $99.5 \pm 0.5\%$, and the background contamination was estimated as $0.3 \pm 0.1\%$. Due to the different signal shapes, the ^{6}Li detector has good background rejection. This difference is likely due to two effects. The first is that backgrounds from interactions in the light-guides make fast signals, and γ events in the scintillation glass deposit very little charge due to the thin layer.

9.3 Recommendations for improved detector performance

Throughout the process of characterizing the prototype detector, some areas of potential improvements were discussed for the final detector design for the TRIUMF nEDM experiment. A number of these areas are discussed below:

- Improved method to hold lightguides: Since the lightguides go from inside vacuum to outside vacuum, the lightguides are held in place by o-rings and a plate. Despite the connecting plate, the lightguides would occasionally come loose and break vacuum. Therefore, a more stable form of holding the lightguides in place needs to be developed.
- Limit rate of pumping down detector: This suggestion occurred after a rapid vacuum test where one of the optically-bonded pieces of glass came unbonded. The channel was repaired by gluing another piece of optically-bonded ^{6}Li glass, but the force of a rapidly pumping down of the volume to vacuum can damage the glass bonding.
- Improved dark box for PMTs: Light-tightness was an issue in reducing background signal. The detector had to be thoroughly wrapped in black blankets to reduce any exposure to light to the PMTs and flooding the output. The next housing to be built around the detector needs to include light-tightness.
- Cable robustness: Some of the channels appeared to pick up electrical noise due to the imperfect connection of the handmade BNC connections. New cables need to be tested for robustness.
- Reduce the amount of Al on flanges: A large amount of material near the detector can introduce more background as high energy neutrons and gamma rays may interact in the material around the detector producing electrons, positrons and gamma rays, which leave a signal in the detector or light guides. Al can also affect the incoming UCN beam. Reducing the exposure of the UCN to Al in the flanges can reduce this source of UCN loss. A number

of materials may be investigated, such as Be or PEEK flanges, as these materials have a lower Z than Al.

Part III

Thermal neutron measurement at TRIUMF

Chapter 10

Method of measuring thermal neutron flux using Au foils

10.1 Method from Paul Scherrer Institute

The Paul Scherrer Institute in Villigen, Switzerland, has a high-intensity UCN source currently in operation [89, 35, 90, 43, 44]. The thermal neutron flux produced by the source was measured using activation foils with the results published in 2014 [44]. The purpose of this experiment was to test models of thermal neutrons produced by the source the thermal neutron flux could be measured from 1 m away from the source [91].

To measure the thermal neutron flux at points away from the PSI source, an activation technique utilizing Au foils was developed. Au was used for its high thermal neutron capture (98.6 bn):

$$^{197}\mathrm{Au} + n \rightarrow {}^{198}\mathrm{Au} \rightarrow {}^{198}\mathrm{Hg} + \gamma + e^{-}. \tag{10.1}$$

The half-life of ^{198}Au is 2.6947(3) days with a main γ transition of 411.8 keV [92].

Au foils were wrapped around a rope which was then inserted into an access tube (see Figure 10.1). This allowed the foils to be placed at various distances from the target [44].

The activation results were then compared to Monte Carlo N-Particle eXtended (MCNPX)

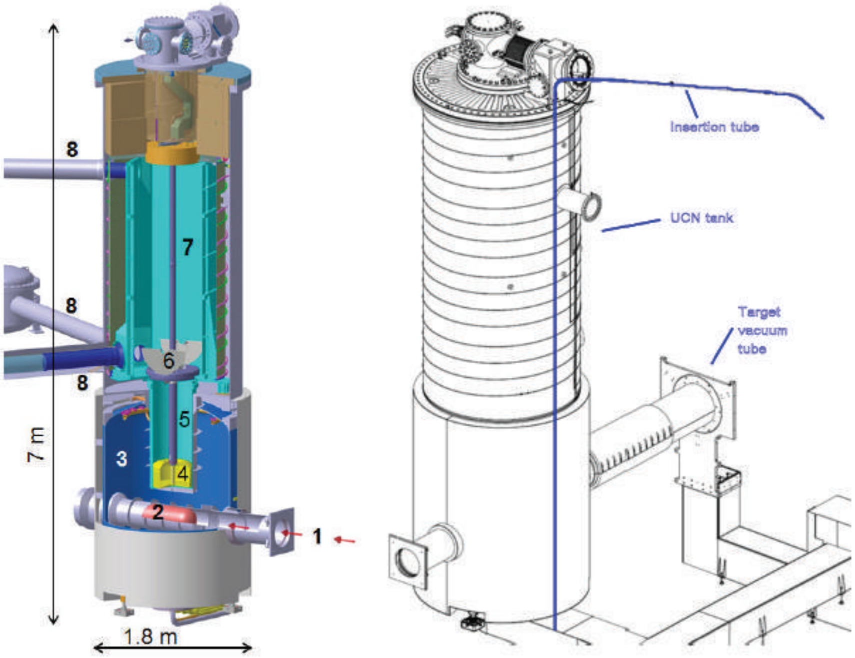

Figure 10.1: (left) Sketch of PSI UCN source where (1) is the proton beam, (2) is the spallation target, (3) is the heavy water moderator tank, (4) is the deuterium moderator vessel, (5) is the vertical UCN guide, (6) is the UCN storage vessel shutter, (7) is the UCN storage vessel, and (8) shows the available UCN guides to experiments. (right) Sketch of placement of Au foils in the PSI UCN source. The foils were placed along the rope which was then inserted into the top of the source [44].

simulations. The MCNPX simulations contained two versions: a full, detailed version of the source and surrounding materials, and a reduced geometry that removed some components of the UCN and D_2O tanks. The measured activity agreed well with the full simulation, but was between the full and reduced simulations at 50 cm above the beam. The simulations were within 10% at this position [44].

10.2 Practice measurement at TNF

The D2O cryostat for the horizontal ultracold neutron (UCN) source was commissioned in the winter of 2016. A thermal neutron measurement utilizing Au foils and Cd covers was developed as part of the commissioning process. In order to assess the accuracy of calculating the thermal neutron flux using these UCN foils, a practice measurement was done at the thermal neutron facility (TNF), where a thermal neutron beam was available. This practice measurement involved irradiating two of the UCN foils alongside two of the Au foils typically used at TNF. The activation of these foils were then analyzed and used to calculate the thermal neutron flux through the surface of the foils. After accounting for geometric effects, primarily the different foil thicknesses, the calculated fluence of neutrons through the UCN foils was found to be $2.2 \pm 0.1 \times 10^{10}$ n/cm^2, while the calculated fluence of the typical TNF foils was found to be $2.3 \pm 0.1 \times 10^{10}$ n/cm^2. Most of the uncertainty was due to the activation measurement counting statistics. Adjusting this gives agreement between the different foil geometries.

The TNF was located at the end of BL1A. The Au foils used at the UCN source were 1 cm$\times$2 cm$\times$100 μm while the TNF foils were 1 in diameter and 25 μm thick. An irradiation measurement was done on both UCN and TNF foils and then compared, in order to determine the thermal neutron flux calculated in both set-ups. By making this comparison, the UCN foils may then be used to determine the thermal neutron flux at the UCN source.

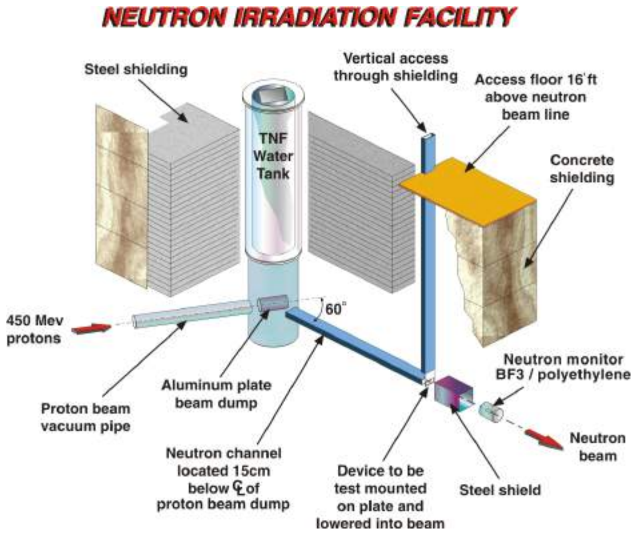

Figure 10.2: Diagram of the Thermal Neutron Facility. Protons enter the TNF water tank and stop in the Al plate. The resultant neutron beam is extracted through a channel out of the shielding. The neutron beam can be accessed (for irradiation purposes) through the vertical access [93].

10.3 Thermal Neutron Facility

Since the TNF was located at the end of BL1A, the facility had a steady thermal neutron flux available whenever BL1A has protons from the TRIUMF cyclotron.

The protons from BL1A pass through meson production targets and were then stopped in a water-cooled Al plate that acts as a beam dump. Neutrons were then extracted through a channel in the steel shielding around the beam dump [93], as shown in Figure 10.2.

The energy range of the neutrons went from thermal to 400 MeV neutrons with approximately 5×10^5 thermal neutrons /cm^2/s and 6×10^6 neutrons/cm^2/s above 1 MeV. Figure 10.3 show the neutron energy spectra, and Table 10.1 summarizes parameters of the neutron source. The flux was most uniform across a rectangular region 5×12 cm^2 of the beam and was noted on the board used in placing samples, as shown in Figure 10.5. In this area, the most change in the flux was in the vertical direction, which has a gradient decrease of 50% towards the top of the area [94].

The TNF housed a BF$_3$ detector for neutron calibration. Data was collected from both the BL1 proton beam current sensor and the BF$_3$ neutron detector. The BL1 sensor measured the proton beam current in μA from the cyclotron. However, only $50 - 65\%$ of the proton beam

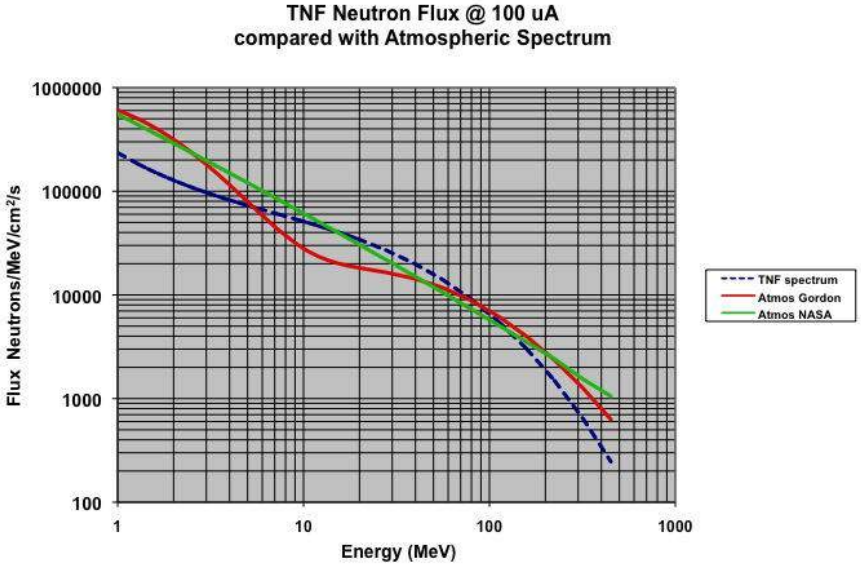

Figure 10.3: TNF neutron spectrum compared to atmospheric neutron flux [94]. The TNF flux is comparable to the neutron flux at high altitudes. As such, the facility is often used for determining the neutron flux resistance of electronics to be placed at these altitudes.

Table 10.1: Source specifications of the various neutron flux sources available at TRIUMF [94]. The measurement focuses on the TNF source.

	TNF neutrons	BL1B neutrons	BL2C neutrons
Energy	Thermal to 400 MeV	1/E spectrum to 480 MeV	1/E spectrum to 120 MeV
Flux (neutrons/cm^2/s)	2×10^6 to 3×10^6 above 10 MeV	10^3 to 5×10^5 above 10 MeV	10^3 to 5×10^4 above 10 MeV
Spot Size	5×12 cm^2	4 to 60 cm diameter	30 to 150 cm diameter
Spot Homogeneity	+/- 10%	+/- 10%	+/- 10%
Beam Counting and Monitoring System	BF$_3$ Counter and Activation Foils	BF$_3$ Counter and Activation Foils	BF$_3$ Counter and Activation Foils
Device-Positioning System	Movable Trolley with positive stop	Remote-controlled X-Y platform with laser alignment	Remote-controlled X-Y platform with laser alignment
Access Conditions	6 m cable length to Control Area	20 m cable length to Control Area	20 m cable length to Control Area

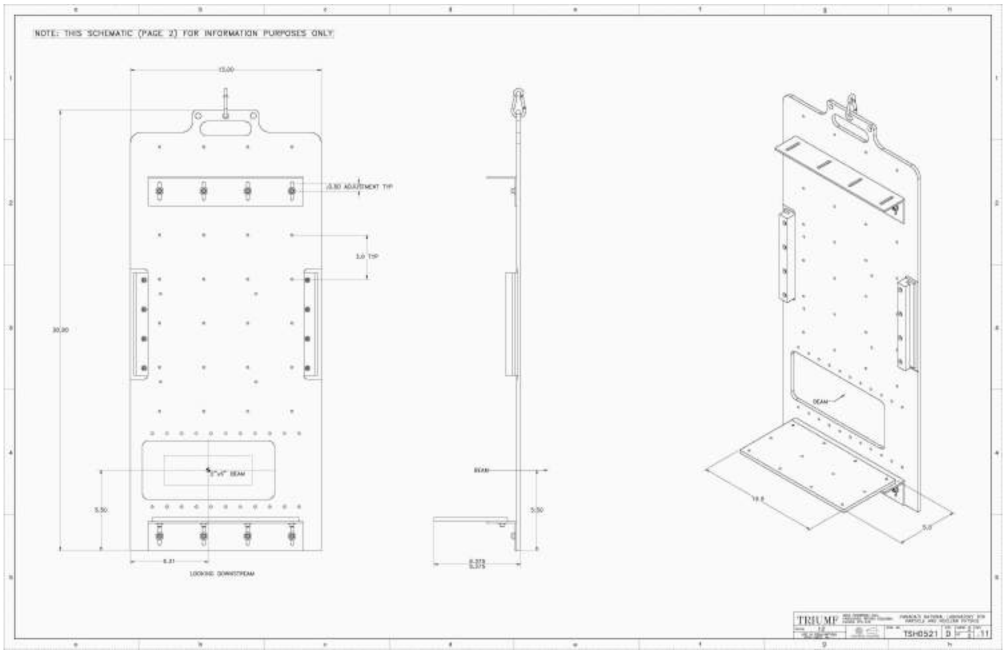

Figure 10.4: Sketch of irradiation plate.

reached the TNF, so the BF_3 neutron detector was placed near the TNF to measure a portion of the thermal neutron flux at the TNF. Beamline data was read via the xstrip program from the TRIUMF beamline control system [93].

10.4 Foil irradiation method

Four ^{197}Au samples were used for the irradiation test:

- 2 TNF circular foils, r = 1.27 cm, thickness = 0.00254 cm, previously irradiated
- 2 UCN rectangular foils, l = 2 cm, w = 1 cm, thickness = 0.01 cm, never irradiated before

One of the TNF foils and one of the UCN foils were also covered with 0.05 cm Cd foils. The Cd foils were encompassed with tape, so as to be safe enough to handle without gloves. The samples were then placed in individual bags and taped to the TNF plate. Figures 10.5 and 10.6 show the placement of foils on the TNF plate.

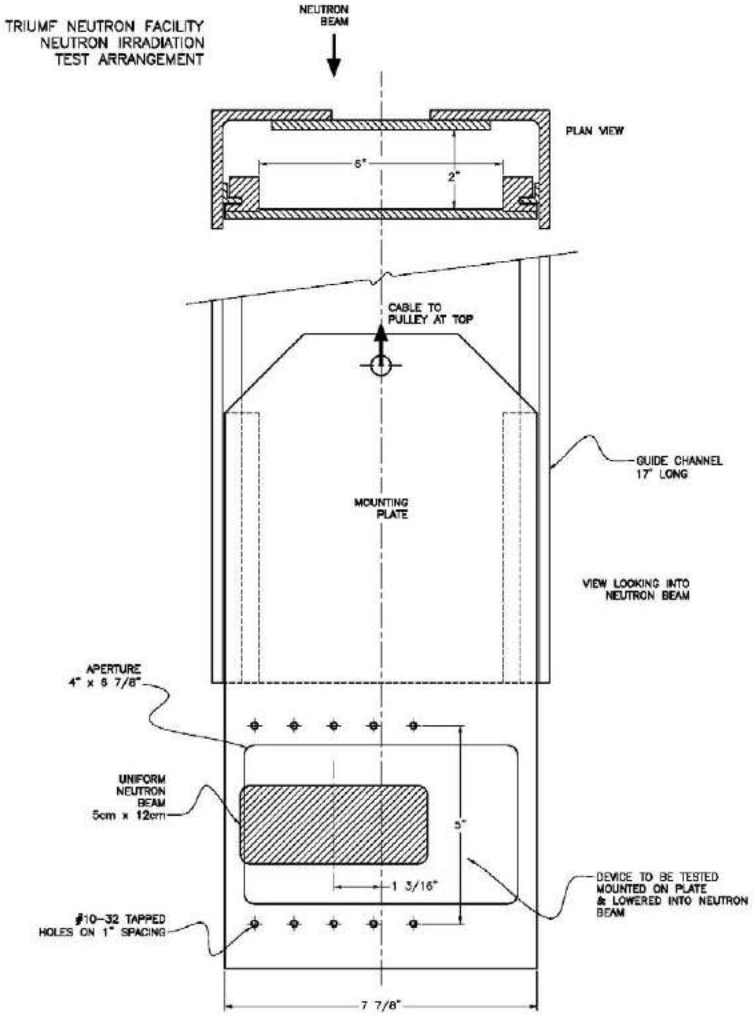

Note: The transverse dimensions of the device to be tested and its cables must fit in the aperture that is 2" deep and up to 8" wide, except where the angle track is located. There are some mounting holes on the plate at the beam position. The neutron beam is offset from the center of the plate, as indicated. Cables from the device to external electronics should be at least 20ft (6 m) and preferable 32 ft (10 m) to reach a shielded area. Access to the test position is available at all times, whether the proton beam is on or not.

Figure 10.5: Specifications of the plate used to place samples to be irradiated at TNF. The rectangular region is where the beam is most uniform [94].

Figure 10.6: Placement of foil samples on the TNF plate. From left to right: bare TNF foil, Cd-covered TNF foil, Cd-cover UCN foils, and bare UCN foil.

The TNF plate was then attached to a pulley mechanism and lowered into the beamline until the green light turned on, as seen in the photo of Figure 10.7. The data collection system then started to monitor the proton beam current and BF_3 neutron counting rate.

The samples were retrieved from the TNF plate and the data collection stopped the next day. Figure 10.8 shows a photo of the beam data collection. For safety, the collected activation was first checked while the samples were still attached to the plate. The activation was initially 20 μSv/hr, but was reduced to < 10 μSv/hr, after a few minutes. The initially high activation was due to the Al plate:

$$n(^{27}\text{Al}, ^{28}\text{Al})\gamma \rightarrow {}^{28}\text{Si} + \gamma(1.779\ MeV) + e^{-}(2.863\ MeV) + \bar{\nu}_e. \tag{10.2}$$

^{28}Al has a half-life of 2.24 min.

The samples were transferred to the health physics lab in a Pb pig for measuring the resultant γ activation in two HPGe detectors. The samples were measured individually by placing the sample flat on the surface of the crystal in Detector 1. Counts were collected by the detector for $1/2$ hr for each sample using the GENIE software package [95]. GENIE was then used to calculate the activation of each sample. The package included a black box analysis, in which an efficiency curve is supplied. The activation is calculated back to the end of the irradiation time, and includes a background subtraction. The activation is reported in Bq, or Bq/mg.

Figure 10.7: Lowering TNF plate into thermal neutron beam. The TNF plate is attached to the pulley and then lowered until the green light illuminates (seen in second figure). This ensures that the plate is placed in the correct position for uniform beam.

Start 26-Oct-2016
End 27-Oct-2016
System B1
TW # 751
MUX
Update Rate 1 Min.
Data Flow ○ Active ● Inactive

May 4, 13:04 - Select a range by dragging the mouse across the data

Figure 10.8: Current (in μA) from the cyclotron before, during, and after the irradiation.

10.5 Calculating thermal fluence

10.5.1 Irradiation data

The beam current was taken from both the BL1 sensor and the BF_3 detector at the TNF. Beamline data was collected via a TNF program that accessed xstrip data and then integrated the total beam current during the run and estimated the neutron fluence. The xstrip was set to take a beam current measurement every 5 min. For approximately 16 hrs, give or take a few minutes, the BL1 current was 106 μA. The samples were irradiated for a calculated integrated proton current of 1766 μA-hr after accounting for beam loss at the end of BL1A.

10.5.2 Measuring sample activation

The activation of each sample was measured using the same HPGe detector and then analyzed using the GENIE software from Canberra. The GENIE program used an undisclosed algorithm for integrating and combining counts in the ^{198}Au peaks. The calibration for the HPGe detector assumed small, flat samples less than 3×3 cm^2 placed on the Ge crystal to determine the activation. This calibration is called 'sfilter.' Detailed descriptions of the different efficiency calibrations are described in Section 12.2.1. Since both foils were small, the same (sfilter) efficiency calibration was used in analyzing the activation. The raw spectra of each foil are shown in Figures 10.10 and 10.11.

The peaks corresponding to ^{198}Au activation were fitted, integrated, and calibrated according to the estimated HPGe detection efficiency (see Figure 10.9), including solid angle corrections, for these peaks. The count was then calibrated for the source shape (the foils were placed on a plastic plate, which was then placed over the Ge crystal and centered over the surface of the crystal). Since only a of couple hours passed between retrieving the foils and counting the respective activations (which is small compared to the ^{198}Au half-life), the activations were not adjusted for decay (or approx. 3% decay from the end of irradiation) for this initial test. In tests performed after this, activations were adjusted for decay from the time of the end of the irradiation to activa-

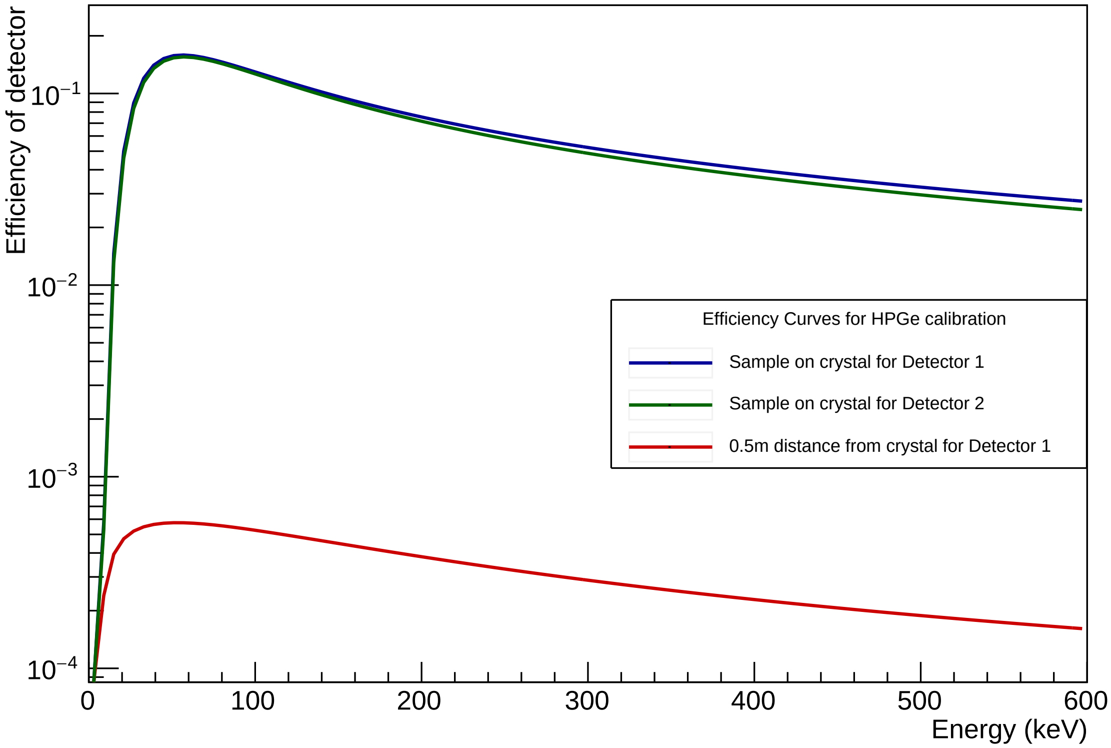

Figure 10.9: HPGe estimated detection efficiency, and acceptance correction versus γ energy for both detectors used in the measurements [96].

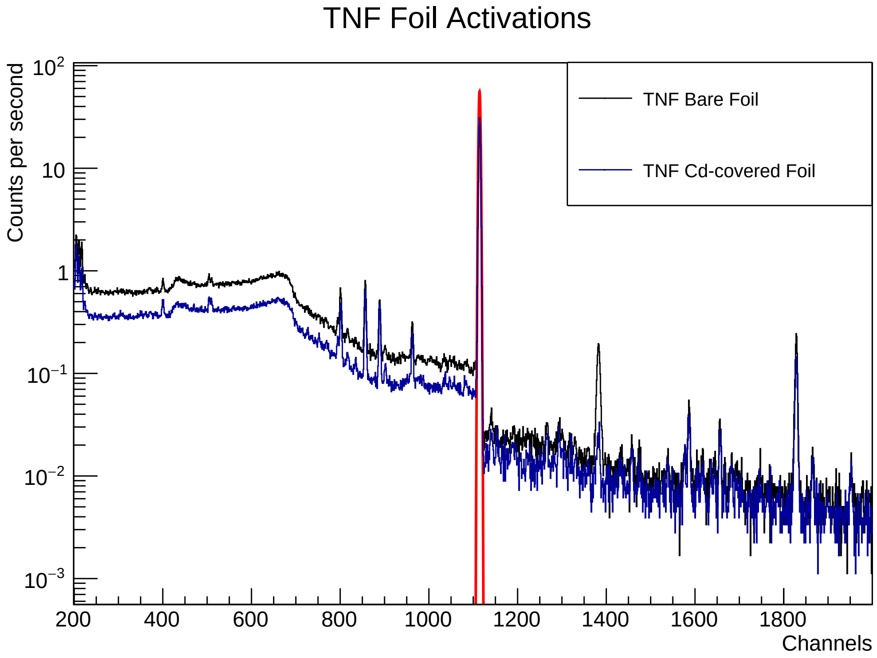

Figure 10.10: Activation spectra for the TNF foils bare (black) and with Cd cover (blue). The dominant peak for activation integration is in red.

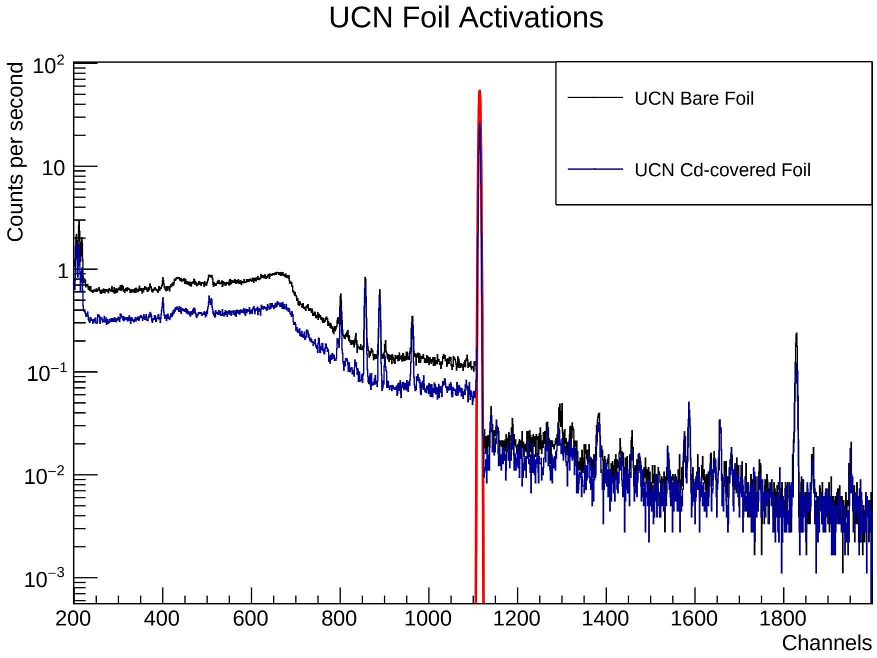

Figure 10.11: Activation spectra for the UCN foils bare (black) and with Cd cover (blue). The dominant peak for activation integration is in red.

tion data collection (estimated within 3 hrs). The activations determined for the gold samples are summarized in Table 10.2.

10.5.3 Calculated fluence

Calculating the fluence from the foil activation requires several factors: the activations of the foils with and without a Cd cover and the irradiation exposure time. Assuming the neutron flux is constant and uniform over the beam, the neutron fluence, Φ_i, for each foil is calculated ($i =$ bare or Cd-covered):

$$\Phi_i = A_i \frac{t}{A\sigma_{abs}N(1-e^{-t/\tau})}, \tag{10.3}$$

where A_i is the activity of the Au sample (with or without Cd), t is the exposure time to the neutron beam, A is the area of exposed foils, σ_{abs} is the thermal neutron absorption cross-section for ^{197}Au, N is the number of atoms per unit area exposed to the beam (number of Au atoms/cm^2 in this case), and τ is the mean lifetime of ^{198}Au.

Next, the thermal neutron fluence is calculated by subtracting the bare foil fluence from the Cd-covered foil fluence:

$$\Phi_{th} = \Phi_b - \Phi_c, \tag{10.4}$$

where Φ_b is the neutron fluence for the bare foils, and Φ_c is the neutron fluence for the Cd-covered foils. See Table 10.2 for calculated thermal fluence.

The calculated uncertainty includes the activation counting, mass, and the variation in the current in xstrip ($\sim$ 25 nA for 1 sec time bins). The uncertainty is dominated by the uncertainty in the counting.

Table 10.2: Measured activation and calculation of thermal neutron fluence using TNF foils and UCN foils.

Foil	Activation (kBq)	% Error	Area (cm^2)	Thickness (cm)	mass (mg)	Φ_i (n/cm^2)	% Error
TNF bare	11.8 ± 0.2	1.7%	5.07	0.00254	$249 \pm 1(calc.)$	$5.8 \pm 0.1 \times 10^{10}$	1.8%
TNF Cd-covered	6.7 ± 0.1	1.5%	5.07	0.00254	$249 \pm 1(calc.)$	$3.25 \pm 0.05 \times 10^{10}$	1.6%
UCN bare	11.8 ± 0.2	1.7%	2.00	0.01	$339 \pm 1(meas.)$	$4.23 \pm 0.08 \times 10^{10}$	1.8%
UCN Cd-covered	5.6 ± 0.1	1.8%	2.00	0.01	$342 \pm 1(meas.)$	$1.97 \pm 0.04 \times 10^{10}$	1.9%

10.6 Flux measurement correction factors

Using the above analysis, there was some disagreement in calculated thermal neutron fluence between the TNF foils and the UCN foils. This could have been due to statistical fluctuations in data collection, however, the biggest difference between the two sample sets was geometry, most notably thickness and shape. However, due to the difference in thickness of the foil samples, the effect of self-shielding would have the greatest effect.

For self-shielding, reference [97] includes a number of formulas to determine the effect of Au shielding itself from neutron irradiation according to increasing thickness. The TNF and UCN foils were different thicknesses, but also different shapes. However, the exposure to the beam was uniform across the foil surface. To account for this difference in thickness, we use the fluence, Φ_i, in the following relation:

$$\Phi_i = \phi_{0,i} t = K R_i t, \tag{10.5}$$

where ϕ_0 is the neutron flux through the Au foil, R_i is the reaction rate, and K is a constant to account for foil geometry and counting set-up during activity data collection with the HPGe counter. The reaction rate is given by

$$R_i = \frac{C \text{exp}(t_w/\tau)}{\epsilon N_0 (1 - \text{exp}(-t/\tau))}, \tag{10.6}$$

where C is the counting rate of the activated sample, N_0 is the number of atoms of ^{198}Au, ϵ is the detector efficiency, and t_w is the time from the end of the irradiation to the measurement of activation. This changes Eqn. 10.4 to

$$\Phi_{th} = \Phi_b - \Phi_c = K(R_b - R_c)t. \tag{10.7}$$

However, R_c requires two more corrections. 1 mm of Cd has a cut-off energy of 0.55 eV, which allows for epithermal neutron reactions; here to be denoted as F_{epi}. This factor is derived as

$$F_{epi} = \frac{g\sigma_0 f_1}{I_0} = 0.0298 \pm 0.0006, \tag{10.8}$$

where $\frac{I_0}{g\sigma_0}$ and f_1 are taken from Table 2 in [97].

There is also a departure from the $1/v$ cross section behavior for neutron energies between $5kT$ and E_{cd}(0.13 eV to 0.55 eV assuming room temperature), denoted as F_v. This factor is derived as

$$F_v = \frac{\sigma_0 w'}{I_0} = \left(\frac{g\sigma_0}{I_0}\right)\left(\frac{w'}{g}\right) = 0.00317 \pm 0.00006, \tag{10.9}$$

where again $\frac{I_0}{g\sigma_0}$ is taken from Table 2 in [97] as are the factors g and w'.

Both of these factors are affected by epithermal self-shielding, which needs to be accounted. The thermal flux also has some self-shielding, which needs to be accounted for in the subtraction. This gives the final equation:

$$\Phi_{th} = \frac{K}{G_{th}}\left(R_b - R_c\left(1 + \frac{F_{epi}}{G_{epi}} + \frac{F_v}{G_{epi}}\right)\right)t, \tag{10.10}$$

where G_{th} is the thermal self-shielding correction, and G_{epi} is the epithermal self-shielding correction.

Finding the values for these correction factors (and approximating G_{th} and G_{epi} to halfway between the experimental thicknesses given in Table 7 of [97]) and factoring in these corrections brings the two calculated fluences to within their statistical uncertainly (6%) as can be seen in Table 10.3 with the activation integration dominating the uncertainty. The only remaining factor is K, which accounts for the geometry of the foil and counter. K is approximately the same for

Table 10.3: Calculated thermal fluence, before and after epithermal and self-shielding corrections

	without corrections	with corrections
TNF calculated thermal fluence	$2.5 \pm 0.1 \times 10^{10}$ n/cm^2	$2.3 \pm 0.1 \times 10^{10}$ n/cm^2
UCN calculated thermal fluence	$3.0 \pm 0.1 \times 10^{10}$ n/cm^2	$2.2 \pm 0.1 \times 10^{10}$ n/cm^2

all foils, as all were irradiated in a uniform beam with the same orientation and counted with the same HPGe detector on the same day. Only the geometry of the different foils remains, the effect of which is minimized from adding in the effect of self-shielding.

10.7 Summary

The Au foils being used for the finding of the thermal neutron flux at a point in space around the UCN cryostat have a different geometry than the Au foils typically used at TNF. As such, when irradiating the UCN foils for finding the thermal neutron flux, differences in dimensions and self-shielding effects need to be taken into account, especially thickness. With these corrections, the UCN thermal fluence was calculated to be $2.2 \pm 0.1 \times 10^{10}$ n/cm^2, compared to the TNF calculated fluence of $2.3 \pm 0.1 \times 10^{10}$ n/cm^2 through the surface of the foils. This gives agreement in measured fluence between the different foil geometries.

Chapter 11

Simulation of the neutron fluxes and foil activations

Simulations were done to understand the flux of cold neutrons entering the UCN production volume, and to determine the thermal neutron fluxes around the cold cryostat. The simulation model included a detailed model of the biological shielding and other materials around the cryostat. The simulations were used to determine locations to place gold foils that would measure the neutron reflecting effect of the graphite moderator around the cryostat. The simulation model was developed by Tatsuya Kikawa and adjusted from there, with continued collaboration with Dr. Kikawa.

11.1 Au foil layout at TRIUMF

To measure the thermal neutron flux around the UCN source, the method of Au activation measurement was used, originally based on the PSI method described in Section 3.3. This method utilized the high thermal neutron capture cross-section of ^{197}Au. Using this method, the thermalizing effectiveness of the graphite blocks surrounding the source was studied.

The thermal and colder neutron flux can be determined by irradiation of bare Au foils and Cd-covered foils, as specified in Section 10.2. Subtracting the resulting activations, gives the activation due to thermal and colder neutrons [97] at specified positions around the cryostat.

The Au foils were chosen to be flat rectangular foils that were rolled into cylinders for a combination of reasons. The Au foil shapes were investigated to see which configuration had the foil activated with the least dependence on the combined effect of the incident angle of the incoming neutron and neutron energy. These were calculated with FLUKA simulations [70]. The sphere had no combined effect, while the wire and cylinder configurations has little to no effect at the lower energy ranges. Since only the lower energy ranges were to be measured, all three of these configurations were possible. The sphere, however, presented additional difficulties in measuring activation due to self-shielding effects, and the wire presented additional difficulties in applying a close-fitting Cd-cover. The cylindrical configuration was also less likely to catch in the pipes than the sphere and has been used in other thermal neutron measurements in the past [44]. As a result, the cylindrical configuration was used.

11.2 Preliminary calculations

To determine where to place the foils, a geometry matching the setup at TRIUMF was coded into the simulation package FLUKA [70]. This geometry included the graphite reflectors and surrounding shielding. Foils were placed around the cold cryostat to determine how the graphite affected neutron thermalization (see Figure 11.4). Peak and valley positions were noted when the graphite reflector was added to the simulation, giving positions for determining the graphite thermalization effectiveness. Drawings of the vertical placement of the pipes and the radial placement of the foil positions are shown in Figure 11.1.

FLUKA uses a number of different data sets and models for scattering cross-sections (such as ENDF/B, JEF, JENDL libraries). FLUKA has special libraries available for thermal and colder neutron scattering. The multigroup algorithm is used when the energy of the neutrons is below 20 MeV and is divided into 260 energy groups, with 31 of these groups in the thermal range [98]. Using the libraries associated with low energy neutrons requires adding FLUKA cards, such as LOW-MAT, LOW-NEUT and LOW-BIAS, although these libraries are often already activated in

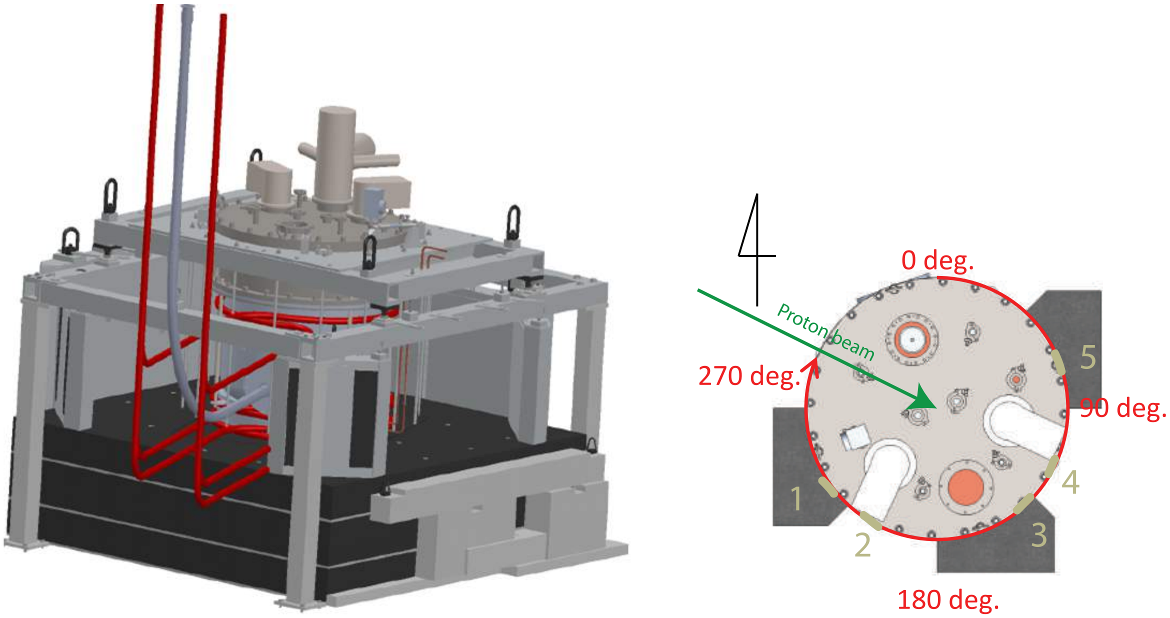

Figure 11.1: This drawing displays the locations that the foils were placed in for activation measurements. The left panel in this figure shows the pipes used to guide the foil holders into locations around the cryostat. The right panel shows the labels for the locations the foils were placed in (as numbers) for the activation measurement.

DEFAULTS. These libraries were used in the model. For graphite and carbon, the ENDF/B-VIIR0 references are used.

However, the thermalizing cross section of graphite is strongly dependent on the density of the graphite. For example, Zhou noted a 30-40 % disagreement of neutron thermalization between the MCNP5 simulation (which used the ENDF/B-VI graphite library) and measurements [99]. The graphite used here as reactor grade graphite, which has a lower thermalizing cross section (0.61 ± 0.05 bn) than pyrolytic graphite (1.40 ± 0.03 bn) [99]. If the graphite is not modeled correctly, the thermalization of the neutrons, and thus the neutrons that contribute to activating the Au, would be substantially too high or too low.

11.3 Irradiation method

Pipes were placed at three levels around the cryostat (see Figures 11.1 and 11.3). Five foils were placed in the calculated peak and valley positions around the cryostat in the lower and middle levels. Two foils were placed in the highest activated peak and valley position in the top level (see Figure 11.1).

The Au foils were ordered as a sheet from Nilaco with a thickness of 100 μm. The foils were cut into 1×2 cm^2 pieces. Each piece was numbered and had its mass measured and recorded.

For the irradiation procedure, 12 foils were selected and placed in Al boats (photograph of an Al boat with a Au foil shown in Figure 12.1) which were tied to strings that provided access to the three pipe levels. These foils were then pulled along the string to the preset positions within an error of about 2-3 cm.

The proton beam was then turned on and directed to the UCN area's tungsten target, and foils were activated by the resulting neutron flux. After the beam was turned off, the foils were retrieved, and their activation was measured with two HPGe detectors.

11.4 Simulation geometry and materials

The software used for determining the thermal neutron flux was FLUKA [98], with the FLUKA Advanced Interface ($flair$) being used to display the geometry and for debugging purposes [100]. The cryostat, surrounding materials, shielding and much of the experimental hall were included in the model. Figure 11.2 shows the expanded screenshot of the cryostat and surrounding materials in FLUKA. The black cylinders are BIASING volumes, which are used to reduce computing time by directing FLUKA where to generate more statistics. Simulations here were run to get the computing statistics of the activation down to 1 % or lower.

The experimental hall was included in the FLUKA model for other calculation purposes and is retained here. The calculations focused on the crypt area containing the cryostat. The geometry includes

- the cryostat and all of its components,
- the surrounding shielding of lead, graphite and concrete,

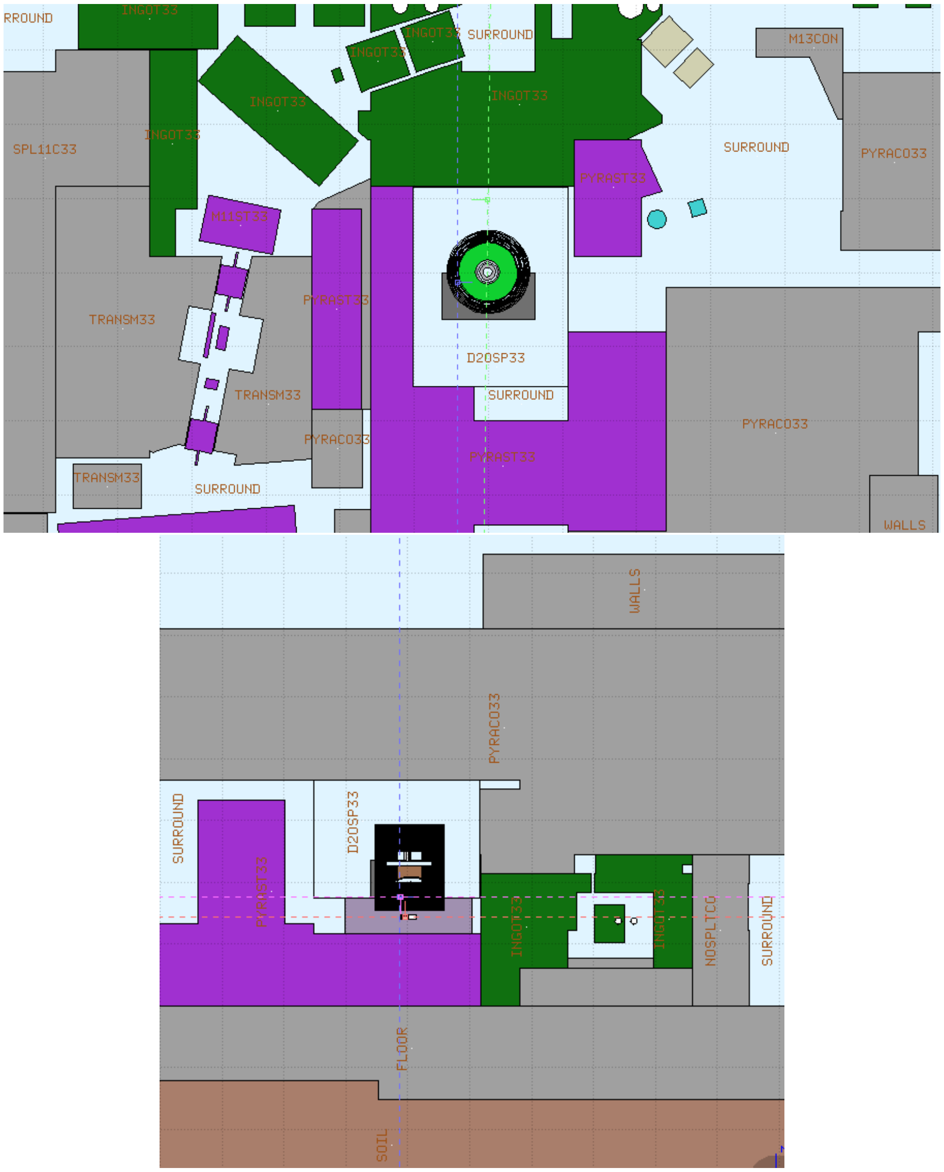

Figure 11.2: Vertical (top) and horizontal (bottom) cross sectional drawings of the cryostat and surrounding shielding in FLUKA model. The cryostat is covered with BIASING here for computing purposes.

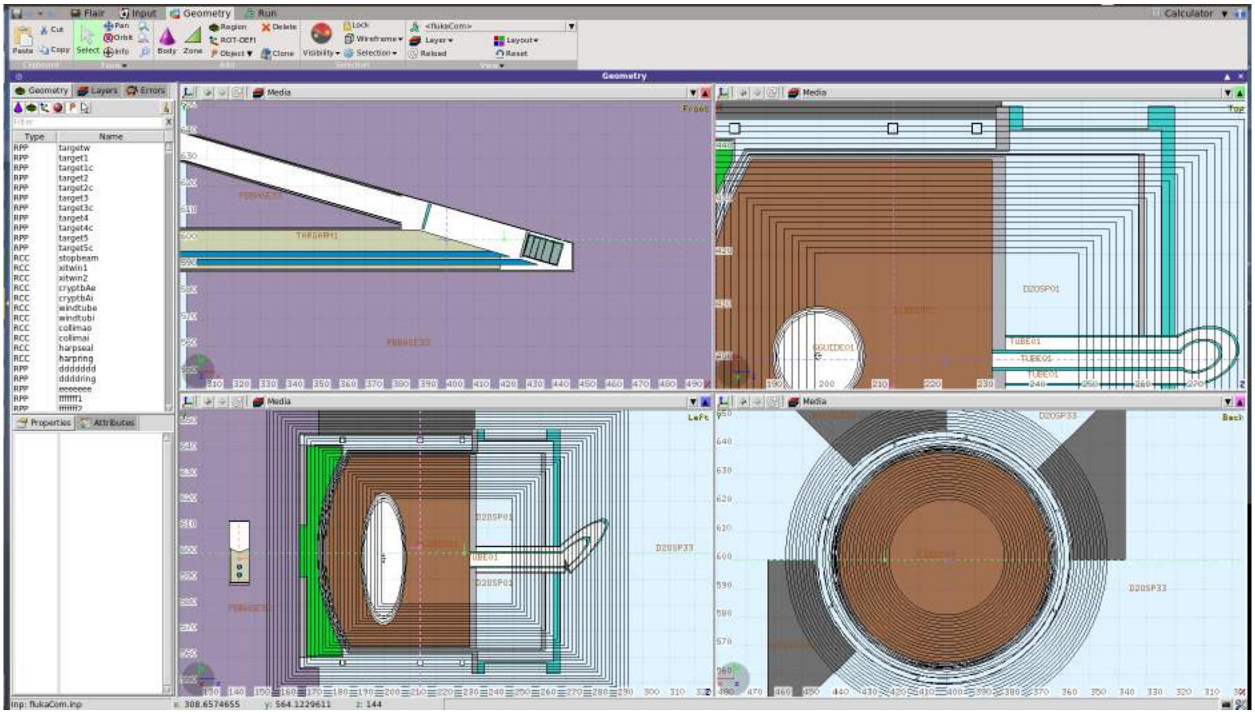

Figure 11.3: Screenshot of FLUKA simulation in Flair. Four different perspectives are shown in slices. Top left is of the tungsten target. Top right and bottom left are side slices of the cryostat. Bottom right is a top view slice of the cryostat. The numbers along the axes of each panel provide the scale in cm for these images.

- components of the Au foil placement system.

Screenshots of the cryostat and moderators in FLUKA are shown in Figure 11.3. An expanded view showing the shielding around the cryostat are shown in Figure 11.2.

11.5 Simulation model

This section will focus on the development of the Au foil placement system.

In order to determine where to place the foils, a version of the model with flat Au foils surrounding the cryostat was developed by Kikawa. The actual foils, however, were to be held in cylindrical boats, which were simulated later on.

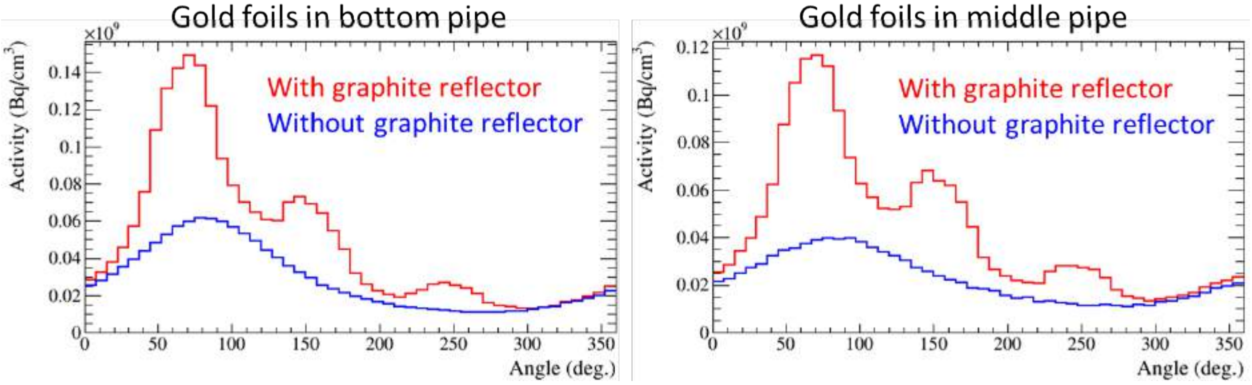

Figure 11.4: Simulation with rings of flat Au foils. The activations of the foils were subdivided around the cryostat in order to determine where the Au foils were to be placed during the measurement. The simulation included versions with (red) and without (blue) the graphite reflectors at two heights with 1 μA-hr integrated proton beam.

11.5.1 Subdivided Au foil ring simulation

Three rings of flat Au foils were simulated at three different heights around the cryostat. Heights are shown in left drawing of Figure 11.1. The foils were then divided into 48 foils per ring. After irradiation, each foil activation was calculated and plotted as shown in Figure 11.4. The simulation was run with both graphite reflectors and without. This showed that the greatest foil activation was near the graphite and the least was away from the graphite. Activating the foils in these peak and valley positions was done to check the effect of the graphite on the neutron flux around the cryostat.

11.5.2 Discrete cylindrical Au foil simulation

The next simulation used 12 cylindrical foils with a cylinder height of 1 cm, a circumference of 2 cm, and a thickness of 100 μm. This matches well the geometry of the actual foils around the cryostat and to calculate the expected activation. Five foils each were placed in the lower and middle levels at 19 cm and 47 cm above the lead base. Two more foils were placed in the high level at 63 cm above the lead base. All of the foils were placed in a peak or valley position found in the continuous simulation. A graphic representation showing the approximate placement of the foils is in Figure 11.1.

The numbering of foil positions is as follows:

- H5 and H4 are the two positions used in the highest pipe elevation. These positions are where the activation is highest (H5) and the next valley (H4) at this elevation.
- M5 - M1 are the five positions used in the middle pipe elevation. These positions are where the activation is expected to peak (M5, M3, and M1) and valley (M4 and M3).
- L5 - L1 are the five positions used in the lowest pipe elevation. These positions are where the activation is expected to peak (L5, L3, and L1) and valley (L4 and L3).

The numbering of the foils is always set to be decreasing clockwise while viewing the cryostat from above. As a result, all three '5' positions have the same x-y position but different z-positions, all three '4' positions have the same x-y position but different z-positions, both '3' positions have the same x-y position but different z-positions, etc.

The model was run with both bare foils and with a 500 μm Cd cover. Both versions were necessary to determine the thermal and colder neutron flux. The results of the simulations are shown in Figure 11.5.

11.5.3 Comparisons of calculated activations for each simulation

While the overall peak-to-valley pattern is present in both simulations, the discrete simulation has a higher calculated activation for most of the foils. This is mostly due to the difference between placing flat foils or cylindrical foils. As cylindrical foils have more Au volume for the neutrons to pass through, and the probability that the neutrons capture on the Au rises. Also, the Cd-covers cover the outside of the cylindrical foils but not the inside, so the cylindrical foils with Cd-covers have higher activation than the flat foils with Cd-covers.

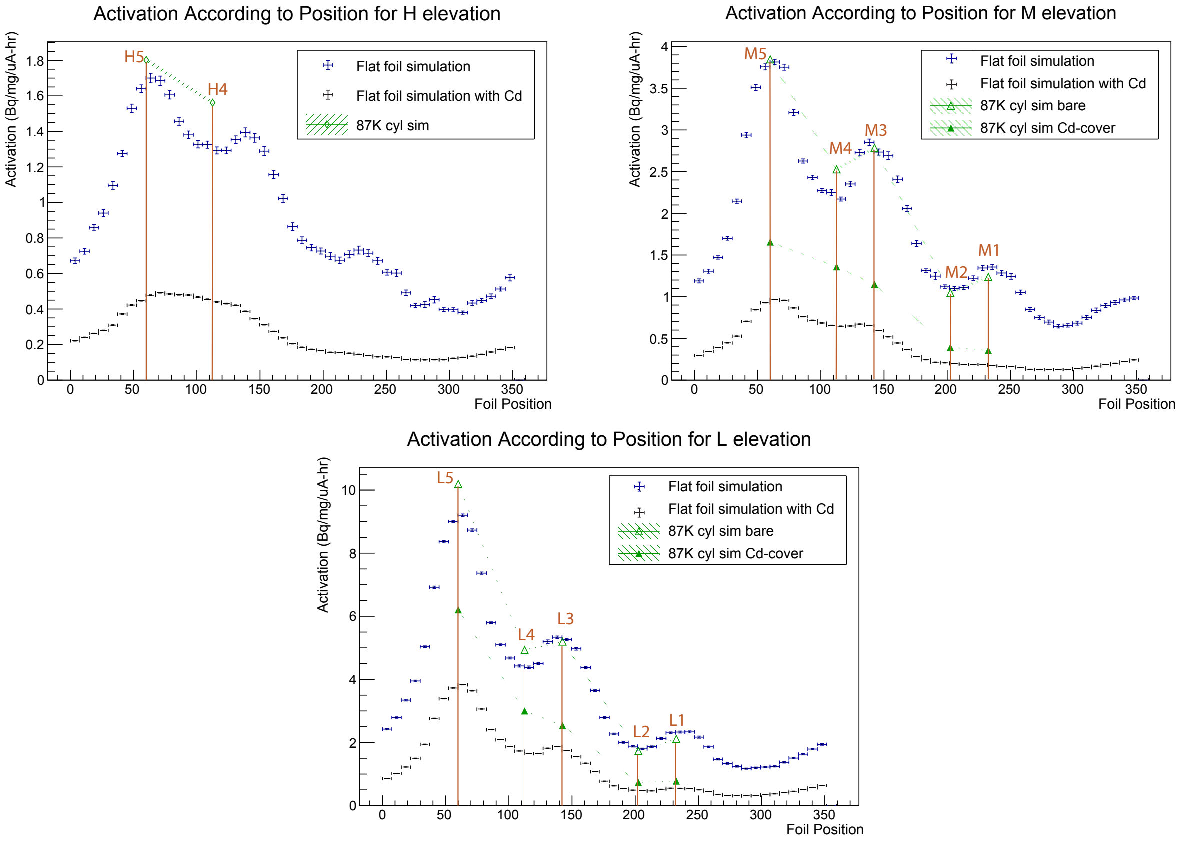

Activation According to Position for H elevation

Activation According to Position for M elevation

Activation According to Position for L elevation

Figure 11.5: Simulations with cylindrical Au foils. The foils were placed around the cryostat in 12 positions: (left) 5 in the lower level, (right) 5 in the middle level, and (bottom) 2 in the top level. Each graph shows the calculated activation for each foil with and without a Cd cover.

Chapter 12

Measurement of Au activation around the cryostat

12.1 Au activation measurement during the TRIUMF UCN source commissioning

12.1.1 Au foil insertion procedure

Forty-eight Au foils and 12 Al boats were used for the irradiation procedure. The mass of each of the Au foils was measured and recorded. The masses of the foils used are found in Table 12.1. The Al boats were tied to a string which was then pulled into place. A foil placed in the Al boat is shown in Figure 12.1. The string was a loop with markings to determine where to finish pulling to keep the boats in the predetermined position with a couple centimeters uncertainty. Four sets of twelve foils were arranged for irradiation and five Cd covers were used for a specified level. The proton beam was then impinged on the tungsten target, generating neutrons. While the intensity of the proton beam varied in each run, the total time of irradiation was calculated to bring the total integrated proton beam to approximately 0.3 μA-s ($\sim 2 \times 10^{13}$ protons on target) for each run. This integrated beam current was chosen to activate the foils enough to generate a strong γ signal

Table 12.1: Table of foil masses used in measurement. The foils were divided into four groups as shown below. The foils also had corresponding numbers to coincide with the mass reference. Uncertainties on the masses were about 1 mg.

Foil label	Mass (mg)	Foil label	Mass (mg)	Foil label	Mass (mg)	Foil label	Mass (mg)
5	335	1	349	36	342	4	365
9	336	2	354	37	339	5	335
13	334	7	351	38	336	6	339
15	337	8	358	39	356	9	336
16	338	10	351	40	335	11	343
21	330	14	356	41	359	12	325
27	336	17	354	42	341	19	342
31	334	18	355	43	360	20	338
32	330	22	356	44	332	25	329
33	335	23	343	45	330	30	327
36	342	24	358	46	330	34	328
39	328	28	350	47	363	35	338

for the HPGe detectors, without saturating the detectors.

The basic set-up and procedure for each irradiation was as follows:

- One set of 12 Au foils was brought to the access pipes above the cryostat.
- Each foil was inserted clockwise for each level and noted.
- Beam was sent on target for a total irradiation of approximately 0.3 μA-s or $\sim 2 \times 10^{13}$ protons on target.
- Beam was shut down and beam blocker put in, to allow access to the concrete shielding above the cryostat, usually in less than 10 min.
- Foils were removed from the Al boats and then allowed to further cool in the Meson Hall for usually 12-48 hrs after activation, before being brought to the health physics lab.
- Foil activation was then measured using one of the two HPGe detectors in the health physics lab.

The positions of the foils are shown in Figure 11.1, and a photo of the crypt area with the cryostat, pipes, and graphite is shown in Figure 12.2. There were more irradiations than sets of Au foils,

Figure 12.1: Photo of the Al boat used for placing the Au foil around the cryostat. The boat is in the open position in order to show the foil wrapped inside.

therefore foils were reused in later irradiations. Each set of gold foils was allowed to decay for a few half-lives before being used again. The residual activation from previous activations was accounted for as is described in Section 12.2.1.

12.1.2 Current normalization data

Since the irradiation for each set of foils differed from run to run, the proton current data was recorded. The proton beam current data was collected from the BL1A sensor upstream of BL1U. This program was used for the practice measurement as described in Section 10.3, but in this experiment was not calibrated for beam loss downstream of the cyclotron, as the tungsten target was much closer to the BL1A sensor. The first five irradiations were taken with the current being sampled at 5 s intervals, as shown in Figure 12.3; the remaining six irradiations were taken with the current being sampled at one second intervals, as shown in Figure 12.4. Taking the stable part of the runs and applying a Gaussian fit to the frequency distribution was done to determine the uncertainty of the beam intensity. For the 1 μA runs, the beam had a maximum variation of less than 5% and usually between 1 and 2%. Taking the stable portions of the lower intensity runs, where available, and applying the fit, gave uncertainties that varied between 2 - 9% and 18% for Run 10.

The proton beam current from the cyclotron varied from measurement to measurement, as this period also served as an engineering run to test the new beamline's EPICS system at TRIUMF, and to learn how to steer the beam into BL1U. While the beam tuning looked good for the first run, the

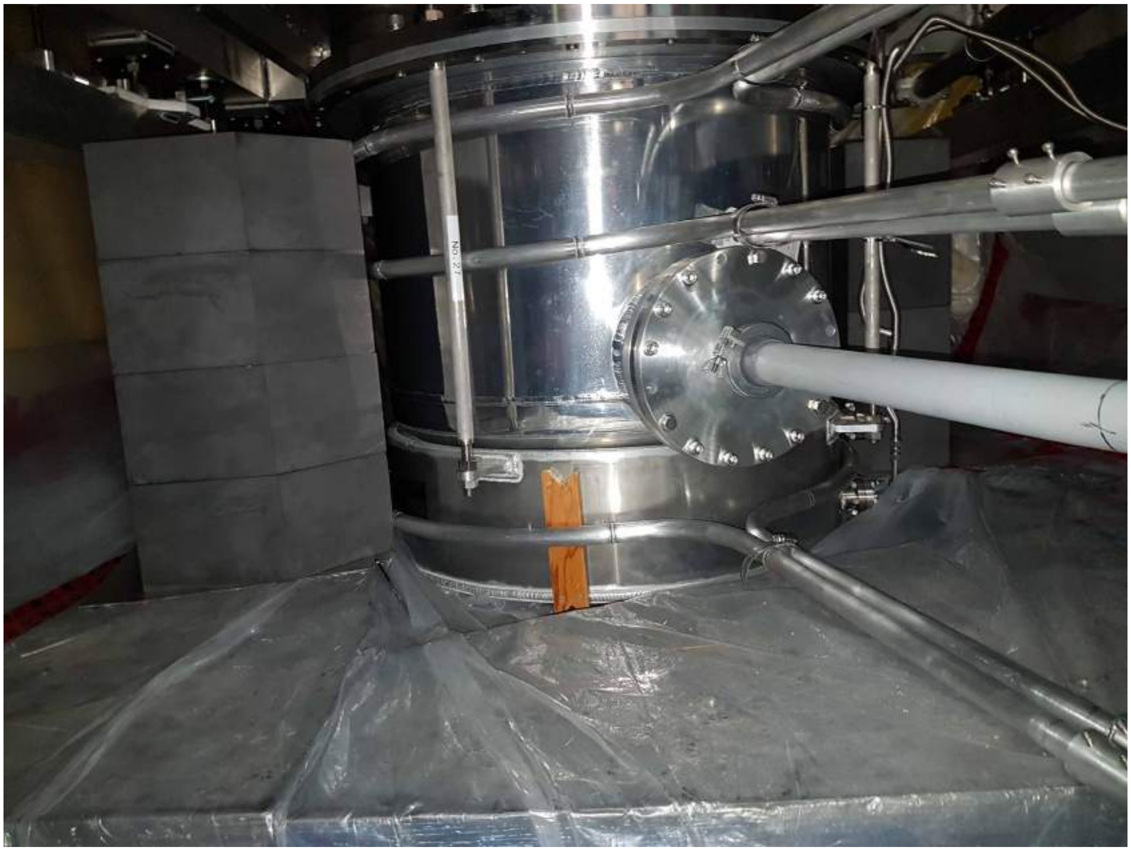

Figure 12.2: Photograph of cryostat with pipes for foil placement and the surrounding graphite columns. Only one column of graphite is seen here, but there were three columns for the measurement.

tuning was more difficult for the next run. As a result, the current intensity was gradually increased for Run 2. Runs 3 and 4 were done on the same day and with beam tuning similar to Run 1. Run 5 showed a problem in the 1VB1 data (horizontal beam steering magnet) and a sudden increase in temperature in the right collimator thermocouple, so the irradiation was stopped to check the beam profile and then the irradiation was completed. During the irradiation of Run 6, it was noted that the temperature had risen about 1^o C on the right collimator thermocouple. A number of beam tuning tests were performed prior to the next measurement, and from Run 7, the current intensity was reduced to 50 nA. In Run 8, the beam intensity could only get up to 45 nA. In Run 9, the current was set at 78 nA to keep the intensity to less than 100 nA. The reason for this was that at 80 nA the extraction current readback switched to a higher gain setting and caused glitches in data. For Run 10, there was trouble getting the beam intensity above 40 nA, but eventually the intensity got up to 55 nA. In Run 11, the beam was stable at 70 nA before irradiation, but dropped during irradiation. The operators got the beam back up to 80 nA, but not in a stable manner.

As a final note regarding the beam stability, the current reaching the target was at a lower intensity than is typically used at TRIUMF. The toroid used for measuring the beam current usually has an uncertainty of about 5% at high intensities (such as 100 μA). However, since the intensity was at 1 μA or lower, the current measurement precision cannot be better than 10%. This uncertainty related to the BL1A sensor's uncertainty, not the stability of the beam itself. This does not include the current readout uncertainty, which as mentioned before, varied according to current intensity and stability. This uncertainty was added into the uncertainty of the normalization. The total integrated current for all irradiations is shown in Table 12.2.

12.2 Foil activation

12.2.1 Systematic corrections

This section describes the systematic corrections to the activation measurements due to the HPGe detectors.

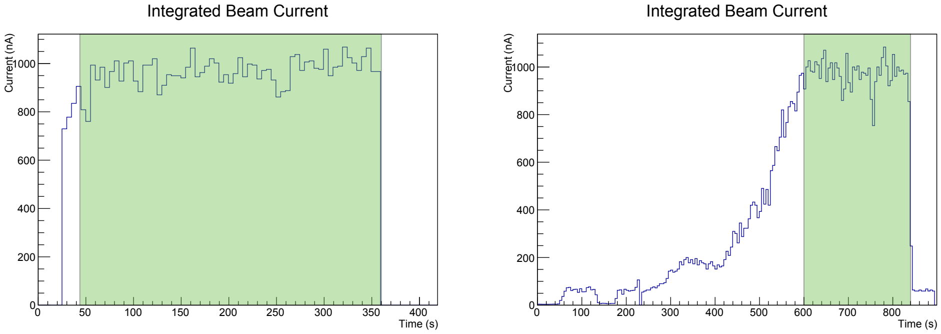

(a) Run 1 (b) Run 2

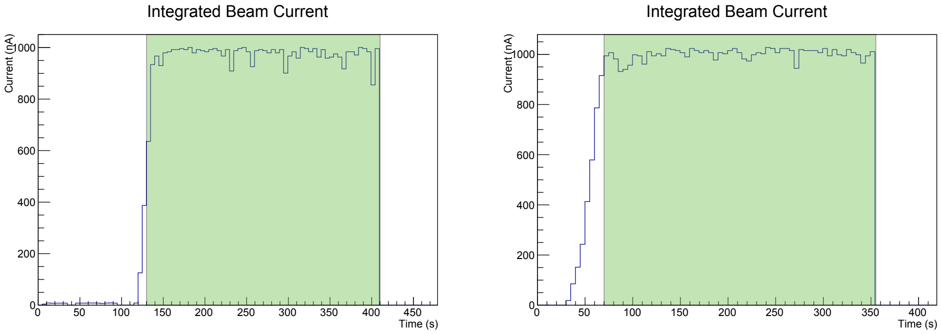

(c) Run 3 (d) Run 4

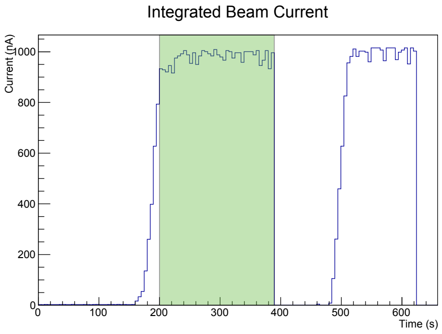

(e) Run 5

Figure 12.3: Each of the graphs shows the measured beam over the course of the first 5 irradiation runs in the order taken. Each sample was taken at 5 second intervals. The highlighted regions show the data section used for calculating the beam stability for each run.

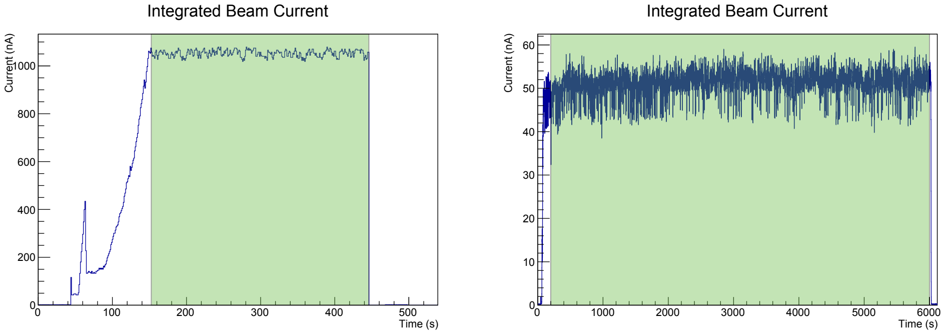

(a) Run 6

(b) Run 7

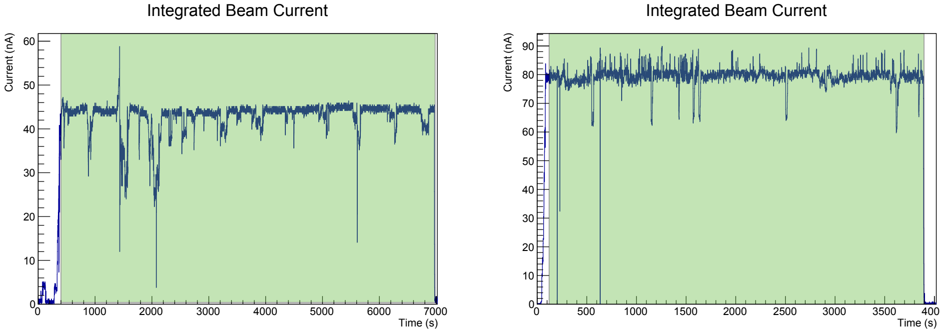

(c) Run 8

(d) Run 9

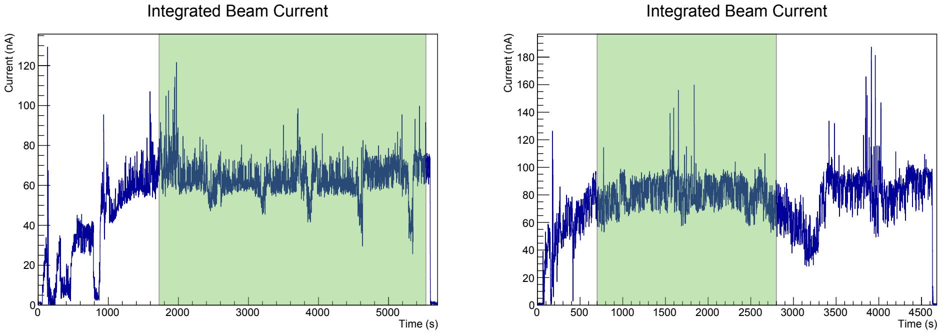

(e) Run 10

(f) Run 11

Figure 12.4: Each of the graphs shows the measured beam over the course of the remaining 6 irradiation runs in the order taken. Each sample was taken at 1 second intervals. The highlighted regions show the data section used for calculating the beam stability for each run.

Table 12.2: Table of irradiation runs and the integrated current. Uncertainty is dominated by the calibration (estimated to be 10%).

Run Number	Temperature (K)	Date	Start Time	End Time	Integrated Beam (uA-s)	Precision
1	126	Nov. 22nd	20:10	20:17	321 ± 32	5 sec intervals
2	87	Nov. 23rd	15:14	15:28:17	364 ± 36	5 sec intervals
3	8	Nov. 29th	8:01	8:09	275 ± 27	5 sec intervals
4	35	Nov. 29th	21:39	21:46	301 ± 30	5 sec intervals
5	8	Dec. 2nd	11:36	11:43	324 ± 32	5 sec intervals
6	65	Dec. 6th	7:20	7:28	352 ± 35	1 sec intervals
7	8	Dec. 12th	18:07	19:49	306 ± 31	1 sec intervals
8	49	Dec. 13th	13:57	15:54	284 ± 28	1 sec intervals
9	300	Dec. 20th	2:51	3:57	304 ± 30	1 sec intervals
10	300	Dec. 20th	12:01	13:36	312 ± 31	1 sec intervals
11	Empty	Dec. 21st	22:39	23:56	349 ± 35	1 sec intervals

First, there are two HPGe detectors with unique efficiency and acceptance (geometry correction) as a function of gamma ray energy. The HPGe detectors also have more than one calibration available to account for the different acceptance for different distances from detector to sample and different sample sizes. The main calibration used for both detectors was for placing the sample on the Ge crystal surface, called 'sfilter'. The efficiency (including geometry correction for this set-up) was estimated to be $3.90 \pm 0.39\%$ for detector one, and $3.59 \pm 0.36\%$ for detector two for the 411 keV γ energy. The other calibration, called '0.5mpole,' was used when the sample was placed 0.5 m above the Ge crystal. The 0.5mpole calibration had an efficiency plus geometry correction of $0.0220 \pm 0.0005\%$. This calibration placed the sample 0.5 m above the Ge crystal. The further measurement point was used when the foils were activated enough that they caused more than 10% deadtime at the sfilter calibration. The efficiency curve was estimated using a ^{152}Eu source with a known activation, as shown in Figure 12.5. From Figure 12.5 we estimate the uncertainty in efficiency is 10% for the sfilter calibrations and 2% for the 0.5mpole calibration.

At the same time as the thermal neutron measurement, there was a measurement with various metals and metal oxide powders placed in the He-II volume of the cryostat, called the cold neutron measurements. These activations were measured with both detector calibrations and showed

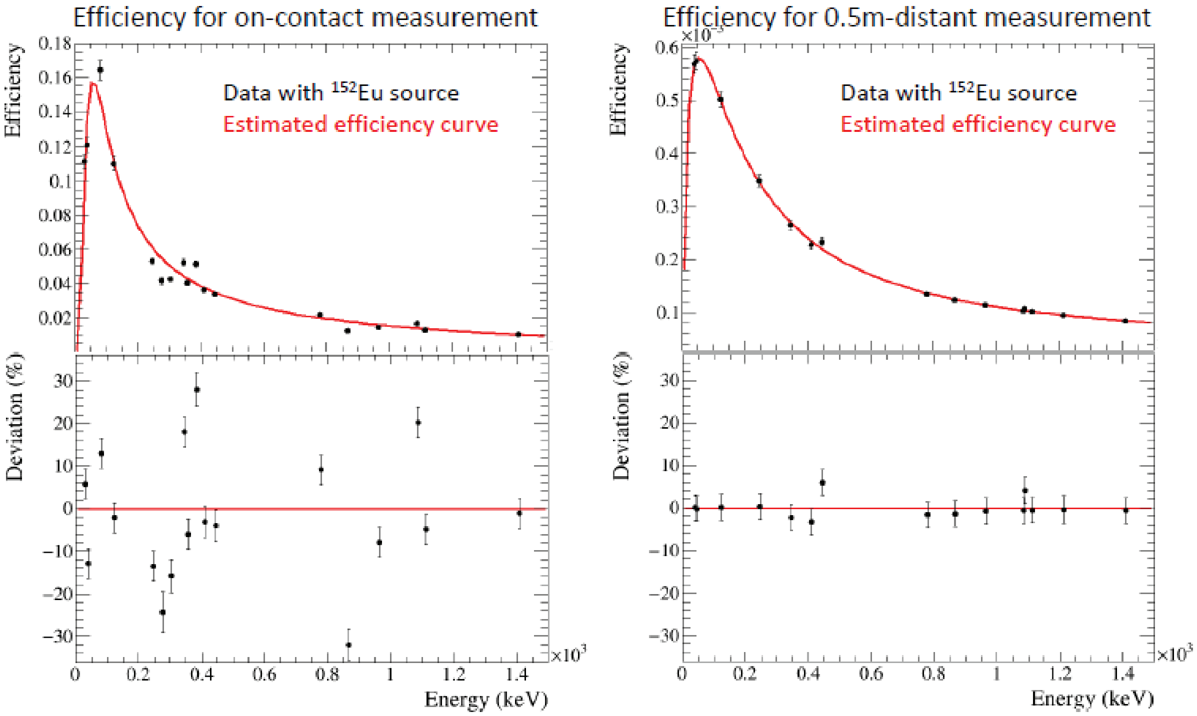

Figure 12.5: Comparison of the estimated efficiency curve with known ^{152}Eu source for one of the HPGe detectors for two calibrations. The right is with the surface calibration and the left is with the 0.5 m distant calibration. Figure and data from [70]

Table 12.3: The gold activation data in this table is from the cold neutron analysis from [70]. The columns are divided according to calibration to show the activation differences between the sfilter and 0.5m pole calibrations.

Temperature of data run	Activation using sfilter calibration (Bq/mg/5μA-min)	Activation using 0.5m pole calibration (Bq/mg/5μA-min)	middle point (Bq/mg/5μA-min)	spread (Bq/mg/5μA-min)
8	1025.85	782.032	903.941	121.909
8	1022.6	741.697	882.1485	140.4515
8	894.677	669.096	781.8865	112.7905
35	984.499	713.472	848.9855	135.5135
48	1023.18	803.674	913.427	109.753
65	1057.9	884.368	971.134	86.766
87	1122.31	855.761	989.0355	133.2745
126	1235.86	978.501	1107.1805	128.6795
300	1448.59	1110.85	1279.72	168.87
300	1291.53	1023.51	1157.52	134.01

a consistently higher measured activation for the surface calibration than for the 0.5 m distant calibration [70]. The activation of the ^{198}Au placed in the He-II volume using both calibrations is shown in Table 12.3. The difference between these measurements is taken as an uncertainty in the measurement due to peculiarities of the HPGe detector's black box activation determination. To adjust for the calibration systematic effect, the thermal neutron activations were shifted to the middle point between the calibrations found through the cold neutron measurements. Both the calibration variation, and the deviation of the estimated efficiency curve from the known ^{152}Eu sample were taken as systematic uncertainties.

Second, in the efficiency calibrations the HPGe detectors used the GENIE software to determine the activation of ^{198}Au using all the activation peaks. The main activation peak is 411.7 keV. There was a noted variation in measured activations in the other peaks, possibly due to lack of statistics in these other peaks. A manual analysis was performed on the HPGe spectra to determine the activation using the 411 keV peak. This manual analysis used the raw counts in the 411 keV peak divided by livetime of the HPGe detector. The counts in the 411 keV peak were found by fitting a Gaussian, and by subtracting off the estimated background. The difference due to the background subtraction was always less than 1%. The integrated Gaussian and its corresponding uncertainty were then used to calculate the activation, in terms of activation per unit of beam on target by

$$\frac{A}{I} = \frac{N/t_{live}}{\epsilon I m \exp\left(-t/\tau_{Au}\right)}, \tag{12.1}$$

where N/t_{live} is the background-subtracted count divided by HPGe detector live time, ϵ is the detector efficiency including geometry correction, I is the integrated proton beam current, m is the mass of the Au foil, t is the time from the end of irradiation to data collection, τ_{Au} is the mean-life of ^{198}Au and A is the calculated activation.

The foils used in the activations were reused for the later measurements. While the foils were left to cool for a few half-lives before being reused, there was a small residual activation remaining. This residual activation was also subtracted from the measured activation.

12.2.2 Normalized activations

Since the simulation is limited to two temperatures (87 K and 300 K) the comparison to simulation is most relevant for the 87 K and 300 K measurements. The 8 K data by itself is interesting since it was measured three times and may provide some insight into the repeatability of the results.

Systematic uncertainties were accounted for in the measured values, and were summed quadratically. The systematic uncertainties dominate over the statistical uncertainties. The accounted uncertainties in the data are listed below:

- Current Integration: Estimated to be 10%.

- Calibration variation: The activity measured was slightly different for different HPGe calibrations. The variation was calculated from the cold neutron data which included measuring the Au sample activations at both calibrations and was more than 10% depending on the measurement [70].

- Mass: The uncertainty (0.3%) was small ($\sim$ 1 mg) compared to the measured values ($>$ 300 mg).

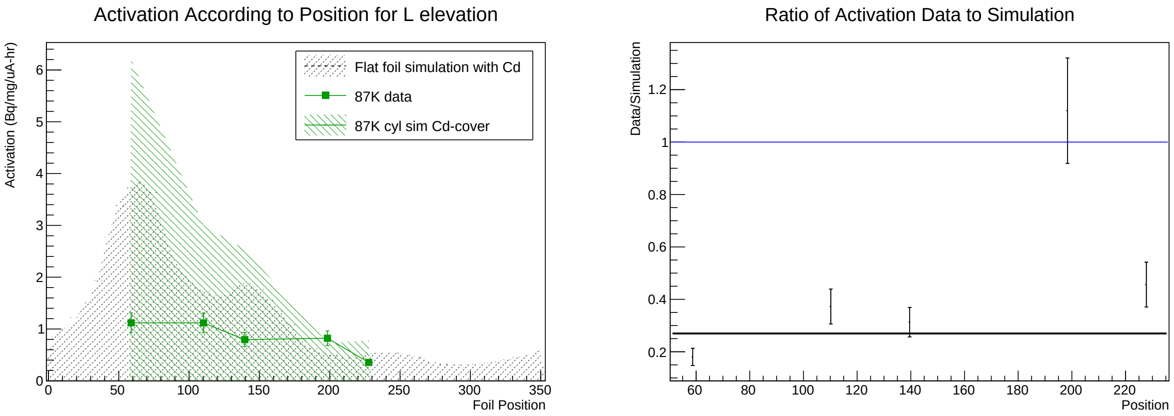

Figure 12.6: Activation results for foils in L positions at 87 K. The left panel shows the measured data and the simulated results. The right panel shows the ratio of the measured data over the simulated data for the cylindrical model. This level used Cd-covers.

- Activation measurement: The manual method of finding the activation of the foils was used. The Gaussian fit over the peak provided the statistical uncertainty (1% or less).
- Time of activation measurement: The time the activation of the foil that was measured was given a 3 hr uncertainty, which was small as compared to the Au half-life.

After systematic uncertainties and corrections were considered the simulation and measured data were compared. Figures 12.6 to 12.8 show the data for the 87 K measurements taken from irradiation Run 2 and Figures 12.9 to 12.11 show the data for the 300 K measurements from irradiation Runs 9 and 10. Positions are kept according to radial position around cryostat as outlined in Section 11.5.2.

87 K measurement - lowest level

The 87 K measurement at the lowest level is compared to the simulation in Figure 12.6. In Figure 12.6, the foils were covered with Cd. The measured peak and valley behavior was not clearly visible, and looked consistent with a slope. Position L2 was the only position to agree with the simulation, the other positions were 20% to 40% of the expected activation.

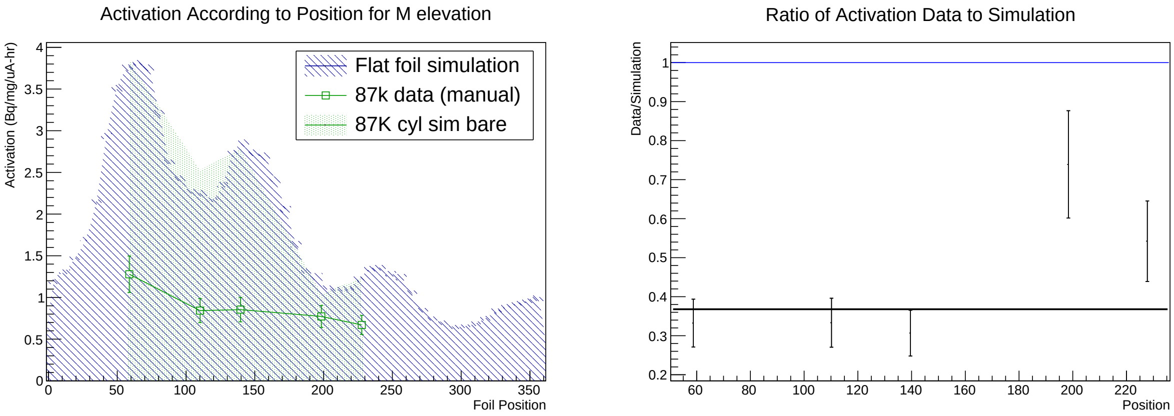

Figure 12.7: Activation results for foils in M positions at 87 K. The left panel shows the measured data and the simulated results. The right panel shows the ratio of the measured data over the simulated data for the cylindrical model. This level used bare foils.

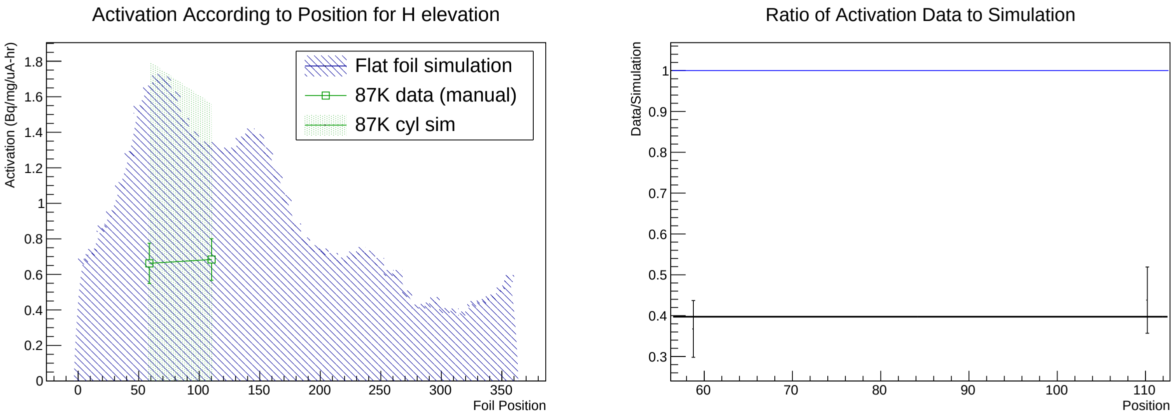

Figure 12.8: Activation results for foils in H positions at 87 K. The left panel shows the measured data and the simulated results. The right panel shows the ratio of the measured data over the simulated data for the cylindrical model. This level used bare foils.

87 K measurement - middle level

The 87 K measurement at the middle level is compared to the simulation in Figure 12.7. In this part of the measurement, the foils were bare. There was a slightly visible peak and valley behavior in positions M5-M3, but the data is 30 - 70% of the simulation, with M2 being the closest to agreeing.

87 K measurement - highest level

The graphs for the 87 K high level measurement are in Figure 12.8. In this part measurement, the foils were bare, and there were only two foils in positions H5 and H4. The M5 position measured

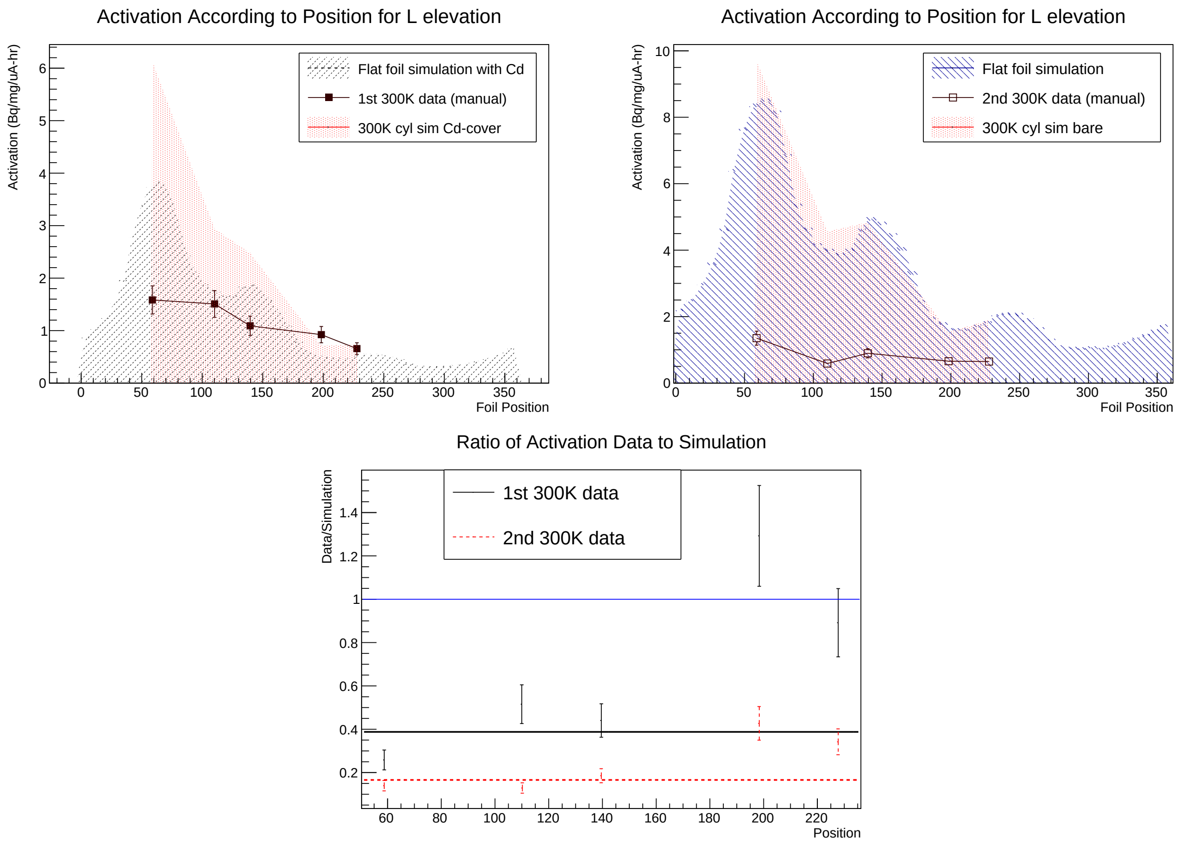

Figure 12.9: Activation results for foils in L positions at 300 K. Top left is the measured data and the simulated results for the first measurement. Top right is the measured data and the simulated results for the second measurement. First measurement used Cd-covers; second measurement used bare foils. Bottom is the ratio of the measured data over the simulated data for the cylindrical model for both measurements.

to 37 $\pm$ 15% of the simulation and the M4 position measured to $44 \pm 18\%$ of the simulation.

300 K measurements - lowest level

The graphs for the 300 K lowest level measurement are in Figure 12.9. In these two measurements, the first (irradiation Run 9) was done with Cd covers, the second (irradiation Run 10) with bare foils. In the first measurement, the inverted peak and valley behavior occurred. In the second measurement, the peak and valley behavior occurred but was substantially less than the simulation. Only one point in the first measurement agreed with simulation, L1. Position L4 was close to agreeing by about 10%.

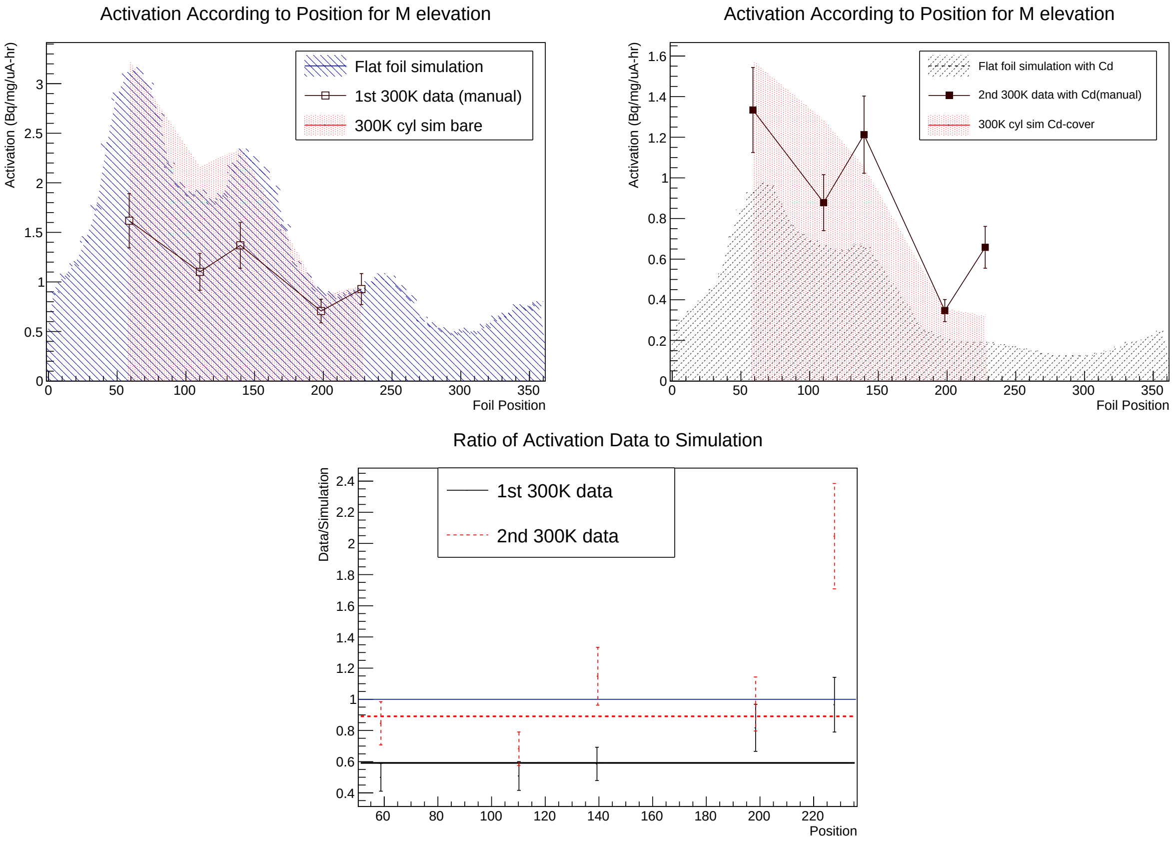

Figure 12.10: Activation results for foils in M positions at 300 K. Top left is the measured data and the simulated results for the first measurement. Top right is the measured data and the simulated results for the second measurement. First measurement used bare foils; second measurement used Cd-covers. Bottom is the ratio of the measured data over the simulated data for the cylindrical model for both measurements.

300 K measurements - middle level

The graphs for the 300 K middle level measurement are in Figure 12.10. In these two measurements, the first (irradiation Run 9) was done with bare foils and the second (irradiation Run 10) with Cd-covers. The peak and valley behavior occurred here for both measurements. The second measurement had closer agreement with positions M3 and M2 agreeing with simulation and M5 less than 10% from agreement. In the first measurement, only M1 agreed with the model, although M2 was close to agreement.

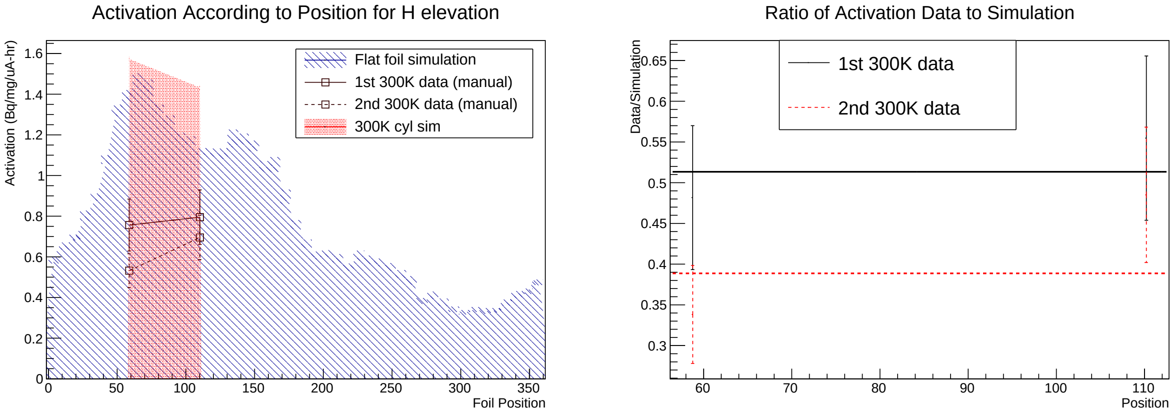

Figure 12.11: Activation results for foils in H positions at 300 K. The left panel shows the measured data and the simulated results for both measurements. The right panel shows the ratio of the measured data over the simulated data for the cylindrical model. This level used bare foils.

300 K measurements - highest level

The graphs for this measurement are in Figure 12.11. Both of these two measurements were done with bare foils. Since this is the high position, there were only 2 positions, H5 and H4. The measured activations agreed with each other, but not to the model.

12.2.3 Discussion

There were a number of notable discrepancies of the data from the simulation.

The two top level H positions were largely present as a means to check for current normalization. These positions always had bare foils which gave a rough estimation of lowering flux at larger height, but more importantly, gave a reference point to compare irradiation runs of the same temperature. The uncertainty of the proton current was estimated to be about 10% due to the reduced efficiency of the proton current toroid at low intensities [93], but the top positions for the 300 K measurement data just barely agree with each other, which shows some consistency in the flux measured at that temperature.

The middle level positions showed the most peak-and-valley behavior for determining the effect of the graphite reflectors in the data, but again, the data did not agree with the simulation. The 87 K measurement showed an almost flat activation with angle and the second 300 K measurement was actually too high in two positions. Most of the positions measured too low, not too high.

The low level position showed the largest variation from the simulation. The activation was closer to the middle level in magnitude, but there was a deviation from the peak-and-valley expected behavior. In both Cd-covered measurements, there was an inverted peak and valley behavior with one position, M4 in the first 300 K measurement, higher than the simulation. The second 300 K measurement had the correct peak and valley pattern, but the total activation was substantially lower than the model.

Overall, the positions most likely, or closest to agreeing with the model tended to be closer to the lower estimated activation positions, 2 and 1. Several possible sources of uncertainty which could have been the cause of the disagreement between the model and measured activation are discussed in the next chapter.

Chapter 13

Systematic uncertainties and corrections to activation results

There were a number of differences between the simulations and data in the Au activation measurements. A change in the proton beam impinging on the target may have an effect on the neutron flux around the cryostat. The proton current reading was taken at BL1A, but not at the UCN tungsten target, and was not calibrated for a small proton current loss from BL1A to the tungsten target. For reference, the TNF experienced about 60% less proton beam than the BL1A reading. The loss was due to the position of the TNF. The proton beam travelled the full length of BL1A passed through several production targets for secondary beamlines before reaching the TNF. This was far from the BL1A sensor and resulted in substantial beam loss. However, the UCN target was at the beginning of BL1A, so proton beam loss would be expected to be small to negligible. As a result, the thermal neutron measurements were not calibrated for proton beam loss. The measured activations were typically three to five times smaller than the simulation in many of the positions. Such a large deficit in activation could not only be due to a slightly lower proton beam current on target.

Also, positions 5, 4, and 3 on all levels tended to deviate the most from the expected activation (please see Section 11.5.2 for review of foil placement format), while positions 2 and 1 were closer to agreement. In order to better understand why the simulation varied from the data, in particular at these two points, two types of tests were carried out. First, the settings of the model were checked and adjusted, as is described in Sections 13.1 to 13.9, to better match the simulation foil positions to the real setting. The second set of tests involved bringing materials to the TNF and measuring potential shielding effects as is described in Section 13.11. The effects these studies had on the analysis is summarized in Section 13.10.

13.1 Simulation adjustments

A number of simulation adjustments were carried out to try to understand possible causes for the discrepancies observed. First, the positions of the materials in the model were compared to photos of the cryostat. Then a few adjustments were put in at the L5 position to see if angling the Au foil or placing wood near that position would cause a shielding effect. The discrete simulations were run without the graphite. And finally, adjustments to the beam target system were attempted, such as changing the placement of the origin of the beam to permit more beam divergence before hitting the tungsten target. All of the simulation results with different adjustments compared to data are shown in Appendix A.2, and are described in the following sections.

Each model was compared to data in the form of a χ^2, where the $ndf = 12$ degrees of freedom, due to the twelve measurement points. The change in χ^2 from one model to the next is compared for the 87 K measurement and for both 300 K measurements, in order to determine which adjustments improved agreement.

13.2 Material placement

One of the potential reasons that the simulation varied with the data was that the materials might not be placed at the same locations in the model as in the measurement. All of the materials were checked and then in the photographs, it was noted that the lowest pipe was below the transition between the warm D_2O and the cold D_2O, rather than above, as originally assumed. The photo showing the pipes around the cryostat is shown in Figure 13.1. Lowering the lowest level of foils to below this transition line (about 10 cm) in the simulation caused the change in the foil in position L4 to have that higher activation than L3 in the 300 K measurements, although the overall agreement was worse for these measurements (for irradiation Runs 9 and 10, the χ^2 went from about 400 and 1400 to 1500 and 6800). The agreement improved in the 87 K comparison (for irradiation Run 2, the χ^2 went from about 4300 to 3300). This correction was maintained for the remaining simulation adjustments.

13.3 Adjustments of foil positioned at L5

The measured activations of foils placed at position L5 were drastically lower than the model, usually about three times lower than simulation, but up to nine times lower than simulation. Due to this observation, there is likely a strong shielding effect at that position. Two variations in the simulation were tried at position L5: one with added wood surrounding the pipe at position L5, and one with the foil rotated at its greatest angle without hitting the pipe wall (rotated up 25° and horizontally by 35°).

As can be seen in Figure 13.1, there are wood spacers used to keep the foil folder pipes in place for the lowest level. To put a constraint on how large an effect this could have on the measured activation, a simulation with wood surrounding the pipe at position L5 was done. The wood was assumed to be of typical yellow pine, of density 0.448g/cm^3 and composed of 50% C, 42% O, and 8% H by mass.

Also, since the orientation of the foil could not be guaranteed, a simulation with the foil at L5 rotated at its greatest possible angle, within the confines of the Al pipe was also run.

The addition of wood and changing the angle of the foil placement had little effect. Variations in the activation of the foil at L5 varied no more than 6% for the angled foil and the added wood for the 87 K Cd-covered simulation. There was slight disagreement (less than 0.1% outside of agreement) with the angled foil for the no Cd 300 K measurement. L5 with the 87 K no Cd and the 300 K Cd-covered simulation did not vary outside of uncertainty for both the angled foils. The

Figure 13.1: Photograph of the crypt area of the cryostat. The pipes for foil placement are situated around the outside of the cryostat. The welding line shows the transition between the warm volume and the cold volume.

wood had no change outside of uncertainty. The angled foil appeared to possibly have a slight effect of less than 6%, but not a large effect, which is required here. The change in χ^2 for the 87 K measurement went from about 3300 to 3700 for adding the wood and to 3000 for angling the foil. For the 300 K measurements, the χ^2 values were about 1500 for Run 9, and 6800 for Run 10 before the adjustments. With the addition of wood, the χ^2 became about 1600 for Run 9 and 6900 for Run 10. With the angled foil, the χ^2 became about 1600 for Run 9 and 7200 for Run 10. The simulation activation results for these models are shown in Appendix A.2 in Tables A.12 to A.15.

13.4 Removing graphite in simulation

The placement of the graphite in the simulation could have been different from the experimental setup. The maximum effect to the measurement would be if there had been no graphite at all. While this is not a realistic situation, it puts a bound on how much the activation could be changed if there had been a huge change in the graphite reflector.

This simulation was the same as the material placement correction, but with the graphite reflectors set to air. This reduced the activation of all the foils, and the foil at L5 by less than half. The agreement is closer with more data points agreeing within uncertainty. For the 87 K measurement, the χ^2 went from 3300 to 1000. For the 300 K measurements, the χ^2 of Run 9 went from 1500 to 450, and the χ^2 of Run 10 went from 6800 to 2900.

This suggests that the graphite model in the simulation could be significantly incorrect.

13.5 Proton beam placement

FLUKA has a number of characteristics required for the proton beam: the intensity in protons/s, the length of irradiation time, the energy of the protons in GeV, the momentum spread, divergence, and the spatial distribution of the beam cross section. The strength of the beam was set to 3500 μA-s for most of the runs. Switching from 3500 μA-s to 350 μA-s scaled linearly in calculated activation and the activation was always scaled according to the integrated beam. The energy of the protons was set to 480 MeV. The beam was set to be uniform in momentum with flat beam divergence, as in all the protons had the same momentum and direction. The spatial distribution of the protons across the cross section was set to gaussian with a FWHM of 0.58 cm in the x direction and 2.5 cm in the y direction.

In all of the previous simulations, the proton beam was placed immediately in front of the tungsten target. To gauge some possible spread of the beam before hitting the target, the origin of the beam was backed up along the beam pipe in the simulation by several meters. Some points were affected by this spread; other points less so. For the 87 K simulations, the top positions had an overall reduction in activity, the graphite positions in the middle level were slightly lower, M2 was slightly higher, and M4 had no change within statistical uncertainty. For the 300 K simulations, positions H4, M5, M2, M1, L4, L2, and L1 had statistically the same activations, while the remaining positions had reduced activations. The effectiveness of the graphite may be affected by beam spread. For the 87 K measurement, the χ^2 went from 3300 to 2700. For the 300 K measurements, the χ^2 of Run 9 went from 1500 to 1300, and the χ^2 of Run 10 went from 6800 to 5500.

The possibility of beam spread is explored in detail in Section 13.12.

13.6 Removing graphite and proton beam placement

To gauge the combined effect of reducing graphite and increasing the beam spread, both of the adjustments were simulated together. This improved the agreement more than removing the graphite. For the 87 K measurement, the χ^2 went from 3300 to 960. For the 300 K measurements, the χ^2 of Run 9 went from 1500 to 350, and the χ^2 of Run 10 went from 6800 to 2600.

Considering the slight improvement in the combination, there is a possibility that the combined difference in the graphite or even other moderators and proton beam affected the activation.

Table 13.1: Table showing the contamination changes to the moderators before and after the assays.

Graphite (density 1.7 g/cm^3)			
Before		After	
Element	Fraction	Element	Fraction
C	1	bound C	0.8
		amorphous C	0.2
V	4.0×10^{-7}	V	0.000125
Fe	2.6×10^{-5}	Fe	3.0×10^{-7}
B	3.0×10^{-6}	B	2.0×10^{-6}
Lead (density 11.35 g/cm^3)			
Before		After	
Element	Fraction	Element	Fraction
Pb	0.999915	Pb	0.999
Ag	8.0×10^{-6}	Ag	0.0000999
As	5.0×10^{-6}	As	0.000878
Zn	4.0×10^{-6}	Cd	0.0000056
Cu	0.00001	Cu	0.0001
Sb	8.0×10^{-6}	Sb	0.000878

13.7 Moderator contamination

Assays were performed on both the lead and graphite for potential contamination. For the lead, the primary form of contamination was from antimony. For the graphite, the main contamination of concern were vanadium and boron. These contaminations were added to the simulation. The change in contaminations are summarized in Table 13.1. The density of the graphite was also noted to vary between 1.66 to 1.87 g/cm^3 but was set to 1.7 g/cm^3 in the simulation.

This had the best fit to the data of the last three adjustments, but not as good as without any graphite. For the 87 K measurement of Run 2, the χ^2 went from 3300 to 2300. For the 300 K measurements, the χ^2 of Run 9 went from 1500 to 1000, and the χ^2 of Run 10 went from 6800 to 5400.

There is a possible reason for this in terms of the graphite used in the experiment and the graphite model in FLUKA. Higher densities of graphite contain only crystalline carbon, which has a high neutron thermalizing cross-section. However, reactor grade graphite contains a grain and pore structure. The grains contain both crystalline carbon and binder carbon atoms [99]. As a result, the neutrons do not only interact with the crystalline carbon structure, but with the combined structure, giving a lower neutron thermalizing cross-section. This means that below the Bragg cutoff energy for graphite (2 meV), pyrolytic graphite thermalizes neutrons more than reactor grade graphite.

The libraries for carbon differ in whether the carbon is bound or free (amorphous). Since the graphite here is reactor grade graphite, 20% of the carbon was set as amorphous and uses a free gas model for calculating interactions. Both carbon libraries are ENDF-VIIR0.

13.8 Variation in D_2O volume

Frozen D_2O is about 10% larger in volume than liquid D_2O. Due to this constraint, the cold D_2O volume wasn't always completely filled. This volume was filled to a minimum of approximately 80%. When frozen, the 80% liquid became 88% frozen. This was put into the simulation. While it resulted in some reduction of activation, this adjustment had a lesser effect of than last three adjustments. For the 87 K measurement, the χ^2 went from 3300 to 2600. For the 300 K measurements, the χ^2 of Run 9 went from 1500 to 1200, and the χ^2 of Run 10 went from 6800 to 6100.

13.9 Beam hitting collimator

During irradiation Run 5, the proton beam was noted to hit the collimator. Please see Section 13.12 for the discussion of this proton beam drift. Since the proton beam was noted to drift horizontally to the right, a simulation was run where the beam was set to partially hit the collimator (a drift of approximately 3 cm). While this showed some improved agreement, it was not as good as the contaminated moderators. This also still assumes a stable beam, but Section 13.12 demonstrates that large variations in activations can occur when the beam hits the collimator. For the 87 K measurement, the χ^2 went from 3300 to 2800. For the 300 K measurements, the χ^2 of Run 9 went from 1500 to 1200, and the χ^2 of Run 10 went from 6800 to 5600.

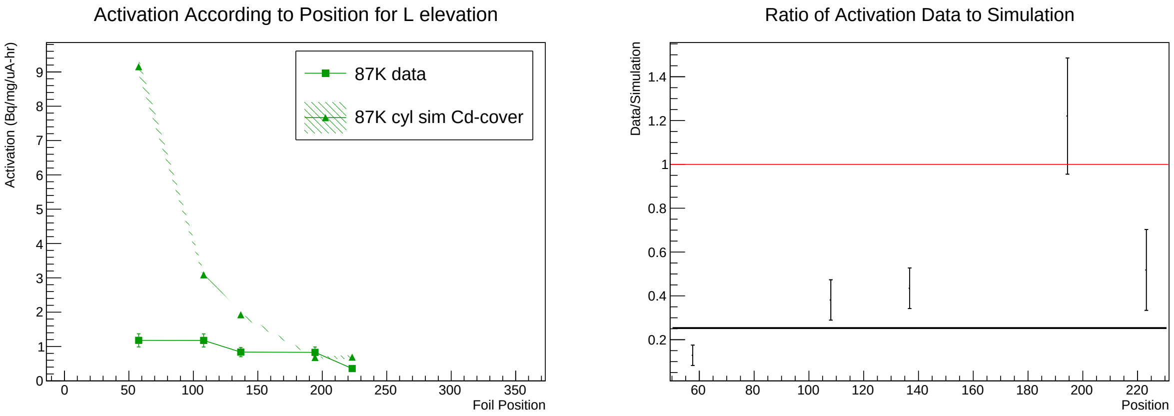

Figure 13.2: Activation results for foils in L positions at 87 K after adjusting the simulation (Irradiation Run 2). The left panel shows the measured data and the simulated results. The right panel shows the ratio of the measured data over the simulated data for the cylindrical model. This level used Cd-covers. To the right is the ratio of the 2nd measurement over the 3rd measurement. The red line is the agreement and the green line is the average disagreement.

13.10 Comparison of simulation with all adjustments to data

After comparing the simulation adjustments, the moderators have the most systematic effect on the activation. As an aside, the mis-steering of the proton beam can completely change the expected activation behavior, but this effect is not systematic. Since the monitoring of the proton beam was fairly minimal, the level of this systematic effect was hard to estimate. The model without the graphite still has the closest agreement of the simulations. However, the graphite was indeed present in the experiment, so the contaminated moderator model is compared here.

The following Figures 13.2 through 13.7 show the results of the changes in the simulation compared to data. The χ^2 comparison for the 87 K measurement is in Table 13.2 and the χ^2 comparisons for both 300 K measurements is in Tables 13.3 and 13.4. All of the measured data and simulation are available in the Appendix in Section A.2 in Tables A.12 to A.19.

13.10.1 87 K measurement - lowest level

The lowest level of the 87 K measurement used Cd-covers. The measured data and adjusted simulation are shown in Figure 13.2. Since the position of the L foils was brought down, the total

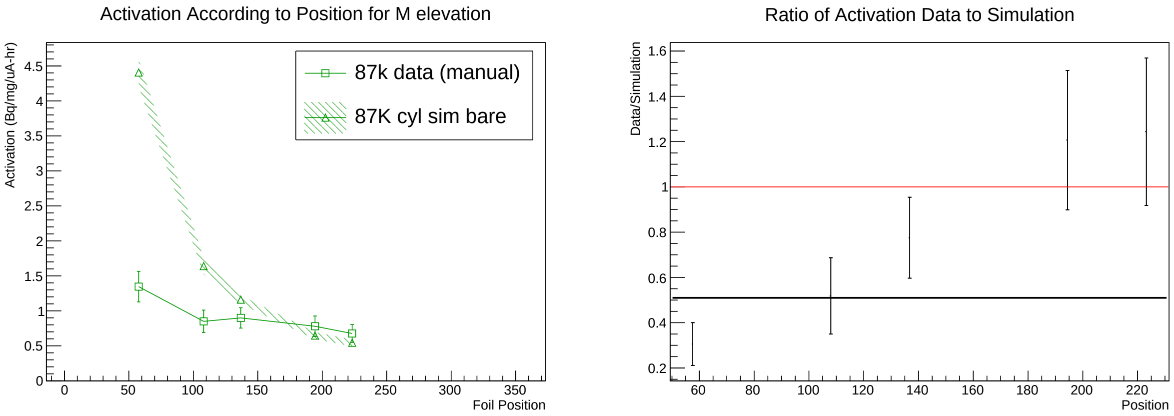

Figure 13.3: Activation results for foils in M positions at 87 K after the simulation adjustments (Irradiation Run 2). The left panel shows the measured data and the simulated results. The right panel shows the ratio of the measured data over the simulated data for the cylindrical model. This level used bare foils. To the right is the ratio of the 2nd measurement over the 3rd measurement. The red line is the agreement and the green line is the average disagreement.

activation went up, resulting in less agreement in L5. The L2 position still agrees, however. L3 and L1 have closer agreement with L3 improving to more than 40% and L1 improving to about 50% of the expected activation.

13.10.2 87 K measurement - middle level

The middle level of the 87 K measurement used bare foils. The measured data and adjusted simulation are shown in Figure 13.3. After adjustments, the agreement went from no agreement to two points agreeing, M2 and M1. M3 is less than 10% to agreement. M5 is about 30% of the expected activation and M4 is about 50% of the expected activation.

13.10.3 87 K measurement - highest level

The highest level in the 87 K measurement used bare foils. The measured data and adjusted simulation are shown in Figure 13.4. After adjustments, the activations of H5 is about 35% and H4 is about 50% of the expected value. This gives about a 5% improvement for H4, but no effect on H5.

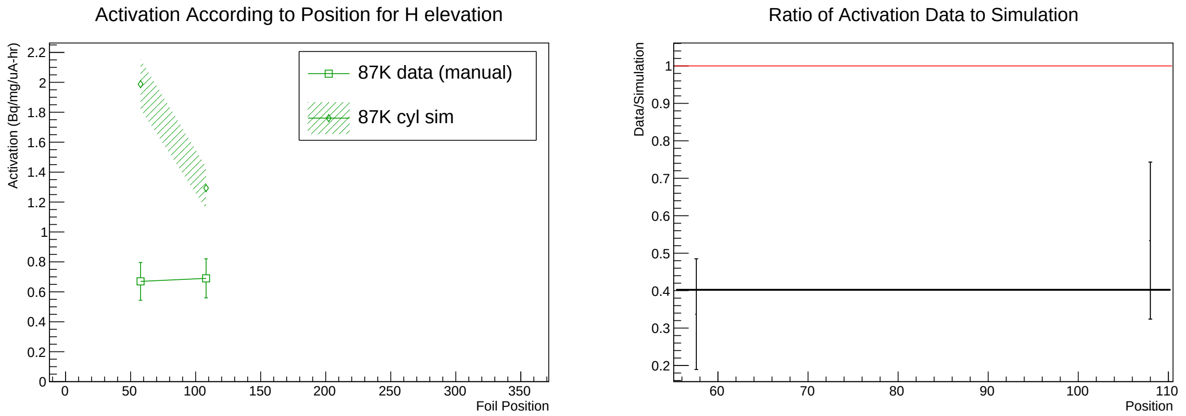

Figure 13.4: Activation results for foils in H positions at 87 K after the simulation adjustments (Irradiation Run 2). The left panel shows the measured data and the simulated results. The right panel shows the ratio of the measured data over the simulated data for the cylindrical model. This level used bare foils. To the right is the ratio of the 2nd measurement over the 3rd measurement. The red line is the agreement and the green line is the average disagreement.

Table 13.2: Comparison of Data to Simulation for 87 K (Activation in Bq/mg/μA-s)

Foil position	Data	Original simulation	Contaminated moderator	Less D_2O	Beam hit collimator
h5	0.67 ± 0.13	1.802 ± 0.012	1.99 ± 0.17	1.73 ± 0.09	2.11 ± 0.14
h4	0.69 ± 0.13	1.561 ± 0.010	1.29 ± 0.14	1.12 ± 0.05	1.18 ± 0.06
m5	1.35 ± 0.22	3.847 ± 0.017	4.40 ± 0.19	4.10 ± 0.21	4.47 ± 0.20
m4	0.85 ± 0.16	2.527 ± 0.015	1.63 ± 0.12	1.88 ± 0.23	1.68 ± 0.16
m3	0.90 ± 0.15	2.784 ± 0.017	1.16 ± 0.06	1.16 ± 0.10	1.24 ± 0.12
m2	0.78 ± 0.15	1.045 ± 0.012	0.65 ± 0.05	0.81 ± 0.09	0.74 ± 0.10
m1	0.68 ± 0.13	1.236 ± 0.013	0.54 ± 0.05	0.64 ± 0.06	0.59 ± 0.06
l5	1.18 ± 0.19	9.683 ± 0.019	9.15 ± 0.23	9.85 ± 0.18	10.08 ± 0.19
l4	1.18 ± 0.19	4.565 ± 0.017	3.09 ± 0.09	3.40 ± 0.10	3.23 ± 0.07
l3	0.84 ± 0.14	4.832 ± 0.016	1.93 ± 0.04	1.96 ± 0.05	1.90 ± 0.03
l2	0.83 ± 0.16	1.541 ± 0.016	0.68 ± 0.02	0.77 ± 0.04	0.83 ± 0.03
l1	0.36 ± 0.07	1.895 ± 0.011	0.69 ± 0.06	0.62 ± 0.02	0.83 ± 0.10
χ^2		4255	2287	2565	2777

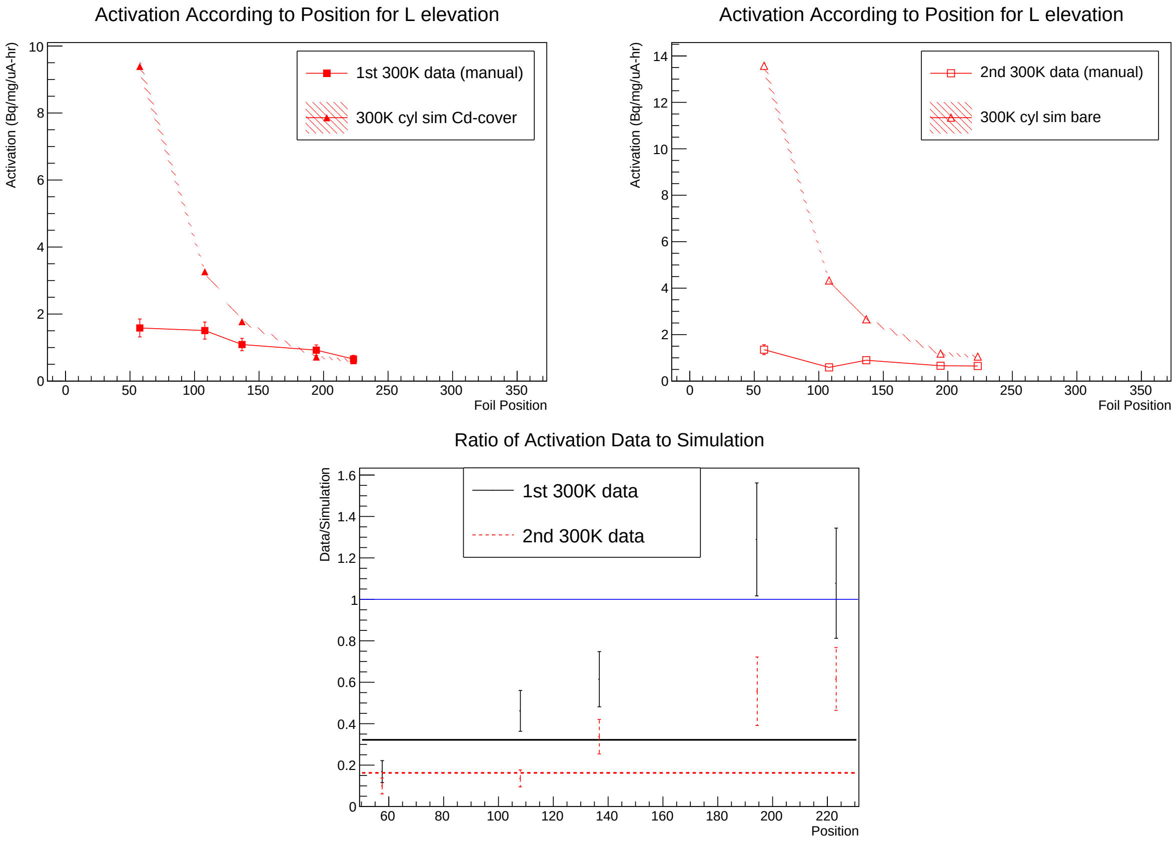

Figure 13.5: Activation results for foils in L positions at 300 K after adjusting the simulations (Irradiation Runs 9 and 10). Top left is the measured data and the simulated results for the first measurement. Top right is the measured data and the simulated results for the second measurement. The first measurement used Cd-covers; the second measurement used bare foils. Bottom is the ratio of the measured data over the simulated data for the cylindrical model for both measurements. The blue line is the agreement line, the black line is the averaged disagreement for the first 300 K measurement and the red, dotted line is the averaged disagreement for the second 300 K measurement.

13.10.4 300 K measurement - lowest level

The first 300 K measurement used Cd-covers and the second 300 K measurement used bare foils for the lowest level. The measured data and adjusted simulation are shown in Figure 13.5. After the adjustments, L1 from the first measurement still agreed. L2 is less than 10% from agreement. L3 went from less than 50% to about 60% of the expected activation. In the second measurement, L3, L2, and L1 are closer to agreement. L3 improved from about 20% to not quite 40% of the expected activation while L2 and L1 went from about 40% to about 60% of the expected activation. L5 and

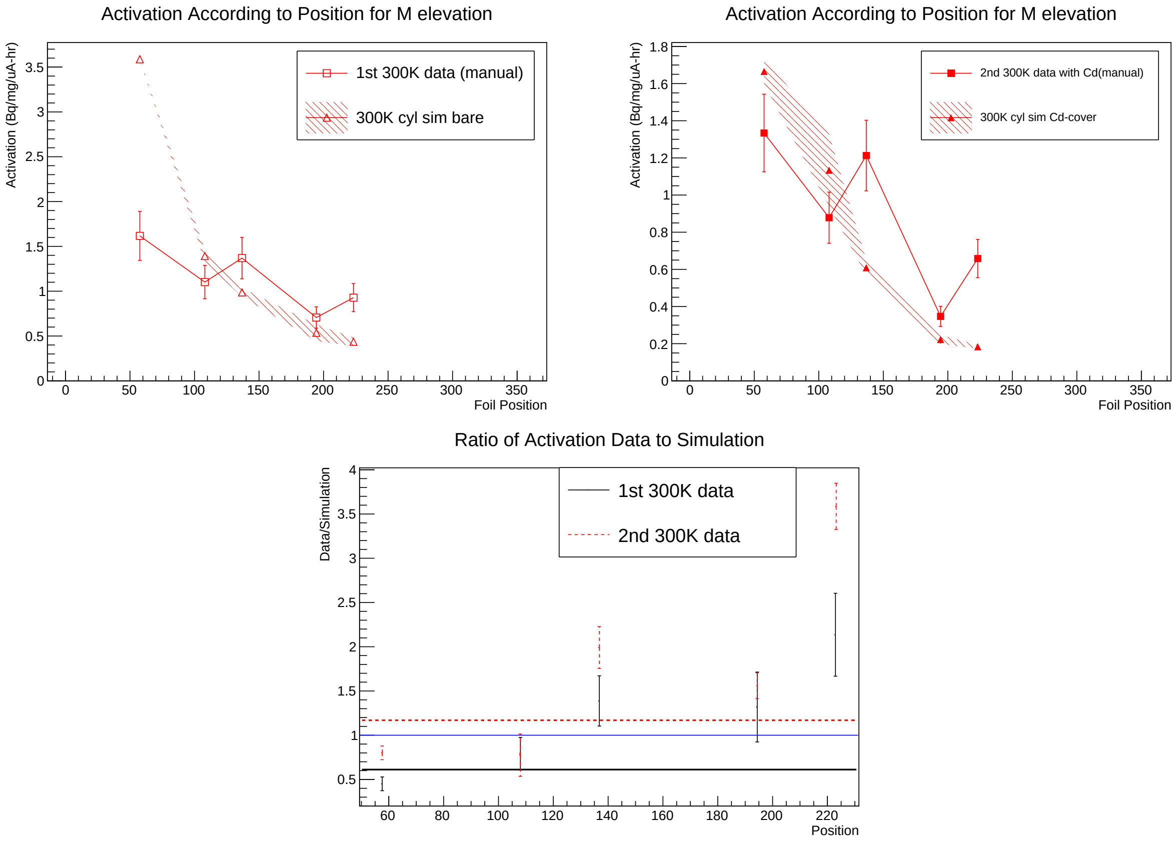

Figure 13.6: Activation results for foils in M positions at 300 K after adjusting the simulation (Irradiation Runs 9 and 10). Top left is the measured data and the simulated results for the first measurement. Top right is the measured data and the simulated results for the second measurement. First measurement used bare foils; second measurement used Cd-covers. Bottom is the ratio of the measured data over the simulated data for the cylindrical model for both measurements. The blue line is the agreement line, the black line is the averaged disagreement for the first 300 K measurement and the red, dotted line is the averaged disagreement for the second 300 K measurement.

L4 were still less than 20% of the expected activation.

13.10.5 300 K measurement - middle level

The first 300 K measurement used bare foils and the second 300 K measurement used Cd-covers for the middle level. The measured data and adjusted simulation are shown in Figure 13.6. In the first measurement, M2 just barely agrees, but M1 no longer agrees. M4 and M3 are both within less than 10% to agreement. M5 is still about 50% of the expected activation. In the second measurement, M5 is a little further from agreement. However, now M4 agrees but not M3, which

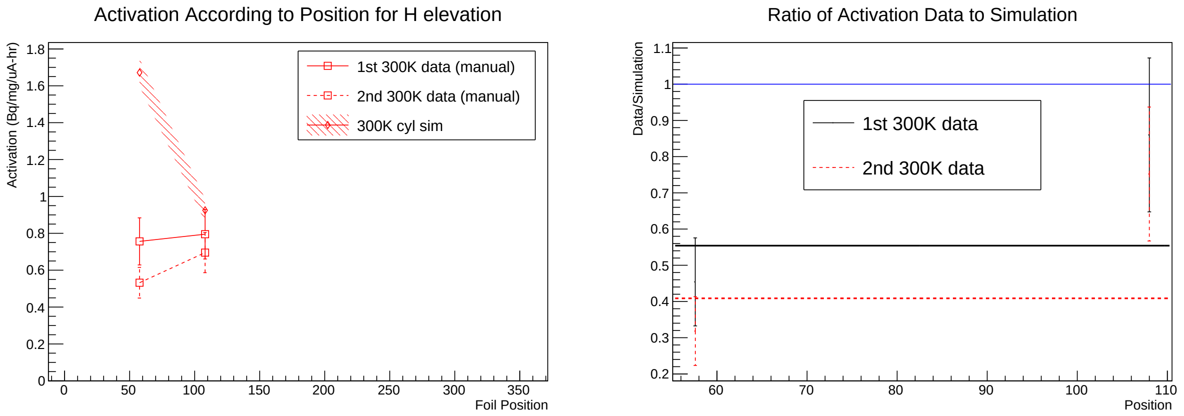

Figure 13.7: Activation results for foils in H positions at 300 K. The left panel shows the measured data and the simulated results for both measurements (Irradiation Runs 9 and 10). The right panel shows the ratio of the measured data over the simulated data for the cylindrical model. This level used bare foils. The blue line is the agreement line, the black line is the averaged disagreement for the first 300 K measurement and the red, dotted line is the averaged disagreement for the second 300 K measurement.

is about 2 times higher than expected activation. M2 is also higher than expected, but about 1.5 times higher. M1 is more than 3 times higher than expected.

13.10.6 300 K measurement - highest level

Both 300 K measurements used bare foils for the highest level. The measured data and adjusted simulation are shown in Figure 13.7. H4 in the first measurement agrees when previously no positions agreed. H4 in the second measurement is about 80% of the expected activation, up from about 50%. H5 is about 35% of the expected activation, nominal change. H5 in the first measurement improved by less than 5% to the expected activation, also nominal change.

13.10.7 Commentary on adjustments

While the adjustments in the simulation brought closer agreement to measured activation in the 87 K measurements, this did not occur with the 300 K measurement. There are a number of topics to note about the simulation model.

The foils were held in Al boats which were then tied to a thin polypropylene rope using copper

Table 13.3: Comparison of Data to Simulation for first 300 K measurement (Activation in Bq/mg/μA-s)

Foil position	Data	Original simulation	Contaminated moderator	Less D_2O	Beam hit collimator
h5	0.76 ± 0.13	0.869 ± 0.007	1.67 ± 0.08	1.52 ± 0.08	1.88 ± 0.22
h4	0.80 ± 0.13	0.934 ± 0.006	0.92 ± 0.06	0.96 ± 0.06	1.13 ± 0.10
m5	1.62 ± 0.27	1.656 ± 0.007	3.59 ± 0.22	3.28 ± 0.16	3.64 ± 0.17
m4	1.10 ± 0.19	1.359 ± 0.006	1.37 ± 0.04	1.39 ± 0.07	1.43 ± 0.06
m3	1.37 ± 0.23	1.148 ± 0.009	1.16 ± 0.14	0.99 ± 0.05	1.08 ± 0.09
m2	0.71 ± 0.12	0.393 ± 0.005	0.64 ± 0.17	0.54 ± 0.09	0.51 ± 0.04
m1	0.93 ± 0.16	0.357 ± 0.004	0.60 ± 0.10	0.44 ± 0.56	0.42 ± 0.03
l5	1.58 ± 0.27	6.130 ± 0.012	9.86 ± 0.27	9.39 ± 0.23	9.80 ± 0.20
l4	1.51 ± 0.25	2.941 ± 0.008	3.11 ± 0.05	3.26 ± 0.07	3.24 ± 0.08
l3	1.09 ± 0.18	2.475 ± 0.007	1.84 ± 0.06	1.77 ± 0.05	1.88 ± 0.05
l2	0.92 ± 0.16	0.714 ± 0.010	0.66 ± 0.03	0.72 ± 0.04	0.76 ± 0.02
l1	0.66 ± 0.11	0.736 ± 0.005	0.65 ± 0.02	0.61 ± 0.05	0.67 ± 0.02
χ^2		404	1034	1230	1164

Table 13.4: Comparison of Data to Simulation for second 300 K measurement (Activation in Bq/mg/μA-s)

Foil position	Data	Original simulation	Contaminated moderator	Less D_2O	Beam hit collimator
h5	0.53 ± 0.08	0.869 ± 0.007	1.67 ± 0.08	1.52 ± 0.08	1.88 ± 0.22
h4	0.70 ± 0.11	0.934 ± 0.006	0.92 ± 0.06	0.96 ± 0.06	1.13 ± 0.10
m5	1.33 ± 0.21	1.577 ± 0.010	1.67 ± 0.07	1.72 ± 0.09	1.72 ± 0.11
m4	0.88 ± 0.14	1.286 ± 0.001	1.13 ± 0.19	0.82 ± 0.04	0.85 ± 0.03
m3	1.21 ± 0.19	1.056 ± 0.006	0.61 ± 0.04	0.61 ± 0.04	0.63 ± 0.05
m2	0.35 ± 0.05	0.358 ± 0.008	0.22 ± 0.02	0.25 ± 0.03	0.28 ± 0.02
m1	0.66 ± 0.10	0.322 ± 0.006	0.18 ± 0.01	0.23 ± 0.04	0.27 ± 0.04
l5	1.35 ± 0.21	6.206 ± 0.011	13.57 ± 0.31	13.68 ± 0.32	13.78 ± 0.62
l4	0.59 ± 0.09	3.001 ± 0.008	4.33 ± 0.08	4.83 ± 0.19	4.16 ± 0.04
l3	0.90 ± 0.14	2.539 ± 0.007	2.66 ± 0.08	3.43 ± 0.47	2.85 ± 0.08
l2	0.66 ± 0.10	0.734 ± 0.007	1.18 ± 0.09	1.42 ± 0.07	1.44 ± 0.13
l1	0.65 ± 0.10	0.778 ± 0.006	1.05 ± 0.06	1.24 ± 0.06	1.35 ± 0.09
χ^2		1392	5411	6107	5552

wire. These materials were not put in the simulation under the assumption that these materials are small enough to be negligible. The pipes were also made of Al. Simpler simulations were done using plastic or Al pipes or cores, but no boats. Large amounts of plastic thermalize neutrons, but as long as the amount of plastic was small, the effect due to this plastic is negligible. The Al boats were not included in the simulation, but the Al pipes were. The effect of Al boats was measured using the TNF, as described in the next section.

When wrapping the Au and the Cd around the boats for irradiations, the foils did not wrap into perfect cylinders. Some foils were larger and became crinkled at the edges. When using Cd covers, it was possible for the Cd to shift a little bit to expose a mm of Au. These effects were not added to the simulations, although a slight exposure of Au could result in slightly higher than expected activations for Cd-covered foils.

Finally, the simulation made one assumption that did not occur at every irradiation measurement: a stable, focused proton beam. There was a large learning curve to steering the proton beam and difficulties in maintaining constant intensity. In addition, different tuning of the beam could cause additional or reduced irradiation that was not accounted for in the simulation. Every irradiation had a unique proton beam as discussed in Section 12.1.2. As the simulation adjustment for the proton beam shows above, a differing proton beam affects the behavior of the thermal neutron flux. If the irradiating beam is not stable enough, the calculated flux will not match measurement and needs to be removed from analysis in order to make conclusions about the agreement between measurement and simulation. Substantial proton beam drift was noted in the later irradiation runs (Runs 5-11) which included both 300 K runs (Runs 9 and 10), but not the 87 K run (Run 2). A large mis-steering of the proton beam can even change the activation pattern behavior. How this can happen is discussed in Section 13.12.

13.11 Aluminum effects on foil activation measurement at TNF

In the initial TNF measurements, the foils were place flat against the thermal neutron flux. However, in the thermal neutron flux tests with TUCAN, the Au foils were wrapped around Al boats. In order to determine possible geometric effects and other systematic effects in activation due to the Au foils being wrapped in a cylindrical Al boat, more tests were conducted at the TNF. For a review on the TNF and the initial measurements there, please see Section 10.3.

13.11.1 Method

In order to study the geometric effects of activating foils in both flat and cylindrical configurations used in the TUCAN tests, more activation tests were done at the TNF by placing the Au foils in different configurations. All of the Au foils were approximately $10 \times 20 \times 0.1$ mm and weighed within an accuracy of ± 1 mg. The combination of geometries of the foils tested included combinations of a foil rolled into an Al boat, a foil rolled onto a cylinder and placed inside an Al pipe and the original flat foil configuration. Each configuration included both a bare Au foil and Cd-covered foil measurement. A summary of the different foil configurations tested in the TNF neutron flux is given in Table 13.5. A photograph of all the samples activated on the TNF plate is shown in Figure 13.8.

Table 13.5: Sample arrangement for TNF irradiation

Gold sample	Weight (mg)	Configuration
A	354 ± 1	Bare flat foil
B	349 ± 1	Cd covered flat foil
C	351 ± 1	Bare foil in boat
D	343 ± 1	Cd covered foil in boat
E	351 ± 1	Bare foil on Al rod
F	358 ± 1	Cd covered foil on Al rod
G22	356 ± 1	Bare foil on Al rod in pipe
G24	386 ± 1	Bare foil on Al rod in pipe
H	380 ± 1	Cd covered (both sides) flat foil

The samples were irradiated for 12.5 hours with the BL1A proton beam current at 102 μA on

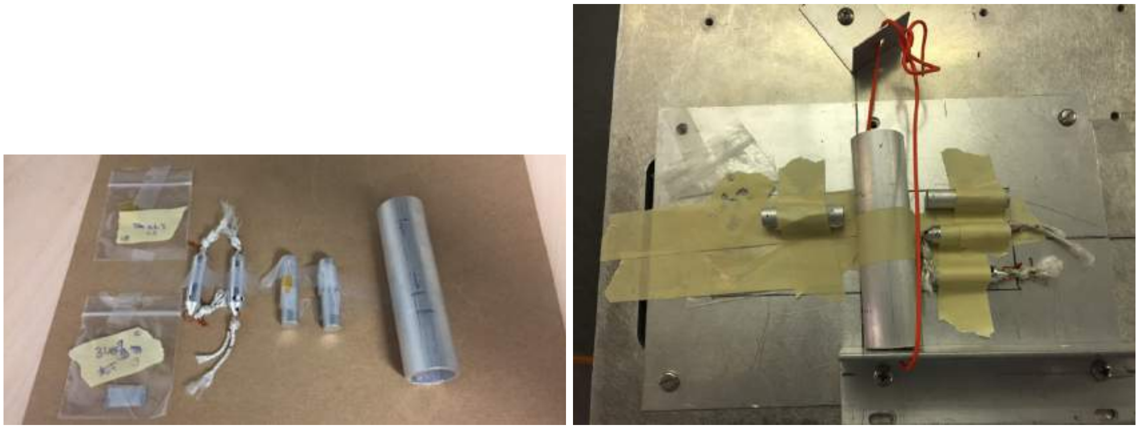

Figure 13.8: The photograph on the left shows the different samples that were irradiated in the tests (top left is a bare flat foil, below that is a Cd covered foil, then from left to right is a gold foil in an Al boat, Cd covered gold foil in an Al boat, gold foil on an Al bar, Cd covered gold foil on an Al bar, and finally inside the Al pipe there is a bare foil on Al rod, and s Cd covered foil on an Al rod. The panel on the right shows the arrangement of these samples on the TNF sample holder. The black rectangle in pen on the Al irradiation plate is the region of uniform neutron flux.

the night of August 22, 2017. The γ ray spectra were then measured over the next few days using the two HPGe detectors in the TRIUMF health sciences lab.

13.11.2 Results

The γ ray activation of the foils was measured in the HPGe detectors using GENIE. The analysis chosen for this test was called the A1 interference corrected analysis, which reported the activity in Bq according to the single 411 keV peak ($A1_{411}$), or for all of the ^{198}Au related peaks in the spectrum ($A1_{cor}$). To check the performance of this algorithm, the total counts in the 411 keV peak without background subtraction were also recorded. Activation data was collected for 600 s of live time and had an estimated background at a maximum of 100 counts in 10,000 (1%). The measurement results are summarized in Table 13.6.

Table 13.6: Gamma-ray counts from the decay of the activated gold samples, measured with the HPGe gamma-ray detectors in the TRIUMF health sciences lab. The sample irradiation ended at 10:30 am (± 5 minutes) on Aug. 23, 2017. In this table, t represents the HPGe detector live time, and N represents the counts in the 411 keV peak, including backgrounds.

Sample	Detector	Start Measurement	t(s)	N	$A1_{cor}$ (Bq)	$A1_{411}$ (Bq)
A	1	2017/08/23 15:55	600	427438	15690.0 ± 18.0	20280.0 ± 29.0
C	1	2017/08/23 16:15	600	350237	15220.0 ± 17.0	16690.0 ± 24.0
E	1	2017/08/23 16:32	600	386571	15690.0 ± 17.0	18460.0 ± 27.0
G24	1	2017/08/23 17:07	600	391467	14900.0 ± 17.0	18820.0 ± 27.0
G24	1	2017/08/23 17:39	600	392627	18410.0 ± 24.0	18860.0 ± 27.0
G22	2	2017/08/23 17:38	600	382023	19690.0 ± 26.0	20110.0 ± 29.0
B	1	2017/08/23 17:55	600	233651	8560.0 ± 10.0	11340.0 ± 29.0
D	2	2017/08/23 17:55	600	126674	4360.0 ± 6.0	6290.0 ± 9.0
H	2	2017/08/23 18:12	600	177138	9180.0 ± 10.0	9380.0 ± 14.0
F	1	2017/08/23 18:12	600	210838	10100.0 ± 14.0	10260.0 ± 15.0
A	1	2017/08/24 13:01	900	528170	21670.0 ± 25.0	20990.0 ± 35.0
A	1	2017/08/24 13:31	900	525645	21900.0 ± 25.0	21000.0 ± 30.0
C	1	2017/08/24 13:57	900	413300	17680.0 ± 21.0	16560.0 ± 24.0
C	1	2017/08/24 14:21	900	412124	17430.0 ± 20.0	16670.0 ± 24.0
A	2	2017/08/25 10:39	900	390979	20640.0 ± 26.0	21320.0 ± 31.0
A	2	2017/08/25 11:32	900	386751	20640.0 ± 26.0	21280.0 ± 21.0
C	2	2017/08/25 11:09	900	312777	16050.0 ± 21.0	17140.0 ± 25.0
C	2	2017/08/25 11:52	900	290182	15210.0 ± 20.0	16030.0 ± 23.0
A	2	2017/08/29 10:50	3600	588870	20105.0 ± 24.9	21407.0 ± 31.6
C	2	2017/08/29 12:19	3600	464012	14546.0 ± 19.1	17139.7 ± 25.1

13.11.3 Discussion of GENIE analysis compared to simple activation calculation

To check the black-box activation analysis, samples A and C were measured several times over the course of two decay lifetimes, to compare the activity calculated from the raw counts and the activities reported by the A1 analysis. The activity, A, was calculated the same as in Section 12.2.1 but without the current normalization, as all samples were exposed to the same neutron flux:

$$A = \frac{N}{\epsilon \cdot t \cdot \exp\left(-t_{dec}/\tau_{Au}\right)}, \tag{13.1}$$

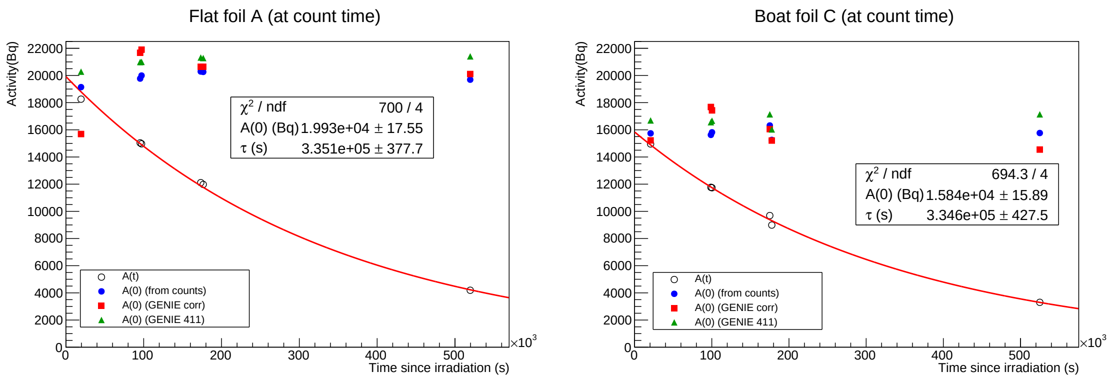

Figure 13.9: The left panel shows the activity measurements from foil A (flat gold foil), and the right panel shows the activity measurements from foil C (flat foil with Cd cover). In both figures, the open circles show the activity at measurement time from the bare counts measurement, the filled blue circles show the activity from the bare counts measurement projected back to the end of the time of irradiation of the foil, the red squares show the activity reported by the A1 analysis, and the green squares are from the A1 analysis on the 411 keV peak.

where t is the HPGe detector live time, ϵ is the detector efficiency for the specified HPGe calibration, τ_{Au} is the ^{198}Au lifetime, and t_{dec} is the time since irradiation that the sample has been decaying. The calculated activation is shown compared to the A1 analysis in Fig. 13.9 for foils A and C.

From this comparison, one can see that there is some effect from not subtracting backgrounds, since the estimated activity from the counts sees a slight, upward trend between the first and second measurement points in both foil A and C. In either case, the measurements from the raw counts seem to level off and are more consistent with each other from times 100,000 s after irradiation than the values reported by the A1 analysis. The A1 analysis, using all the peaks, shows the most variability, reporting values between 12,000 Bq and 22,000 Bq for foil A, and 15,000 Bq and 18,000 Bq for foil C. This analysis thus incurs a systematic uncertainty of $4000/20000 \times 100 = 20\%$. Looking at the 411 keV peak only, the results are more consistent with each other and with the results of the simple activation calculation. Using the values obtained from the A1 analysis using only the 411 keV peak incurs a systematic uncertainty of 10% due to the effects of background subtraction.

A simple fit for the decay lifetime yields $(3.351\pm0.038)\times10^5$ s for foil A, and $(3.346\pm0.043)\times10^5$ s

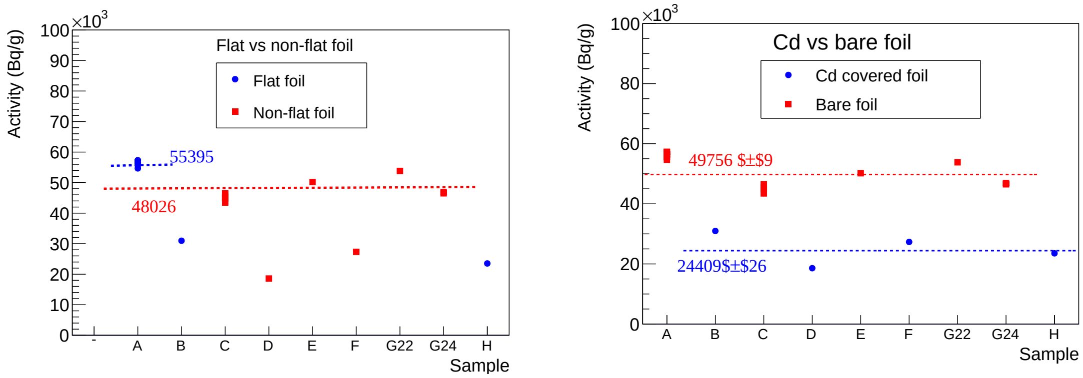

Figure 13.10: The left panel shows the specific activity measurements from foils that are flat as blue circles, and from the foils that are non-flat as red squares. In this figure, samples B, D, and F were all Cd covered samples, and were omitted from the average measurement shown as dashed lines. The right panel shows the specific activity measurements from the bare foils as red squares, and from Cd-covered foils as blue circles.

for foil C. These results are consistent with the current best estimate of $\tau_{Au} = (3.3589 \pm 0.0006) \times 10^5$ s from the Nuclear Data Sheets[101]. This suggests the estimated activities using the simple counting method are reliable.

13.11.4 Discussion of systematic uncertainty due to foil geometry

The main systematic uncertainty to be measured in these tests was in the foil geometry. In order to evaluate this uncertainty, the activities of the cylindrical foil on the Al boat must be compared to the flat foil configuration. The specific activities for the foils, flat versus cylindrical and with and without Cd, are shown in Fig. 13.10. In these comparisons, the specific activities are reported per gram of gold (Bq/g), using the calculations from the simple counts in the 411 keV peaks from Section 13.11.3.

From these measurements, one can see that the specific activity of the bare gold foils was $(49.756 \pm 0.009) \times 10^6$ Bq/g, and the Cd-covered foils is $(24.409 \pm 0.026) \times 10^6$ Bq/g. Recalling that the Cd-covered samples measure the activation from epithermal-and higher energy neutrons, while the bare foils measure the activation from all neutrons, the difference between the two gives the activation from thermal and colder neutrons, which according to these measurements was $(25.347 \pm 0.028) \times 10^6$ Bq/g.

The bare flat-foils had an average specific activity of $(55.40 \pm 0.23) \times 10^6$ Bq/g, while for the bare Cd-covered-foils, the specific activity was $(48.03 \pm 0.22) \times 10^6$ Bq/g. The specific activity of the non-flat foils is therefore systematically lower by $(7.37 \pm 0.33) \times 10^6$ Bq/g. This represents a difference of $7.4/50 \times 100\% = 14.8 \pm 0.6\%$. This difference is presumably due to the self-shielding of the gold foils, due to being relatively thick (0.1 mm).

13.11.5 Conclusion

A comparison of flat gold foils, and foils cylindrically wrapped around an Al rod showed that their activation in a neutron flux differed by about 15%. The cylindrically wrapped foils were activated by $14.8 \pm 0.6\%$ less than the flat foils. In addition, the systematic uncertainty due to background subtraction in the black box analysis of the GENIE software was estimated to be 10% when using only the 411 keV peak, and 20% when using the analysis of all peaks.

13.12 Irradiation to irradiation comparison

As noted in Section 12.1.2, different irradiation runs had unique proton beam behavior. Whether this unique behavior could affect the foil activations depended on the quality of the beam (what portion of the beam hit the tungsten target and not something else) and comparing the variation of beam to irradiation runs with the same temperature and settings.

13.12.1 BL1U steering

After the irradiations, an experimental report was drafted outlining the proton beam steering and related activities [102]. The beam tuning was checked using the HARP0 and HARP2 sensors from EPICS, the beam control system at TRIUMF. The HARPs use wires to measure x-y projections of the proton beam. A screenshot of the HARP2 output was taken for each measurement. The beam profile was noted to be Gaussian in the center with non-Gaussian “wings”. The beam tune settings were checked and recorded for each irradiation. The settings were not the same for every irradiation.

Runs 1-4 are noted to be stable, with acceptable increases in temperature in the target. However, there was not a close agreement between the 87 K irradiation and simulation.

Before the second irradiation with foils (87 K with D_2O), some beam tuning difficulties occurred and caused a spill into BSM56. Tuning difficulties were noted, until it was realized that the HARP0 was still inserted and scattering protons. Removing the HARP0 corrected the beam tune. While the subsequent irradiation was slowly ramped up, no other major issues were noted.

During Run 5, a decrease in the 1VB1 sensor was noted. 1VB1 is one of the magnet currents for steering the beam. The run was stopped, but then the magnet current returned. A temperature increase in the thermocouple was noted showing that the beam had hit the thermocouple. The beam was reset, and the irradiation then finished.

Run 6 showed an increase of about 2 degrees in temperature in the collimator as well, but the beam tune looked okay. After this, the intensity of the beam was lowered. The beam tune looked ok for these runs, but the possibility of the beam hitting the collimator remained.

There were difficulties steering the beam and not hitting the collimator. This was noted from Run 5 on. This could affect the resulting neutron flux, which made it difficult to simulate. If that is the case, the measured activation would vary between irradiations, regardless of whether the other settings are the same or not. Unfortunately, in this experiment, there were limited means to measure how much the beam may have drifted from the original settings. Run 5 had data showing the 1VB1 sensor with a sudden decrease in current, but the current came back as soon as the run was stopped.

The 1VB1 moved the beam horizontally. The HARP2 showed the x and y projections of the beam current, in terms of wire positions. The beam was usually centered around the wire position 7 or 8. However, the HARP2 showed a drift in the center of the beam to the left of wire position 5. There was noted evidence of similar horizontal drifts in subsequent runs, but how much was not always clear, due to factors such as uncorrelated beam spills and drops in 1VB1. There was

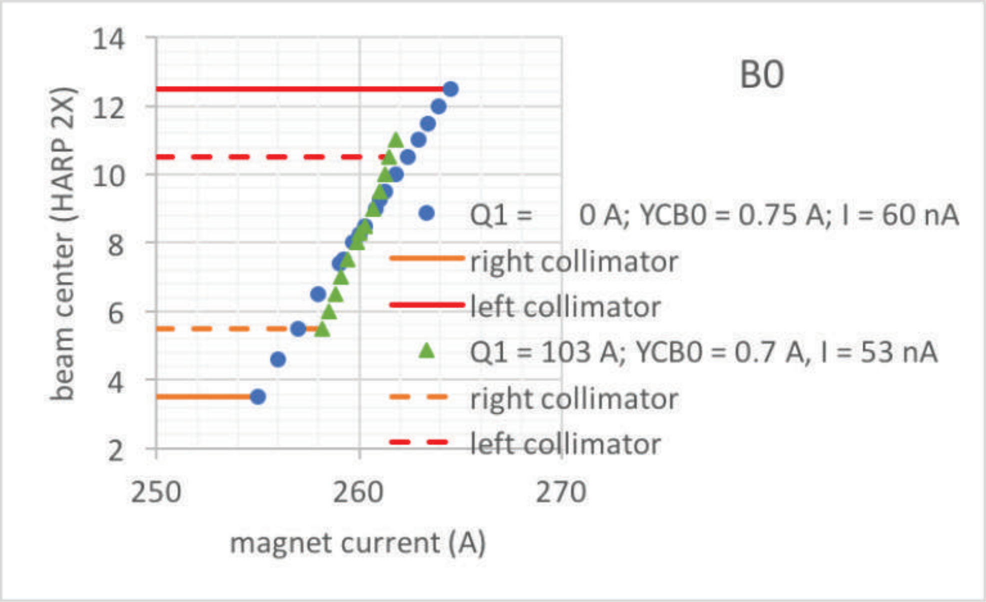

Figure 13.11: Figure of the noted temperature increases using different beam settings. The beam was slowly shift in the horizontal direction and stopped when the collimator temperature increased. The horizontal lines indicate where the collimator temperature increase for the different beam settings: solid line for Q1=0A and dashed line for Q1=103A. Q1 is the beam focusing setting. Figure from [102].

an automatic steering algorithm for BL1A, but that turned off at currents below 20 μA, which permitted drifts at lower currents. All of the irradiation runs were at lower currents. However, the collimator temperature was always available.

In order to determine how to gauge the amount of beam mis-steering results in increases in collimator temperature, some tests were performed with different beam focuses (Q1 setting) and gradually shifting the beam position horizontally, while watching the collimator temperature. At lower Q1, the beam veered off center to about wire position 3 or 13 before temperature increased. At higher Q1, the beam veered off center to about wire position 5.5 or 10.5 before the collimator temperature increased. The noted behavior may be seen in Figure 13.11.

13.12.2 8 K data comparison

Three irradiation runs were taken with the cryostat temperature at 8 K, runs 3, 5, and 7. Due to concerns about the beam problems occurring in Run 5, the same foil settings were used for Run 7

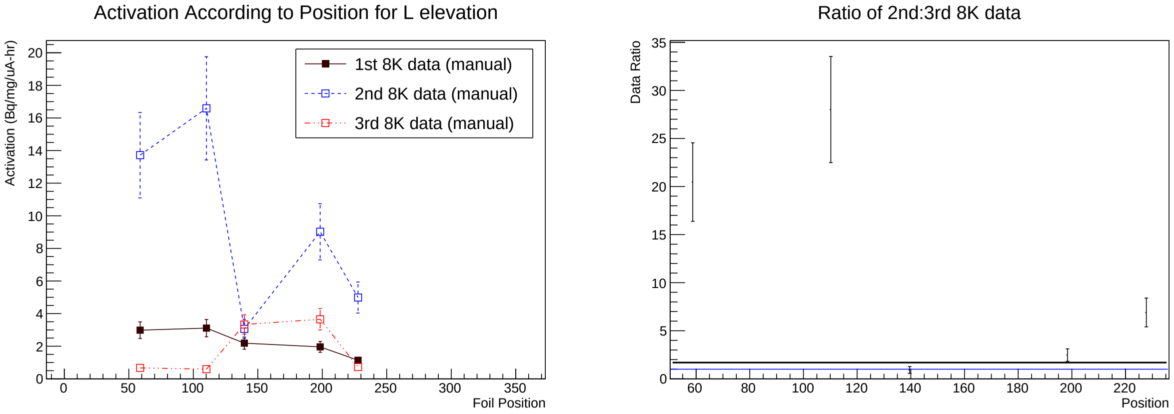

Figure 13.12: To the left is the measured activation of the foils for all three 8 K runs (Irradiation Runs 3, 5 and 7). The first measurement used Cd-covers and the other two used bare foils. To the right is the ratio of the 2nd measurement over the 3rd measurement.

as Run 5. This gives an opportunity to compare data variation between irradiation runs. All three of the 8 K runs were compared. Every irradiation run had two bare foils in the top positions, H5 and H4. This was done to allow for normalization and run to run comparisons. These top positions were the most useful for gauging the variation in neutron flux from one run to another. Runs 5 and 7 had the same settings, so the other positions may be compared to determine how much the activation may vary depending on the beam conditions.

8 K measurement - lowest level

In the lowest level, the first measurement had Cd-covers and the other two measurements used bare foils, as shown in Figure 13.12. Only the bare foil in position L3 agrees between the 2nd and 3rd measurements. The difference between the second and third measurements reached about 28 times higher activation for the second measurement over the third measurement. A number of the Cd-covered foils were also more activated than some of the bare foils in the 3rd measurement which was not at all expected to occur. The activation pattern for the second measurement was also inverted, the foils outside the graphite were the peaks and the foils close to the graphite were the valleys.

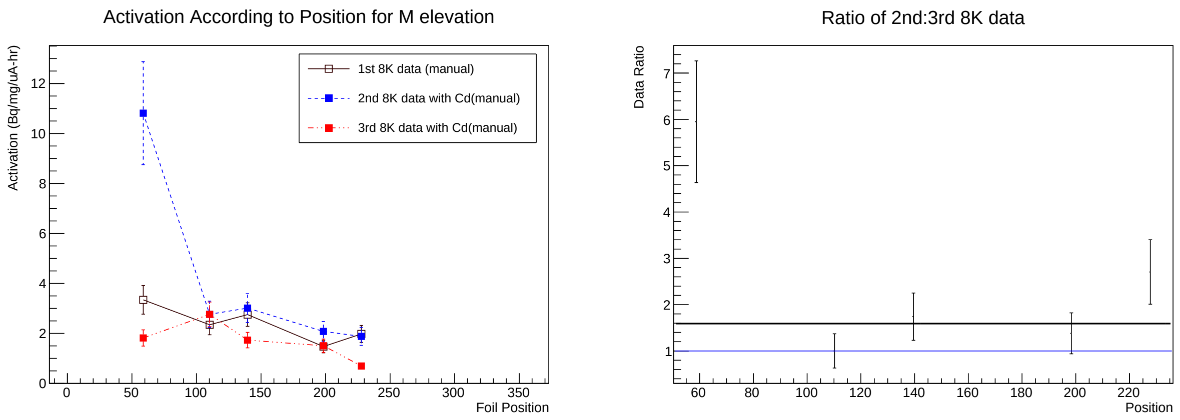

Figure 13.13: To the left is the measured activation of the foils for all three 8 K runs (Irradiation Runs 3, 5 and 7). The first measurement used bare foils and the other two used Cd-covers.

8 K measurement - middle level

In the middle level, the first measurement used bare foils, while the other two measurements used Cd-covers, as shown in Figure 13.13. Only one position in the 2nd and 3rd measurements agreed, M4. M2 doesn't quite agree. Also, all of the Cd-covered foils in the 2nd measurement had higher activation than the bare foils in the 1st measurement. One of the Cd-covered foils in the 3rd measurement was still higher than the bare foil in the 1st measurement and another of the Cd-covered foils had the same activation as the bare foil in the 1st measurement. Again, this should not have occurred at all. The third measurement also had that inverted peak-and-valley pattern.

8 K measurement - highest level

At the highest level, all three measurements used bare foils as shown in Figure 13.14. Only one of the foil activation measurements agreed between the 1st and 3rd measurements (position H5). The second measurement was more than twice as high as the first measurement.

Comparison of measurements

All three of these measurements occurred at 8 K. Two of these measurements had the same foil settings, and all three had the same foil settings at the highest positions. There was more disagreement than agreement. Expected activation patterns did not always occur, either. The one known

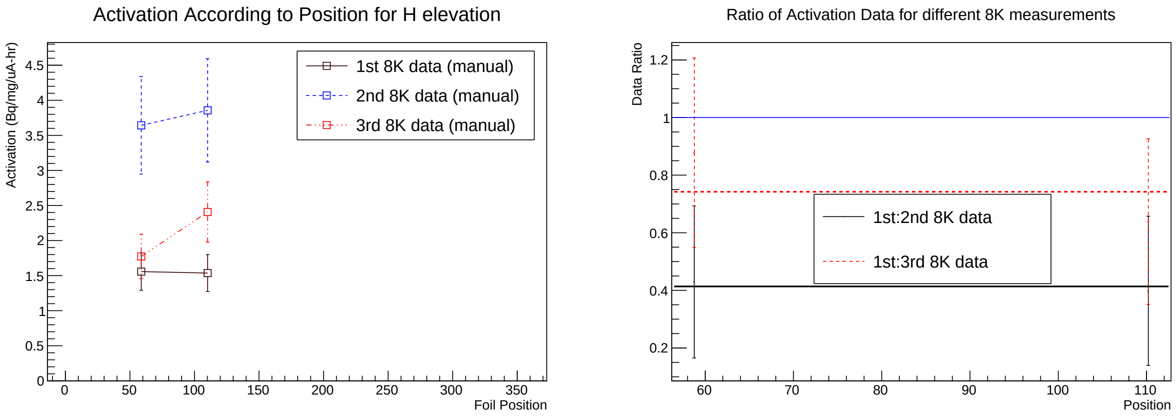

Figure 13.14: To the left is the measured activation of the foils for all three 8 K runs (Irradiation Runs 3, 5 and 7). All measurements used bare foils. To the right is the ratio of the 1st measurement over the 2nd and 3rd measurements.

variable to change between all these measurements is the variability of the proton beam.

13.12.3 Discussion of beam steering effects on activation

Regardless of whether the data was compared to simulation or measurements with identical settings, there appears to be a large discrepancy between activations. There was also a noted change in the expected activation behavior (reverse of expected peak-and-valley activation pattern) starting in irradiation run 5 with more runs where the foils at position L5 was substantially lower than expected. This is likely due to the different proton beams that occurred from irradiation to irradiation. Some of these irradiations were stable, some showed strong evidence of the proton beam hitting the collimator. This makes the data collected in Runs 5-11 less reliable. While Run 6 still appeared to be a stable run from the proton beam data, there was still evidence of the temperature of the collimator increasing by about 2 degrees.

Run 2 (87 K is shown in Figures 13.2, 13.3, and 13.4) was a stable run. This run had a number of data points that agreed with the simulation. The total agreement improved after adjusting the simulation settings, but still did not agree well: the χ^2 decreased from 4255 to 2287 with 12 degrees of freedom. The L5, M5, and H5 positions were all too high and disagreed with the model the most. One possibility for this is that the graphite column at the 5 position was in a slightly different position than assumed in the model. Thus, the foils in the 5 positions did not get exposed to the assumed level of moderation. The model without the graphite had the closest agreement with the 5 position, which also suggests possible misalignment.

13.13 Concluding remarks on the systematic uncertainties

While making adjustments to the simulations and checking the foil geometry improved agreement, these analyzes did not completely account for the differences between the data and simulation. However, there was a noted variation in the steering of the proton beam from irradiation to irradiation. Some of the beam hit the collimator. How much is not known. This, then, requires that most of the data runs be discarded, in particular, Runs 5-11. Run 6 looked more stable with smaller evidence of the beam hitting the collimator, so whether this run is to be discarded is debatable. Also, many of the discrepancies noted in the stable Run 2 (87 K) were due to the model for the graphite. The graphite model depended on libraries that assumed a perfect crystalline structure and a denser graphite. Even after adding amorphous carbon to better model the graphite, the structure of the graphite in the model was not close enough to the reactor grade graphite used in measurement. Some variation between graphite models and measurements have been noted in the past for this reason [99].

In short, the model has shown two main limitations in relating to the measurement as follows:

- Proton beam: The model assumed a well-focused, perfectly steered proton beam impinging squarely on the tungsten target. Since this measurement involved first tests of focusing and the steering the beam, variations from the model occurred. Steering of the beam has since become more consistent as the behavior of the beam has become better understood, but cannot be assumed for the thermal neutron measurement. As a result, there could be more beam spread than assumed, or the beam could also hit the collimator, thus drastically changing the assume neutron flux pattern. These variations are not easily calculated in the model.

- Moderator materials: The model assumed consistent moderation. More specifically, the structure of the graphite is assumed to be consistent when moderating neutrons. However, graphite includes a combination of crystalline and amorphous carbon and varies greatly in structure. The structure of the carbon determines the neutron thermalization. The average density of sample graphite blocks was used in the model. This variation in density, and thus structure of the carbon atoms, restricts how closely the model may be able to match measurement.

Out of the systematic effects discussed, the steering of the proton beam had the largest effect. Adding wood or angling the L5 foil in the simulation had negligible effect. Unfortunately, records of the beam mis-steering off the tungsten target came only from temperature measurements around the collimator, and are not well modelled in the simulation. From the 8 K measurements, the steering of the beam affected the activation by more than an order of magnitude, completely covering the discrepancies between noted simulation and activation. However, this also means that conclusions cannot be made on the amount of thermal and colder neutron flux generated with any precision less than a factor of 2 to an order of magnitude, depending on the position.

Part IV

Conclusions

Chapter 14

Conclusions

This thesis chronicled the measurement of a prototype UCN detector at PSI, and thermal neutron measurements outside of the horizontal UCN source.

The UCN detector for TUCAN was characterized with two UCN beamports at PSI, and compared to a commercial Cascade detector. When the data was compared to simulation, the neutron PSD cut efficiency was determined to be 99.5 ± 0.5 % and the background contamination was determined to be 0.3 ± 0.1 %. The total efficiency of the ^{6}Li detector was determined to be $89.7^{+1.3}_{-1.9}$ %. This detector was determined to be as efficient as the Cascade detector.

Some future developments for the detection system include construction improvements to reduce backgrounds. The detection system for phase 2 of the measurement includes building four detectors to count the UCN of both spins simultaneously.

The thermal neutron measurement involved using Au and Cd foils to determine the thermal and colder neutron flux at specified positions around the cryostat. The positions were determined using a FLUKA model of the experimental hall. These positions were chosen to determine the effectiveness of the moderators, including the presence or absence of the graphite reflectors. There were several inconsistencies between the data and the model. A few inconsistencies were addressed by checking the real position of the lower foils, removing the graphite reflectors in the simulation and moving the simulated proton beam further upstream of the proton beam pipe. The position of the lower foils was lower than originally assumed. The graphite was present in the measurement, but of a different structure than the model. Finally, the proton beam was not as stable as assumed.

Since the absence of the graphite and backing of the origin of the proton beam improved agreement, more simulations were done to better understand the experimental set-up. For the proton beam, some noted drift occurred during irradiation Run 5. This suggests that the proton beam had variability that was not calculated. Looking at the detailed summary of the steering of the proton beam shows substantial evidence of the beam hitting the collimator in later runs. This would require removing Runs 5-11 from the analysis. Run 2, which was a stable run, had more agreement with simulation. If this run is typical in ideal beam conditions, then the thermal neutron flux may be higher than simulated. While proton beam drift was noted for these runs, BL1A had a steering algorithm for higher currents, which prevented the drifts noted in these irradiations from 2016. The proton beam was started again in 2017 with less difficulty in steering. As for the graphite, both the graphite and the lead were assayed for potential contamination. While some contamination was found and added to the simulation, this was not enough to explain all of the activation differences. The graphite was noted to be reactor grade which has a lower thermal neutron cross section. Agreement between models and measurements of thermal neutron scattering in graphite is known to vary. Between the instability of the proton beam and the lighter than expected graphite, the thermal and colder neutron flux generated outside the cryostat could not be determined with precision.

Appendix A

Thermal neutron flux data

A.1 Measurement data tables

The following tables are the activations measured for the thermal neutron activation measurement. The activations were calculated using the GENIE program and the manual analysis.

Table A.1: Run 1 - 126 K (activation in Bq/mg/μA-s)

Foil position	Foil label	Calibration	GENIE Activation	Manual Activation
H5	4	sfilter	0.658 ± 0.009	1.67 ± 0.32
H4	16	sfilter	0.689 ± 0.009	1.74 ± 0.33
M5	15	pole(0.5m)	1.098 ± 0.019	3.30 ± 0.53
M4	36	pole(0.5m)	0.780 ± 0.012	2.27 ± 0.37
M3	13	pole(0.5m)	0.892 ± 0.012	2.75 ± 0.45
M2	31	sfilter	0.739 ± 0.009	1.87 ± 0.35
M1	33	sfilter	0.852 ± 0.009	2.16 ± 0.41
L5	9	pole(0.5m)	1.145 ± 0.019	3.47 ± 0.56
L4	27	pole(0.5m)	1.142 ± 0.019	3.59 ± 0.59
L3	5	sfilter	0.920 ± 0.009	2.31 ± 0.44
L2	32	sfilter	0.774 ± 0.009	1.97 ± 0.37
L1	39	sfilter	0.306 ± 0.003	1.17 ± 0.22

Table A.2: Run 2 - 87 K (activation in Bq/mg/μA-s)

Foil position	Foil label	Calibration	GENIE Activation	Manual Activation
H5	7	sfilter	0.549 ± 0.058	0.67 ± 0.13
H4	18	sfilter	0.510 ± 0.054	0.69 ± 0.13
M5	14	pole(0.5m)	0.895 ± 0.094	1.35 ± 0.22
M4	24	sfilter	0.735 ± 0.077	0.85 ± 0.16
M3	1	pole(0.5m)	0.730 ± 0.077	0.90 ± 0.15
M2	2	sfilter	0.590 ± 0.062	0.78 ± 0.15
M1	22	sfilter	0.587 ± 0.062	0.68 ± 0.13
L5	23	pole(0.5m)	0.936 ± 0.098	1.18 ± 0.19
L4	17	pole(0.5m)	0.963 ± 0.101	1.18 ± 0.19
L3	8	pole(0.5m)	0.661 ± 0.069	0.84 ± 0.14
L2	28	sfilter (9.97% deadtime)	0.692 ± 0.073	0.83 ± 0.16
L1	10	sfilter	0.351 ± 0.037	0.36 ± 0.07

Table A.3: Run 3 - 8 K (activation in Bq/mg/μA-s)

Foil position	Foil label	Calibration	GENIE Activation	Manual Activation
H5	47	sfilter	0.626 ± 0.007	1.55 ± 0.29
H4	38	sfilter	0.634 ± 0.007	1.53 ± 0.29
M5	40	sfilter	1.384 ± 0.015	3.33 ± 0.63
M4	43	sfilter	1.038 ± 0.011	2.34 ± 0.44
M3	39	sfilter	1.227 ± 0.015	2.74 ± 0.52
M2	36	sfilter	0.652 ± 0.007	1.47 ± 0.28
M1	41	sfilter	0.881 ± 0.011	1.97 ± 0.37
L5	44	sfilter	1.333 ± 0.015	2.97 ± 0.56
L4	45	sfilter	1.366 ± 0.015	3.10 ± 0.59
L3	46	sfilter	0.951 ± 0.011	2.18 ± 0.41
L2	37	sfilter	0.867 ± 0.011	1.95 ± 0.37
L1	42	sfilter	0.495 ± 0.007	1.13 ± 0.21

Table A.4: Run 4 - 35 K (activation in Bq/mg/μA-s)

Foil position	Foil label	Calibration	GENIE Activation	Manual Activation
H5	5	sfilter	0.671 ± 0.007	1.44 ± 0.27
H4	4	sfilter	0.738 ± 0.010	1.42 ± 0.27
M5	11	sfilter	1.704 ± 0.020	1.57 ± 0.30
M4	35	sfilter	1.223 ± 0.013	2.37 ± 0.45
M3	19	sfilter	1.435 ± 0.017	1.31 ± 0.25
M2	12	sfilter	0.831 ± 0.010	1.61 ± 0.30
M1	9	sfilter	0.621 ± 0.007	1.33 ± 0.25
L5	6	sfilter	1.565 ± 0.020	1.45 ± 0.28
L4	25	sfilter	0.880 ± 0.010	1.76 ± 0.33
L3	20	sfilter	0.950 ± 0.010	1.81 ± 0.34
L2	34	sfilter	0.907 ± 0.01	1.74 ± 0.33
L1	30	sfilter	0.651 ± 0.007	1.28 ± 0.24

Table A.5: Run 5 - 8 K (activation in Bq/mg/μA-s)

Foil position	Foil label	Calibration	GENIE Activation	Manual Activation
H5	33	sfilter(2)	0.176 ± 0.003	3.84 ± 0.73
H4	32	sfilter(2)	0.207 ± 0.003	4.04 ± 0.76
M5	13	sfilter(2)	0.618 ± 0.006	11.08 ± 2.09
M4	36	sfilter(2)	0.134 ± 0.015	2.96 ± 0.56
M3	16	sfilter(1)	0.570 ± 0.009	3.18 ± 0.60
M2	27	sfilter(1)	0.378 ± 0.006	2.38 ± 0.45
M1	5	sfilter(1)	0.337 ± 0.006	2.09 ± 0.39
L5	9	sfilter(2)	0.816 ± 0.009	14.05 ± 2.66
L4	4	sfilter(1)	3.283 ± 0.031	16.82 ± 3.18
L3	15	sfilter(2)	0.122 ± 0.002	3.34 ± 0.63
L2	39	sfilter(1)	1.756 ± 0.022	9.17 ± 1.73
L1	31	sfilter(2)	0.272 ± 0.003	5.16 ± 0.98

Table A.6: Run 6 - 65 K (activation in Bq/mg/μA-s)

Foil position	Foil label	Calibration	GENIE Activation	Manual Activation
H5	14	sfilter	0.727 ± 0.011	11.8 ± 2.2
H4	2	sfilter(2)	0.710 ± 0.009	10.9 ± 2.1
M5	8	sfilter(1)	1.581 ± 0.020	24.4 ± 4.6
M4	28	sfilter(1)	1.113 ± 0.014	17.6 ± 3.3
M3	22	sfilter(2)	1.18 ± 0.014	20.0 ± 3.8
M2	23	sfilter	0.771 ± 0.011	13.6 ± 2.6
M1	7	sfilter(2)	0.871 ± 0.011	13.9 ± 2.6
L5	10	sfilter(2)	1.542 ± 0.020	23.7 ± 4.5
L4	1	sfilter(1)	1.476 ± 0.020	22.8 ± 4.3
L3	17	sfilter(2)	1.051 ± 0.014	16.7 ± 3.1
L2	18	sfilter(1)	0.83 ± 0.011	12.8 ± 2.4
L1	24	sfilter(1)	0.497 ± 0.009	8.0 ± 1.5

Table A.7: Run 7 - 8 K (activation in Bq/mg/μA-s)

Foil position	Foil label	Calibration	GENIE Activation	Manual Activation
H5	40	sfilter(1)	0.563 ± 0.007	1.74 ± 0.33
H4	36	sfilter(1)	0.559 ± 0.007	1.84 ± 0.35
M5	46	sfilter(1)	1.681 ± 0.020	0.73 ± 0.14
M4	37	sfilter(1)	0.445 ± 0.007	0.66 ± 0.13
M3	41	sfilter	0.485 ± 0.007	1.49 ± 0.28
M2	44	sfilter(1)	0.234 ± 0.003	0.73 ± 0.14
M1	47	sfilter(1)	0.243 ± 0.003	0.73 ± 0.14
L5	42	sfilter(1)	2.276 ± 0.026	3.26 ± 0.62
L4	39	sfilter(1)	1.249 ± 0.016	3.56 ± 0.67
L3	45	sfilter(1)	2.575 ± 0.029	2.35 ± 0.45
L2	38	sfilter(1)	0.518 ± 0.007	1.75 ± 0.33
L1	43	sfilter	0.895 ± 0.010	2.72 ± 0.51

Table A.8: Run 8 - 49 K (activation in Bq/mg/μA-s)

Foil position	Foil label	Calibration	GENIE Activation	Manual Activation
H5	35	sfilter(1)	0.978 ± 0.014	1.62 ± 0.31
H4	5	sfilter(1)	0.872 ± 0.011	1.52 ± 0.29
M5	11	sfilter(2) (10.51%)	2.067 ± 0.025	3.29 ± 0.62
M4	9	sfilter(1)	1.405 ± 0.018	2.49 ± 0.47
M3	4	sfilter(2)	1.753 ± 0.021	2.80 ± 0.53
M2	6	sfilter(1)	1.052 ± 0.014	1.72 ± 0.32
M1	25	sfilter(1)	1.073 ± 0.011	1.87 ± 0.35
L5	30	sfilter(2)	1.889 ± 0.021	2.96 ± 0.56
L4	20	sfilter(2)	1.982 ± 0.025	3.14 ± 0.59
L3	34	sfilter(2)	1.294 ± 0.018	2.07 ± 0.39
L2	12	sfilter(1)	0.994 ± 0.014	1.61 ± 0.30
L1	19	sfilter(2)	0.662 ± 0.011	1.12 ± 0.21

Table A.9: Run 9 - 300 K (activation in Bq/mg/μA-s)

Foil position	Foil label	Calibration	GENIE Activation	Manual Activation
H5	39	sfilter(2)	0.569 ± 0.007	0.83 ± 0.16
H4	31	sfilter(2)	0.622 ± 0.007	0.83 ± 0.16
M5	33	pole	0.988 ± 0.016	1.29 ± 0.21
M4	9	sfilter(2)	0.912 ± 0.010	1.12 ± 0.23
M3	36	sfilter(2)	1.075 ± 0.013	1.37 ± 0.26
M2	4	sfilter(2)	0.601 ± 0.007	0.86 ± 0.16
M1	15	sfilter(2)	0.716 ± 0.010	0.94 ± 0.18
L5	13	pole	0.99 ± 0.016	1.32 ± 0.22
L4	16	pole	0.931 ± 0.016	1.20 ± 0.20
L3	32	sfilter(2)	0.833 ± 0.010	1.10 ± 0.21
L2	27	sfilter(2)	0.706 ± 0.010	0.92 ± 0.17
L1	5	sfilter(2)	0.493 ± 0.007	0.66 ± 0.13

Table A.10: Run 10 - 300 K (activation in Bq/mg/μA-s)

Foil position	Foil label	Calibration	GENIE Activation	Manual Activation
H5	28	sfilter(2)	0.738 ± 0.01	0.94 ± 0.18
H4	14	sfilter(2)	0.752 ± 0.010	0.95 ± 0.18
M5	22	pole	1.162 ± 0.019	1.89 ± 0.31
M4	7	pole	0.825 ± 0.013	1.26 ± 0.20
M3	2	pole	0.977 ± 0.016	1.52 ± 0.25
M2	8	sfilter(2)	0.731 ± 0.010	0.93 ± 0.18
M1	17	sfilter(2) (10.31%)	0.813 ± 0.010	1.04 ± 0.20
L5	1	pole	1.256 ± 0.022	1.98 ± 0.32
L4	10	pole	0.742 ± 0.013	1.23 ± 0.20
L3	23	sfilter(2) (11.30%)	0.981 ± 0.013	1.18 ± 0.22
L2	18	sfilter(2)	0.747 ± 0.010	0.94 ± 0.18
L1	24	sfilter(2)	0.657 ± 0.010	0.81 ± 0.15

Table A.11: Run 11 - Empty (activation in Bq/mg/μA-s)

Foil position	Foil label	Calibration	GENIE Activation	Manual Activation
H5	45	sfilter	0.862 ± 0.011	0.9 ± 0.9
H4	40	sfilter	0.839 ± 0.011	0.8 ± 0.8
M5	46	sfilter	1.377 ± 0.014	1.1 ± 1.1
M4	42	sfilter	1.046 ± 0.013	9.5 ± 1.0
M3	41	sfilter	1.146 ± 0.014	10.9 ± 1.1
M2	43	sfilter	0.880 ± 0.012	9.5 ± 1.0
M1	36	sfilter	1.045 ± 0.013	14.0 ± 1.4
L5	47	sfilter	1.439 ± 0.017	5.1 ± 0.5
L4	44	sfilter	1.083 ± 0.015	8.8 ± 0.9
L3	38	sfilter	0.832 ± 0.013	9.4 ± 0.9
L2	37	sfilter	0.855 ± 0.012	10.7 ± 1.1
L1	39	sfilter	0.535 ± 0.007	13.4 ± 1.4

A.2 Simulation tables

The following tables are the activations calculated for the thermal neutron activation measurement. The activations were calculated using FLUKA. Adjustments to the simulation are also included.

Table A.12: Simulation - 87 K no Cd (activation in Bq/mg/μA-s)

foil position	Original simulation	Corrected foil placement	Added wood to foil L5	Angled foil L5	No graphite	Adjusted beam	No graphite and adjusted beam
H5	1.802 ± 0.012	2.361 ± 0.224	2.806 ± 0.278	2.467 ± 0.166	1.261 ± 0.052	2.07 ± 0.29	1.21 ± 0.03
H4	1.561 ± 0.010	1.290 ± 0.083	1.2 ± 0.061	1.174 ± 0.062	1.012 ± 0.055	1.05 ± 0.13	1.02 ± 0.15
M5	3.847 ± 0.017	4.781 ± 0.112	5.367 ± 0.392	4.919 ± 0.285	1.879 ± 0.096	4.33 ± 0.38	2.12 ± 0.41
M4	2.527 ± 0.015	1.866 ± 0.136	3.393 ± 1.290	1.873 ± 0.112	1.523 ± 0.083	1.82 ± 0.51	1.20 ± 0.02
M3	2.784 ± 0.017	1.433 ± 0.133	1.493 ± 0.198	1.280 ± 0.087	1.252 ± 0.075	1.00 ± 0.01	1.33 ± 0.12
M2	1.045 ± 0.012	0.626 ± 0.064	0.759 ± 0.118	0.812 ± 0.153	0.489 ± 0.040	1.00 ± 0.15	0.65 ± 0.05
M1	1.236 ± 0.013	0.927 ± 0.221	0.887 ± 0.144	0.819 ± 0.108	0.727 ± 0.120	0.45 ± 0.06	0.44 ± 0.04
L5	10.192 ± 0.018	15.521 ± 0.648	14.761 ± 0.297	15.081 ± 0.324	8.063 ± 0.277	13.78 ± 0.31	7.50 ± 0.78
L4	4.93 ± 0.016	4.607 ± 0.130	4.886 ± 0.108	4.662 ± 0.065	4.299 ± 0.123	4.67 ± 0.09	3.98 ± 0.03
L3	5.198 ± 0.016	3.113 ± 0.150	3.179 ± 0.164	2.848 ± 0.051	2.949 ± 0.115	3.07 ± 0.03	2.88 ± 0.18
L2	1.729 ± 0.012	1.253 ± 0.077	1.299 ± 0.097	1.374 ± 0.108	1.17 ± 0.036	1.46 ± 0.16	1.25 ± 0.16
L1	2.111 ± 0.012	1.079 ± 0.049	1.093 ± 0.073	1.416 ± 0.109	1.087 ± 0.12	1.88 ± 0.45	1.03 ± 0.03

Table A.13: Simulation - 87 K with Cd (activation in Bq/mg/μA-s)

foil position	Original simulation	Corrected foil placement	Added wood to foil L5	Angled foil L5	No graphite	Adjusted beam	No graphite and adjusted beam
H5	1.573 ± 0.011	1.092 ± 0.060	1.008 ± 0.054	0.918 ± 0.050	0.970 ± 0.046	0.848 ± 0.041	0.920 ± 0.111
H4	1.433 ± 0.010	0.826 ± 0.079	0.857 ± 0.092	1.075 ± 0.236	0.713 ± 0.040	0.737 ± 0.143	0.571 ± 0.003
M5	3.236 ± 0.015	2.049 ± 0.076	2.154 ± 0.184	1.907 ± 0.061	1.222 ± 0.048	1.608 ± 0.050	1.228 ± 0.046
M4	2.169 ± 0.014	1.086 ± 0.049	1.073 ± 0.031	1.103 ± 0.054	0.868 ± 0.036	1.057 ± 0.094	1.023 ± 0.148
M3	2.344 ± 0.019	0.731 ± 0.038	0.721 ± 0.035	0.744 ± 0.036	0.688 ± 0.036	0.610 ± 0.050	0.638 ± 0.091
M2	0.865 ± 0.011	0.286 ± 0.032	0.356 ± 0.039	0.342 ± 0.033	0.240 ± 0.025	0.314 ± 0.019	0.351 ± 0.018
M1	0.961 ± 0.012	0.235 ± 0.024	0.305 ± 0.037	0.284 ± 0.039	0.251 ± 0.046	0.239 ± 0.021	0.196 ± 0.036
L5	9.683 ± 0.019	10.754 ± 0.213	10.846 ± 0.296	10.165 ± 0.115	6.476 ± 0.176	9.877 ± 0.350	6.170 ± 0.643
L4	4.565 ± 0.017	3.701 ± 0.168	3.666 ± 0.076	3.471 ± 0.086	3.377 ± 0.079	3.465 ± 0.153	3.193 ± 0.080
L3	4.832 ± 0.016	2.132 ± 0.062	2.027 ± 0.042	2.045 ± 0.051	2.001 ± 0.057	2.067 ± 0.120	2.001 ± 0.064
L2	1.541 ± 0.016	0.732 ± 0.046	0.737 ± 0.033	0.724 ± 0.025	0.665 ± 0.034	0.751 ± 0.027	0.728 ± 0.024
L1	1.895 ± 0.011	0.576 ± 0.028	0.700 ± 0.048	0.664 ± 0.073	0.558 ± 0.016	0.610 ± 0.007	0.773 ± 0.074

Table A.14: Simulation - 300 K no Cd (activation in Bq/mg/μA-s)

foil placement number	Original simulation	Corrected foil placement	Added wood to foil L5	Angled foil L5	No graphite	Adjusted beam	No graphite and adjusted beam
H5	0.869 ± 0.007	2.249 ± 0.288	1.976 ± 0.164	1.988 ± 0.161	1.215 ± 0.053	1.970 ± 0.115	0.964 ± 0.106
H4	0.934 ± 0.006	1.189 ± 0.087	1.155 ± 0.075	1.186 ± 0.083	0.933 ± 0.057	1.010 ± 0.099	0.830 ± 0.014
M5	1.656 ± 0.007	4.305 ± 0.221	4.062 ± 0.179	5.147 ± 0.499	1.705 ± 0.037	4.226 ± 0.308	1.732 ± 0.326
M4	1.359 ± 0.006	1.638 ± 0.127	1.640 ± 0.113	1.627 ± 0.096	1.297 ± 0.033	1.395 ± 0.096	1.642 ± 0.408
M3	1.148 ± 0.009	1.168 ± 0.135	1.473 ± 0.143	1.190 ± 0.060	1.039 ± 0.074	1.111 ± 0.055	0.922 ± 0.098
M2	0.393 ± 0.005	0.613 ± 0.066	0.723 ± 0.091	0.501 ± 0.047	0.541 ± 0.051	0.454 ± 0.113	0.740 ± 0.084
M1	0.357 ± 0.004	0.522 ± 0.031	0.520 ± 0.059	0.480 ± 0.043	0.425 ± 0.041	0.570 ± 0.026	0.324 ± 0.100
L5	6.206 ± 0.011	14.652 ± 0.372	15.072 ± 0.289	15.505 ± 0.474	8.289 ± 0.239	12.832 ± 0.733	7.071 ± 0.128
L4	3.001 ± 0.008	4.765 ± 0.109	4.774 ± 0.089	4.681 ± 0.087	4.176 ± 0.073	4.669 ± 0.211	4.250 ± 0.073
L3	2.539 ± 0.007	3.077 ± 0.079	2.967 ± 0.058	3.054 ± 0.09	2.718 ± 0.061	2.725 ± 0.206	2.724 ± 0.074
L2	0.734 ± 0.007	1.285 ± 0.070	1.333 ± 0.086	1.298 ± 0.09	1.123 ± 0.040	1.280 ± 0.031	1.200 ± 0.034
L1	0.778 ± 0.006	1.149 ± 0.042	1.192 ± 0.075	1.462 ± 0.159	0.989 ± 0.049	1.355 ± 0.316	0.922 ± 0.094

Table A.15: Simulation - 300 K with Cd (activation in Bq/mg/μA-s)

foil placement number	Original simulation	Corrected foil placement	Added wood to foil L5	Angled foil L5	No graphite	Adjusted beam	No graphite and adjusted beam
H5	0.818 ± 0.004	1.229 ± 0.299	0.941 ± 0.058	0.986 ± 0.072	0.883 ± 0.041	1.175 ± 0.313	0.837 ± 0.025
H4	0.887 ± 0.005	0.756 ± 0.033	0.815 ± 0.042	0.737 ± 0.040	0.667 ± 0.019	0.652 ± 0.057	0.563 ± 0.069
M5	1.577 ± 0.010	1.787 ± 0.066	1.855 ± 0.122	2.147 ± 0.181	1.313 ± 0.054	1.787 ± 0.115	0.971 ± 0.078
M4	1.286 ± 0.001	1.052 ± 0.087	1.114 ± 0.075	0.935 ± 0.04	0.891 ± 0.036	0.823 ± 0.129	0.830 ± 0.078
M3	1.056 ± 0.006	0.651 ± 0.043	0.621 ± 0.05	0.671 ± 0.051	0.736 ± 0.044	0.538 ± 0.026	0.574 ± 0.019
M2	0.358 ± 0.008	0.265 ± 0.025	0.258 ± 0.043	0.248 ± 0.022	0.213 ± 0.019	0.282 ± 0.019	0.387 ± 0.118
M1	0.322 ± 0.006	0.254 ± 0.069	0.229 ± 0.030	0.191 ± 0.014	0.206 ± 0.019	0.315 ± 0.078	0.167 ± 0.043
L5	6.130 ± 0.012	10.789 ± 0.321	11.133 ± 0.201	10.916 ± 0.204	6.559 ± 0.253	9.899 ± 0.627	6.005 ± 0.317
L4	2.941 ± 0.008	3.612 ± 0.069	3.585 ± 0.080	3.543 ± 0.039	3.307 ± 0.039	3.535 ± 0.135	2.981 ± 0.130
L3	2.475 ± 0.007	2.068 ± 0.063	2.257 ± 0.191	2.128 ± 0.079	1.966 ± 0.038	2.135 ± 0.061	1.869 ± 0.017
L2	0.714 ± 0.010	0.806 ± 0.061	0.686 ± 0.048	0.699 ± 0.035	0.703 ± 0.040	0.762 ± 0.016	0.782 ± 0.074
L1	0.736 ± 0.005	0.573 ± 0.037	0.595 ± 0.027	0.592 ± 0.030	0.539 ± 0.038	0.675 ± 0.042	0.637 ± 0.035

Table A.16: Simulation - 87 K no Cd (activation in Bq/mg/μA-s)

Foil position	Original Simulation	Contaminated moderator	Less D2O	Beam hit collimator
H5	1.802 ± 0.012	1.99 ± 0.17	1.73 ± 0.09	2.11 ± 0.14
H4	1.561 ± 0.010	1.29 ± 0.14	1.12 ± 0.05	1.18 ± 0.06
M5	3.847 ± 0.017	4.40 ± 0.20	4.10 ± 0.21	4.47 ± 0.20
M4	2.527 ± 0.015	1.64 ± 0.12	1.88 ± 0.23	1.68 ± 0.16
M3	2.784 ± 0.017	1.16 ± 0.06	1.16 ± 0.10	1.24 ± 0.12
M2	1.045 ± 0.012	0.65 ± 0.05	0.81 ± 0.09	0.74 ± 0.10
M1	1.236 ± 0.013	0.54 ± 0.05	0.64 ± 0.06	0.59 ± 0.06
L5	10.192 ± 0.018	12.98 ± 0.35	14.04 ± 0.69	13.42 ± 0.24
L4	4.930 ± 0.016	4.21 ± 0.07	4.55 ± 0.14	4.45 ± 0.11
L3	5.198 ± 0.016	2.69 ± 0.05	3.12 ± 0.09	3.00 ± 0.11
L2	1.729 ± 0.012	1.21 ± 0.04	1.49 ± 0.14	1.42 ± 0.07
L1	2.111 ± 0.012	1.17 ± 0.09	1.06 ± 0.05	1.48 ± 0.15

Table A.17: Simulation - 87 K with Cd (activation in Bq/mg/μA-s)

Foil position	Original Simulation	Contaminated moderator	Less D2O	Beam hit collimator
H5	1.573 ± 0.011	0.98 ± 0.07	0.75 ± 0.05	1.07 ± 0.08
H4	1.433 ± 0.010	0.81 ± 0.14	0.65 ± 0.03	0.73 ± 0.06
M5	3.236 ± 0.015	1.99 ± 0.18	2.45 ± 0.70	1.77 ± 0.09
M4	2.169 ± 0.014	0.88 ± 0.04	1.11 ± 0.05	1.42 ± 0.25
M3	2.344 ± 0.019	0.66 ± 0.03	0.64 ± 0.05	0.68 ± 0.03
M2	0.865 ± 0.011	0.29 ± 0.05	0.24 ± 0.02	0.34 ± 0.05
M1	0.961 ± 0.012	0.21 ± 0.02	0.24 ± 0.02	0.24 ± 0.03
L5	9.683 ± 0.019	9.15 ± 0.23	9.85 ± 0.18	10.08 ± 0.19
L4	4.565 ± 0.017	3.09 ± 0.09	3.40 ± 0.10	3.23 ± 0.07
L3	4.832 ± 0.016	1.93 ± 0.04	1.96 ± 0.05	1.90 ± 0.03
L2	1.541 ± 0.016	0.68 ± 0.02	0.77 ± 0.04	0.83 ± 0.03
L1	1.895 ± 0.011	0.69 ± 0.06	0.62 ± 0.02	0.83 ± 0.10

Table A.18: Simulation - 300 K no Cd (activation in Bq/mg/μA-s)

Foil position	Original Simulation	Contaminated moderator	Less D2O	Beam hit collimator
H5	0.869 ± 0.007	1.67 ± 0.08	1.52 ± 0.08	1.88 ± 0.22
H4	0.934 ± 0.006	0.92 ± 0.06	0.96 ± 0.06	1.13 ± 0.10
M5	1.656 ± 0.007	3.59 ± 0.16	3.28 ± 0.15	3.64 ± 0.17
M4	1.359 ± 0.006	1.39 ± 0.07	1.36 ± 0.05	1.43 ± 0.06
M3	1.148 ± 0.009	0.99 ± 0.05	1.07 ± 0.09	1.08 ± 0.09
M2	0.393 ± 0.005	0.54 ± 0.09	0.50 ± 0.05	0.51 ± 0.04
M1	0.357 ± 0.004	0.44 ± 0.05	0.51 ± 0.06	0.42 ± 0.03
L5	6.206 ± 0.011	13.57 ± 0.31	13.68 ± 0.32	13.78 ± 0.62
L4	3.001 ± 0.008	4.33 ± 0.08	4.83 ± 0.19	4.16 ± 0.04
L3	2.539 ± 0.007	2.66 ± 0.08	3.43 ± 0.47	2.85 ± 0.08
L2	0.734 ± 0.007	1.18 ± 0.09	1.42 ± 0.07	1.44 ± 0.13
L1	0.778 ± 0.006	1.05 ± 0.06	1.24 ± 0.06	1.35 ± 0.09

Table A.19: Simulation - 300 K with Cd (activation in Bq/mg/μA-s)

Foil position	Original Simulation	Contaminated moderator	Less D2O	Beam hit collimator
H5	0.818 ± 0.004	0.76 ± 0.02	0.74 ± 0.03	0.92 ± 0.04
H4	0.887 ± 0.005	0.67 ± 0.04	0.71 ± 0.06	0.70 ± 0.05
M5	1.577 ± 0.010	1.67 ± 0.07	1.72 ± 0.09	1.72 ± 0.11
M4	1.286 ± 0.001	1.13 ± 0.19	0.82 ± 0.04	0.85 ± 0.03
M3	1.056 ± 0.006	0.61 ± 0.04	0.61 ± 0.04	0.63 ± 0.05
M2	0.358 ± 0.008	0.22 ± 0.02	0.25 ± 0.03	0.28 ± 0.02
M1	0.322 ± 0.006	0.18 ± 0.01	0.23 ± 0.04	0.27 ± 0.04
L5	6.130 ± 0.0120	9.39 ± 0.23	10.34 ± 0.34	9.80 ± 0.20
L4	2.941 ± 0.008	3.26 ± 0.07	3.32 ± 0.07	3.24 ± 0.08
L3	2.475 ± 0.007	1.77 ± 0.05	1.91 ± 0.06	1.88 ± 0.05
L2	0.714 ± 0.010	0.72 ± 0.04	0.78 ± 0.03	0.76 ± 0.02
L1	0.736 ± 0.005	0.61 ± 0.05	0.63 ± 0.03	0.67 ± 0.02

Bibliography

[1] A. Riotta and M. Trodden, “Recent Progress in Baryogenesis,” *Annu. Rev. Nucl. Part. Sci.*, vol. 49, no. 1, pp. 35–75, 1999.

[2] D. E. Morrissey and M. J. Ramsey-Musolf, “Electroweak baryogenesis,” *New Journal of Physics*, vol. 14, no. 12, p. 125003, 2012.

[3] M. Dine and A. Kusenko, “Origin of the matter-antimatter asymmetry,” *Rev. Mod. Phys.*, vol. 76, no. 1, p. 1, 2003.

[4] A. D. Sakharov, “Violation of CP invariance, C asymmetry, and baryon asymmetry of the universe,” *JETP Lett.*, vol. 5, pp. 24–27, 1967.

[5] M. Pospelov and A. Ritz., “Electric dipole moments as probes of new physics,” *Annals of Physics*, vol. 318, no. 1, pp. 119–169, 2005.

[6] J. M. Pendlebury *et al.*, “A revised experimental upper limit on the electric dipole moment of the neutron,” *Phys. Rev. D*, vol. 92, no. 9, p. 092003, 2015.

[7] D. V. Nanopoulos, A. Yildiz, and P. H. Cox, “On the electric dipole moment of the neutron,” *Phys. Lett. B*, vol. 87, no. 1–2, pp. 53–56, 1979.

[8] C. Patrignani *et al.* vol. 40, no. 100001, 2016 (update in 2017). Particle Data Group.

[9] P. Schmidt-Wellenburg, “The quest to find an electric dipole moment of the neutron,” 2017. arXiv preprint arXiv:1607.06609v2.

[10] S. Raby, “Family Mixing and the Origin of Mass: The difference between weak eigenstates and mass eigenstates,” *Los Alamos Science*, vol. 25, p. 25, 1997.

[11] I. B. Khriplovich and A. R. Zhitnitsky, “What is the value of the neutron electric dipole moment in the Kobayashi-Maskawa model?,” *Phys. Lett. B*, vol. 109, no. 6, pp. 490–492, 1982.

[12] R. D. Peccei and H. R. Quinn, “CP Conservation in the Presence of Pseudoparticles,” *Phys. Rev. Lett.*, vol. 38, no. 25, p. 1440, 1977.

[13] H. Baer *et al.*, “Dark matter production in the early Universe: Beyond the thermal WIMP paradigm,” *Phys. Rep.*, vol. 555, pp. 1–60, 2015.

[14] S. A. Abel and O. Lebedev, “Neutron-electron EDM correlations in supersymmetry and prospects for EDM searches,” *J. High Energy Phys.*, vol. 2006, no. 1, 2006.

[15] B. Lauss, “The next phase of the search for a neutron electric dipole moment at the Paul Scherrer Institute - Status of n2EDM,” nEDM2017, 2017.

[16] G. Bison *et al.*, “Comparison of ultracold neutron sources for fundamental physics measurements,” *Phys. Rev. C*, vol. 95, no. 4, p. 045503, 2017.

[17] R. Golub, D. Richardson, and S. Lamoreaux, *Ultra-Cold Neutrons*. Adam Hilger, Bristol, Philadelphia, and New York, 1991.

[18] V. Ignatovich, *The Physics of Ultracold Neutrons*. Clarendon, Oxford, 1990.

[19] V. Helaine, *Neutron Electric Dipole Moment measurement: simultaneous spin analysis and preliminary data analysis*. PhD thesis, University of Caen, 2014. Nuclear Experiment.

[20] I. Altarev *et al.*, “A large-scale magnetic shield with 10^6 damping at millihertz frequencies,” *Journal of Applied Physics*, vol. 117, no. 18, 2015.

[21] J. Voigt *et al.*, “Measures to reduce the residual field and field gradient inside a magnetically shielded room by a factor of more than 10,” *Metrol. Meas. Syst.*, vol. 20, no. 2, pp. 239–248, 2013.

[22] N. F. Ramsey, “A molecular beam resonance method with separated oscillating fields,” *Phys. Rev.*, vol. 78, no. 6, p. 695, 1950.

[23] F. M. Piegsa, B. van den Brandt, P. Hautle, and J. A. Konter, “A compact neutron Ramsay resonance apparatus for polarised neutron radiography,” *Nucl. Instrum. Methods Phys. Res., Sec. A*, vol. 605, no. 1–2, pp. 5–8, 2009.

[24] V. I. Luschikov and Y. Taran, “On the calculation of the neutron adiabatic spin-flipper,” *Nucl. Instrum. Methods Phys. Res., Sect. A*, vol. 228, no. 1, pp. 159–160, 1984.

[25] P. Geltenbort *et al.*, “A compact, large-diameter adiabatic spinflipper for ultracold neutrons,” *Nucl. Instrum. Methods Phys. Res., Sect. A*, vol. 608, no. 1, pp. 132–138, 2009.

[26] J. Karch *et al.*, “Performance of the solid deuterium ultra-cold neutron source at the pulsed reactor TRIGA Mainz,” *Eur. Phys. J. A*, vol. 50, no. 4, p. 78, 2014.

[27] R. Golub and J. M. Pendlebury, “Super-thermal sources of ultra-cold neutrons,” *Phys. Lett. A*, vol. 53, no. 2, pp. 133–135, 1975.

[28] R. Golub *et al.*, “Operation of a superthermal ultra-cold neutron source and the storage of ultra-cold neutrons in superfluid Helium4,” *Z. Phys. B*, vol. 51, no. 3, pp. 187–193, 1983.

[29] P. Schmidt-Wellenburg, K. H. Andersen, and O. Zimmer, “Ultra cold neutron production by multiphonon processes in superfluid helium under pressure,” *Nucl. Instrum. Methods Phys. Res., Sect. A*, vol. 611, no. 2–3, pp. 259–262, 2009.

[30] Y. Masuda *et al.*, “Spallation ultracold neutron source of superfluid helium below 1 k,” *Phys. Rev. Lett.*, vol. 108, no. 13, p. 134801, 2012.

[31] O. Zimmer, F. M. Piegsa, and S. N. Ivanov, “Superthermal sources of ultracold neutrons for fundamental physics experiments,” *Phys. Rev. Lett.*, vol. 107, no. 13, p. 134801, 2011.

[32] R. Golub and K. Böning, “New type of low temperature source of Ultra-cold neutrons and production of continuous beams of UCN,” *Z. Phys. B*, vol. 51, no. 2, pp. 95–98, 1983.

[33] A. P. Serebrov *et al.*, “Solid deuterium source of ultracold neutrons based on a pulsed spallation source,” *JETP Lett.*, vol. 66, no. 12, pp. 802–808, 1997.

[34] Yu.N. Pokotilovski, “Production and storage of ultracold neutrons at pulse neutron sources with low repetition rates,” *Nucl. Instrum. Methods Phys. Res., Sect. A*, vol. 356, no. 2–3, pp. 412–414, 1995.

[35] B. Lauss and UCN Project Team, “A new facility for fundamental particle physics: The high-intensity ultracold neutron source at the Paul Scherrer Institute,” in *AIP Conference Proceedings*, vol. 1441, pp. 576–578, AIP, 2012. `http://dx.doi.org/10.1063/1.3700622`.

[36] C. Patrignani *et al. Chin. Phys. C*, vol. 40, no. 10, p. 100001, 2017. Particle Data Group.

[37] C. A. Baker *et al. Nucl. Instrum. Methods Phys. Res., Sect. A*, vol. 736, pp. 184–203, 2014.

[38] “Pf2: the very cold and ultracold neutron facility,” 2017. `https://www.ill.eu/`.

[39] A. Steyerl *et al.*, “A new source of cold and ultracold neutrons,” *Phys. Lett. A*, vol. 116, no. 7, pp. 347–352, 1986.

[40] A. P. Serebrov *et al.*, “New Measurements of the Neutron Electric Dipole Moment with the Petersburg Nuclear Physics Institute Double-Chamber Electric Dipole Moment Spectrometer,” *Physics of Particles and Nuclei Letters*, vol. 12, no. 2, pp. 286–296, 2015.

[41] B. Lauss, “Status of the apparatus for the next phase of the neutron EDM search at PSI – n2EDM,” nEDM2017, 2017. `https://meetings.triumf.ca/indico/event/10/session/0/contribution/1/material/slides/0.pdf`.

[42] P. Schmidt-Wellenburg, “Status of the data-analysis of the nEDM search at PSI,” nEDM2017, 2017.

[43] B. Lauss, “Ultracold Neutron Production at the Second Spallation Target of the Paul Scherrer Institute,” *Physics Procedia*, vol. 51, pp. 98–101, 2014.

[44] H. Beckera *et al.*, “Neutron production and thermal moderation at the PSI UCN source,” *Nucl. Instrum. Methods Phys. Res., Sect. A*, vol. 777, pp. 20–27, 2014.

[45] I. Altarev *et al.*, “Direct Experimental Verification of Neutron Acceleration by the Material Optical Potential of solid $^2H_2$,” *Phys. Rev. Lett.*, vol. 100, no. 1, p. 014801, 2008.

[46] C. A. Baker *et al.*, “The search for the neutron electric dipole moment at the Paul Scherrer Institute,” *Physics Procedia*, vol. 17, pp. 159–167, 2011.

[47] K. Green *et al.*, “Performance of an atomic mercury magnetometer in the neutron EDM experiment,” *Nucl. Instrum. Methods Phys. Res., Sect. A*, vol. 404, no. 2–3, pp. 381–393, 1998.

[48] O. Zimmer, “SuperSUN new infrastructure for experiments with ultracold neutrons,” PSI2016, 2017. `https://indico.psi.ch/getFile.py/access?contribId=241&resId=0&materialId=slides&confId=3914`.

[49] K. K. H. Leung *et al.*, “Ultracold neutron production and up-scattering in superfluid helium between 1.1 K and 2.4 K,” *Phys. Rev. C*, vol. 93, no. 2, p. 025501, 2016.

[50] K. K. H. Leung, *Development of a new superfluid helium ultra-cold neutron source and a new magnetic trap for neutron lifetime measurements*. PhD thesis, Technische Universität München, 2013.

[51] S. Degenkolb *et al.*, “SuperSUN and PanEDM: a new superthermal UCN source for a new nEDM measurement,” nEDM2017, 2017. `https://indico.psi.ch/getFile.`

py/access?contribId=241&resId=0&materialId=slides&confId=3914.

[52] V. Fedorov, V. Voronin, and Y. Braginetz, "Search for the neutron EDM by crystal-diffraction method. Test experiment and future progress," *Physica B: Condensed Matter Physics*, vol. 406, no. 12, pp. 2370–2372, 2011.

[53] "How SNS Works," 2018. https://neutrons.ornl.gov/content/how-sns-works.

[54] B. Filippone, "The SNS nEDM experiment," nEDM2017, 2017.

[55] E. Korobkina, "Systematic and Operational study apparatus for nEDM@SNS," nEDM2017, 2017.

[56] T. M. Ito *et al.*, "An apparatus for studying electrical breakdown in liquid helium at 0.4 K and testing electrode materials for the SNS nEDM experiment," *Review of Scientific instruments*, vol. 87, no. 4, p. 045113, 2016.

[57] T. M. Ito *et al.*, "Performance of the upgraded ultracold neutron source at Los Alamos National Laboratory and its implication for a possible neutron electric dipole moment experiment," *Phys. Rev. C*, vol. 97, no. 1, p. 012501, 2017.

[58] S. Clayton, "R&D toward a new nEDM Experiment at LANL," nEDM2017, 2017. https://meetings.triumf.ca/indico/event/10/session/4/contribution/17/material/slides/0.pdf.

[59] A. Fomin, "Supersource of ultracold neutrons with superfluid helium at WWR-M reactor," nEDM2017, 2017. https://meetings.triumf.ca/indico/event/10/session/2/contribution/0/material/slides/0.pdf.

[60] A. P. Serebrov *et al.*, "Research of fundamental interactions with use of ultracold neutrons," vol. 798, no. 1, p. 012206, 2017. IOP Publishing.

[61] "FRM-II UCN." http://www.mlz-garching.de/ucn, 2018.

[62] T. Lauer and T. Zechlau, "A prospective pulsed source of ultracold neutrons for experiments in fundamental neutron physics," *Eur. Phys. J. A*, vol. 49, no. 8, p. 104, 2013.

[63] I. Altarev *et al.*, "Minimizing magnetic fields for precision experiments," *Journal of Applied Physics*, vol. 117, no. 23, p. 233903, 2015.

[64] "FRM-II EDM." http://www.mlz-garching.de/edm, 2018.

[65] J. Kahlenberg *et al.*, "Upgrade of the ultracold neutron source at the pulsed reactor TRIGA Mainz," *Eur. Phys. J. A*, vol. 53, p. 226, 2017.

[66] "TRIUMF's (ultra)cool experiment fires up." http://www.triumf.ca/first-triumf-ucns, 2017.

[67] "Ultracold Neutron Electric Dipole Moment Experiment," 2017. CFI Proposal.

[68] T. Kikawa, "Developments for the next generation neutron EDM search at TRIUMF," nEDM2017, 2017.

[69] K. Matsuta *et al. Hyp. Int.*, vol. 220, p. 89, 2013.

[70] "correspondence with Tatsuya Kikawa."

[71] T. Ito, 2014. presentation in Ascona, Switzerland.

[72] J. Pendlebury *et al.*, "Geometric-phase-induced false electric dipole moment signals for particles in traps," *Phys. Rev. A*, vol. 70, no. 3, p. 032102, 2004.

[73] G. Pignol and S. Roccia, "Electric-dipole-moment searches: Reexamination of frequency shifts for particles in traps," *Phys. Rev. A*, vol. 85, no. 4, p. 042105, 2012.

[74] G. Rogel, *Développement de détecteurs de neutrons ultra-froids et d'un système d'analyse de polarisation pour la mesure du moment électrique dipolaire du neutron*. PhD thesis, University of Caen, 2009.

[75] G. Ban *et al.*, "UCN detection with 6Li-doped glass scintillators," *Nucl. Instrum. Methods Phys. Res., Sect. A*, vol. 611, pp. 280–283, 2009.

[76] C. Morris *et al.*, "Multi-wire proportional chamber for ultra-cold neutron detection," *Nucl. Instrum. Methods Phys. Res., Sect. A*, vol. 599, pp. 248–250, 2009.

[77] F. Sauli, "GEM: A new concept for electron amplification in gas detectors," *Nucl. Instrum. Methods Phys. Res., Sect. A*, vol. 386, no. 2–3, pp. 531–534, 1997.

[78] "CASCADE: A High-Rates Detector for Neutron Applications in Science and Research," 2018. `http://www.n-cdt.com/`.

[79] C. A. Baker *et al.*, "Development of solid-state silicon devices as ultra cold neutron detectors," *Nucl. Instrum. Methods Phys. Res., Sect. A*, vol. 487, no. 3, pp. 511–520, 2002.

[80] M. Lasakov *et al.*, "A large area silicon UCN detector with the analysis of UCN polarization," *Nucl. Instrum. Methods Phys. Res., Sect. A*, vol. 545, pp. 301–308, 2005.

[81] G. Ban *et al.*, "A novel fast UCN detector based on the 6Li doped glass scintillators." presentation.

[82] Applied Scintillation Technologies, "Lithium-6 Enriched Glass," 2014. `http://www.appscintech.com/products/gs20-lithium-6-glass`.

[83] Applied Scintillation Technologies, "Lithium-7 Enriched Glass," 2014. `http://www.appscintech.com/products/gs30-lithium-7-glass`.

[84] B. Jamieson and L. Rebenitsch, "Determining the ^{6}Li doped side of a glass scintillator for ultra cold neutrons," *Nucl. Instrum. Methods Phys. Res., Sect. A*, vol. 790, pp. 6–9, 2015.

[85] CAEN S.p.A., "UM2580 DPP-PSD User Manual rev.8," 2016. `www.caen.it`.

[86] "ROOT Data Analysis Framework," 2018. `https://root.cern.ch/`.

[87] B. Jamieson, L. Rebenitsch, S. Hansen-Romu, B. Lauss, T. Lindner, R. Mammei, J. Martin, and E. Pierre, “Characterization of a scintillating lithium glass ultra-cold neutron detector,” *Eur. Phys. J. A*, vol. 53, p. 3, 2017.

[88] Ban *et al. Eur. Phys. J. A*, vol. 52, p. 326, 2016.

[89] A. Anghel *et al.*, “The PSI ultra-cold neutron source,” *Nuclear Instruments and Methods in Physics Research Section A: Accelerators, Spectrometers, Detectors and Associated Equipment*, vol. 611, no. 2-3, pp. 20–27, 2009.

[90] B. Lauss, “Startup of the high-intensity ultracold neutron source at the Paul Scherrer Institute,” *Hyperfine Interactions*, vol. 211, no. 1–3, pp. 21–25, 2012.

[91] K. Kirch, B. Lauss, P. Schmidt-Wellenburg, and G. Zsigmond *Nuclear Physics News*, vol. 20, no. 1, p. 17, 2010.

[92] “Evaluated Nuclear Structure Data File (ENSDF). National Nuclear Data Center.” Brookhaven National Laboratory, 2014. `www.nndc.bnl.gov/ensdf/`.

[93] “correspondence with Ewart Blackmore.”

[94] R. Samarasekera, “TRIUMF: PIF and NIF.” `http://www.triumf.ca/pif-nif`, 2011.

[95] Canberra, “GENIE 2000 Software Family.” `http://www.canberra.com/products/radiochemistry_lab/genie-2000-software.asp`, 2016.

[96] “correspondence with Max Kinakin.”

[97] ASTM E262-3, “Standard test method for determining thermal neutron reaction rates and thermal neutron fluence rates by radioactivation techniques,” *ASTM International*, 2013.

[98] “FLUKA simulation package.” `http://www.fluka.org/`, 2018.

[99] T. Zhou, *Benchmarking Thermal Neutron Scattering in Graphite*. PhD thesis, North Carolina State University, 2006.

[100] "flair for FLUKA." `http://www.fluka.org/flair/`, 2012.

[101] H. Xiaolong and K. Mengxaio, "Nuclear Data Sheets for A = 198," *Nuclear Data Sheets*, vol. 133, 2016.

[102] R. Picker, B. Franke, and C. Davis, "BL1U and cold neutron source tests at TRIUMF Fall 2016," 2018. TRIUMF.